

DYNAMICS OF OCEAN JETS OVER TOPOGRAPHY

A THESIS PRESENTED FOR THE DEGREE OF
DOCTOR OF PHILOSOPHY OF IMPERIAL COLLEGE LONDON
AND THE
DIPLOMA OF IMPERIAL COLLEGE
BY
HEMANT KHATRI

DEPARTMENT OF MATHEMATICS
IMPERIAL COLLEGE
180 QUEEN'S GATE, LONDON SW7 2BZ

JULY 2019

I certify that this dissertation is the result of my own work and any ideas from the work of other people, published or otherwise, are fully acknowledged in accordance with the standard referencing practices of the discipline.. This dissertation, or any part of it, has not been submitted for award of a degree or diploma or other qualification at Imperial College London or any other university.

Signed: _____

COPYRIGHT

The copyright of this thesis rests with the author. Unless otherwise indicated, its contents are licensed under a Creative Commons Attribution-Non Commercial 4.0 International Licence (CC BY-NC).

Under this licence, you may copy and redistribute the material in any medium or format. You may also create and distribute modified versions of the work. This is on the condition that: you credit the author and do not use it, or any derivative works, for a commercial purpose.

When reusing or sharing this work, ensure you make the licence terms clear to others by naming the licence and linking to the licence text. Where a work has been adapted, you should indicate that the work has been changed and describe those changes.

Please seek permission from the copyright holder for uses of this work that are not included in this licence or permitted under UK Copyright Law.

Dynamics of ocean jets over topography

ABSTRACT

Alternating jets seen in the oceans are often transient in nature as they possess spatio-temporal variability. Ocean bathymetry is believed to be one of the primary causes for the jet variability. In this thesis, the dynamics of alternating jets and mesoscale eddies is studied in the presence of a zonally sloped topography in a baroclinic quasi-geostrophic model, which is forced with an imposed vertical velocity shear. It is observed that the jets tilt from the zonal direction and drift meridionally. The jets tend to align with the barotropic potential vorticity isolines and drift speeds match well with the phase speeds of linear Rossby waves. Thus, the linear dynamics controls the jet drift. Also, the tilted jets are coupled to the imposed shear and are able to gain energy directly from the imposed shear. On the other hand, eddies remove energy from the jets; hence, eddies act against the jets. The results are further confirmed by analysing the mean-flow and eddy energy budgets.

These results are limited to continuously forced dissipative systems. In weak dissipation regimes, in addition to the tilted jets, purely zonal large-scale modes are observed. The zonal modes gain energy from eddies and the tilted jets through nonlinear interactions. The results suggest that alternating jet patterns in the oceans can also form due to interactions among eddies and various large-scale modes. The mechanism is different from the classical arguments, in which only mesoscale eddies force the jets. Also, a direct energy transfer from the imposed shear to jets is not possible in the model of stationary zonally symmetric jets. Further, it is found that energy transfer to the jets via Reynolds stress work is higher in the layer having a positive meridional gradient in the background potential vorticity. This is qualitatively explained by simple reasoning based on Rossby wave group velocity.

This dissertation is dedicated to my family.

ACKNOWLEDGMENTS

Firstly, I would like to thank my advisor Pavel Berloff, without whom I could not have completed this thesis. His continuous guidance and encouragement helped me immensely during my PhD. I am grateful to him for reading through my derivations and helping me with physical interpretations of the results.

I would also like to thank Darryl Holm and Igor Shevchenko for their comments and suggestions on my work during my early-stage and late-stage reviews. Igor Shevchenko also helped me with the numerical simulations when I was in the initial state of my PhD. I am also grateful to my PhD examiners David Marshall and Xuesong Wu for their comments and suggestions on this thesis.

I would like to extend my gratitude to Andrew Thompson, Jai Sukhatme, Navid Constantinou, William Young, Paula Cessi, Freddy Bouchet, Peter Haynes, Rupert Klein, Stephen Griffies, Michael Haigh, Erwin Luesink, Laura Cope, Dhruv Balwada, Takaya Uchida, Mary O'Donnell and Josephine Park for useful conversations that I had with them over the course of my PhD. Numerous reviewers have given important feedback that has helped me in improving this thesis and the related research articles.

I am grateful to the HPC team at Imperial College and Andrew Thomas for their help with computer clusters. I also want to acknowledge the financial support from the President's Scholarship and Mathematics of Planet Earth CDT at Imperial College London.

Finally, I would like to thank my family, especially my parents, and friends, who have always cared for me and motivated me.

LIST OF FIGURES

1.1 Snapshot of geostrophic velocity anomaly (30 th June) on the ocean surface from satellite altimetry data in the North-West Pacific. The zonal velocity is shown in colour (units are in m s ⁻¹). Alternating jet patterns can be seen inside the green boxes.	4
2.1 Adopted from Khatri and Berloff (2018a). Sketch of the model domain. A uniform eastward background flow U_b is imposed in the upper layer. H_i , ρ_i are the layer depth and density, respectively. η_T is the topographic height. x axis is along the zonal direction and the meridional axis y points into the sketch.	7
2.2 Baroclinic growth rates (red curves) of the most unstable modes for different magnitudes of U_b and T_x . For the rest of the parameters, values shown in table 2.1 were used in the computations. Blue curves represent the background PV gradients in the meridional direction in individual layers.	10
2.3 Imaginary (ω^i) and real parts (ω^r) of frequencies obtained from the dispersion relation (equation 2.3). k_x and k_y are the zonal and meridional wavenumbers, respectively. Top panels are for the flat topography case and bottom panels correspond to the zonally sloped topography case with $T_x = 1.4 \times 10^{-12} \text{ m}^{-1}\text{s}^{-1}$. For the rest of the parameters, values shown in table 2.1 were used. Colorbar units are in 10^{-7}s^{-1} . Note that the top and bottom panels have the same colorbar shown between the panels.	10
2.4 Snapshots of the streamfunction field, ψ_i (units are in m^2s^{-1}), in the top (left panels) and bottom (right panels) layers at different times (top to bottom: snapshots at 600, 1000, 1400 days) over a zonally sloped topography. The simulation was run on a doubly periodic domain having 1024×512 grid points and the parameter values shown in table 2.1 were used. The core of the numerical model used in this thesis has been developed by Dr Pavel Berloff and his collaborators over the years. Topography was later included in the numerical model as a part of the research work presented in this thesis.	11

3.5	Adopted from Khatri and Berloff (2018a). Time-mean cross-jet profiles for the medium-slope simulation; (a,b): Eddy relative vorticity flux $\overline{v'_i \zeta'_i}$, eddy buoyancy flux $\epsilon_i S_i \overline{v'_i (\psi'_2 - \psi'_1)}$ and eddy PV flux $\overline{v'_i Q'_i}$; (c): Heat diffusivity. The profiles were averaged in the moving frame in the interval 10,000-20,000 days. The green curves in (a,b) represent the mean flow (normalised), and the actual velocity magnitudes are shown in (c).	22
3.6	Adopted from Khatri and Berloff (2018a). Sketch of the cross-jet profiles of the mean PV (violet) and mean along-jet velocity (red). The profiles show the offset in the alignment observed in the numerical simulations (relative magnitudes are not to scale). The locations of the maximum increase/decrease in PV are indicated with red dashed arrows and the resulting direction of jet drift is shown with violet arrows. The zero lines are shown with black dotted lines.	26
3.7	Adopted from Khatri and Berloff (2018a). Time evolution in the medium-slope simulation (a) Barotropic velocity = $\frac{1}{H_1 + H_2}(H_1 u_1 + H_2 u_2)$, (b) Baroclinic velocity = $u_1 - u_2$ (cross-jet profiles, averaged in p direction, were aligned in the frame of reference propagating with the drifting jets; legend units are in days), and (c) Correlation coefficients computed between the eddy forcing and PV profiles, and the barotropic kinetic energy fraction. Note that we computed the eddy field using the full flow-field at every time step because we could not compute a mean flow in the transient state.	28
4.1	Schematic of energetics. E_m (E_e) represents the energy gain by jets (eddies) from the imposed vertical shear. T_v and T_b are energy exchanges between the jets and eddies through momentum and buoyancy exchanges. The rest of the terms represent the energy loss through viscous dissipation and bottom friction.	32
4.2	Domain-averaged heat and PV diffusivity coefficients as a function of T_x . The computations were performed over the last 10,000 days in the frame of reference moving with the jets (see figure 3.3).	35
5.1	Leading EOFs of the streamfunction field in the simulation corresponding to figure 3.2 (data in the interval 10,000-20,000 days, i.e. 500 snapshots, was used for the EOF analysis); (a) EOF1, EOF2 (b) EOF3, EOF4. The spatial structure of the EOFs in the top layer is shown in the top panels, and Hovmöller diagrams of the J and Z modes reconstructed using EOFs and their PCs are shown in the middle panels (meridional cross-section of the modes at the centre of the domain is plotted against time). Colorbar range is [-1,1], blue to red. The power spectra of PCs (normalised to unity) corresponding to the EOFs are shown in the bottom panels. Note that the second and fourth EOFs are counterparts of the first and third EOFs, with the same spatial structure but with a phase shift of $\pi/2$. Here, one of the EOFs in a pair is shown. The J and Z modes together capture about 75% of the variance.	39

5.2 KE spectrum (units are in cm^2s^{-2}) averaged over 2,000 days (100 snapshots between 18,000-20,000 days); (a,b) $\nu = 200 \text{ m}^2\text{s}^{-1}$ and (c,d) $\nu = 50 \text{ m}^2\text{s}^{-1}$. The zonal and meridional wavenumbers are denoted by (k_x, k_y) . Green and red dots represent the wavenumbers corresponding to the J and Z modes, respectively. In the lower eddy viscosity case, the J and Z modes seem to interact nonlinearly and possibly exchange energy.	44
5.3 Time evolution of the KE spectrum (snapshots, units are in cm^2s^{-2}) in the simulation in which the background flow, eddy viscosity and bottom friction parameters were set to zero (a-e): KE spectra at 200, 400, 500, 600 and 800 days, respectively. The zonal and meridional wavenumbers are denoted by (k_x, k_y) . Green and red dots represent the wavenumbers corresponding to the J and Z modes, respectively.	45
5.4 Profiles of \bar{u}_i and \bar{u}_i'' used in the stability analysis. The profiles were computed by applying spatial and time averaging in the direction along the jets in the moving frame of reference between 10,000-20,000 days for the simulation corresponding to figure 5.1 (blue solid line in the top layer and red dotted line in the bottom layer). The velocity profile in the top layer is shown relative to the imposed background flow of 0.06 m s^{-1}	48
5.5 Real parts of eigenvalues (ω_r) obtained from the linear stability analysis for different values of eddy viscosity (left panels, for fixed $\gamma = 2 \times 10^{-8} \text{ s}^{-1}$) and bottom friction (right panels, for fixed $\nu = 100 \text{ m}^2\text{s}^{-1}$) vs wavenumber. Growth rates (day^{-1}) are shown in the colorbar. Eigenmodes having growth rates in the range $[-0.01, 0]$ are shown with grey dots. Growth rates increase with decreasing ν and γ	49
5.6 (a) The eigenvector corresponding to the fastest growing mode (b) Snapshots of the eddy field constructed using all EOFs except EOF1 and EOF2. Top and bottom panels correspond to the top and bottom layers, respectively. The snapshot of eddy field was constructed using the solution from the simulation run with $\nu = 150 \text{ m}^2 \text{ s}^{-1}$ (other parameters were the same as shown in table 2.1). In this case, there is a remarkable resemblance in the spatial structure between the eddy field and the fastest growing eigenmode. These banana-shaped eddies were also seen in the lower viscosity simulations; however, the banana-shaped structures appear less frequently because the eddy field tends to very complex in the presence of the Z mode.	50
6.1 Adopted from Khatri and Berloff (2018b). Meridional profiles of the zonal velocity in the top and bottom layers (averaged in the zonal direction and time for the last 10 years); (a) ES and (b) WS. Dashed and dash-dotted curves represent the mean barotropic ($\frac{H_1\bar{u}_1 + H_2\bar{u}_2}{H_1 + H_2}$) and baroclinic ($\bar{u}_1 - \bar{u}_2$) components in the flow field, respectively.	55
6.2 Adopted from Khatri and Berloff (2018b). Meridional profiles of the Reynolds stress term (solid blue) and form stress term (solid green) in the top (a,c) and bottom (b,d) layers. Left (a,b) and right (c,d) panels are for the ES and WS cases, respectively. The dashed curves represent the meridional profiles of the mean relative vorticity (dashed light green) and mean buoyancy (dashed orange). The profiles were averaged in the zonal direction as well as in time for the last 10 years. Additionally, the profiles of the stress terms were smoothed by applying moving averages in the meridional direction.	58

6.3	Adopted from Khatri and Berloff (2018b). Meridional profiles of heat diffusivity; (a) ES and (b) WS. The dash-dotted curves represent the meridional profiles of the mean zonal flow (averaged for the last 10 years) in the layers. A positive value of heat diffusivity indicates that eddy buoyancy fluxes are down-gradient.	59
6.4	Adopted from Khatri and Berloff (2018b). Meridional profiles of the RSC, FSC and dissipation terms; (a,b) ES (c,d) WS. \bar{u}_{iy} and ψ_{2x} represent the meridional and zonal gradient of the mean zonal velocity and bottom-layer streamfunction, respectively. Top and bottom panels correspond to the upper and lower layers, respectively. The layer-wise mean zonal velocity is represented by dash-dotted curves. The profiles were averaged in the zonal direction as well as in time for the last 10 years.	62
6.5	Adopted from Khatri and Berloff (2018b). Meridional profiles of layer-wise energy transfer from eddies to the zonal jets through RSC terms (solid) and the meridional gradient in the layer-wise full PV (dash-dotted); (a) ES (b) WS. \bar{u}_{iy} and \bar{q}_{iy} are the meridional gradient of the mean zonal velocity and mean PV, respectively, and $\beta_i^* = \beta + \epsilon_i S_i U_b$ ($\epsilon_1 = -\epsilon_2 = 1$) is the background PV gradient in i^{th} layer. The profiles were averaged in the zonal direction as well as in time for the last 10 years. The jets receive more energy through RSC term in the upper (lower) layer in the ES (WS) case.	65
B.1	Adopted from Khatri and Berloff (2018a). Tilted, drifting jets in a channel simulation; (a,b): Snapshots of the PV anomaly field in the top layer ($\nabla^2\psi_1 + S_1(\psi_2 - \psi_1)$) and bottom layer ($\nabla^2\psi_2 + S_2(\psi_1 - \psi_2)$) for the medium-slope configuration (colorbar units are in s^{-1}); (c,d): Hovmöller diagrams of the PV anomaly field in both layers (PV along a meridional cross-section is plotted against time). $\nu = 50 \text{ m}^2\text{s}^{-1}$ and $\gamma = 10^{-8} \text{ s}^{-1}$ were used in the simulation. The rest of the parameter values were the same as in table 2.1.	86
B.2	The leading EOFs of the streamfunction field in a channel simulation; (a) EOF1 (b) EOF3. The upper-layer spatial structure of the EOFs is shown in the top panels and the Hovmöller diagrams of the J and Z modes reconstructed using the EOFs and their PCs are shown in the middle panels. The J and Z modes together capture about 60% of the variance. The colorbar range is [-1,1], blue to red. The power spectra of PCs (normalised to unity) corresponding to the EOFs are shown in the bottom panels.	88
B.3	The first twenty EOFs of the streamfunction field in the doubly-periodic simulation corresponding to figure 5.1. The panels show the spatial structure of the EOFs in the top layer. The colorbar range is [-1,1], blue to red. The first twenty EOFs capture more than 90% of the variance.	88

LIST OF TABLES

2.1 Parameter values used in the numerical simulations. We ran different simulations for a range of magnitudes of T_x , ν and γ . Whenever not specified, $T_x = 1.4 \times 10^{-12} \text{ m}^{-1}\text{s}^{-1}$, $\nu = 100 \text{ m}^2\text{s}^{-1}$ and $\gamma = 2 \times 10^{-8} \text{ s}^{-1}$ were used in those cases.	8
3.1 Jet drift velocity (cm s^{-1}) estimates from the numerical simulations and dispersion relation. \hat{i} and \hat{j} represent the unit vectors in the zonal and meridional directions, respectively.	17
3.2 Correlation coefficients between the time-mean cross-jet profiles of the linear and nonlinear stress terms, and the mean PV (\bar{Q}_i) in both layers for the medium-slope simulation. The jets are forced by the linear stress terms while eddies act against the jets.	21
3.3 Correlation coefficients between the cross-jet profiles of the time-mean layer-wise eddy forcing ($EF_i = Rs_i + Fs_i$, where $i = 1$ and $i = 2$ indicate the top and bottom layers, respectively) and the time-mean PV (\bar{Q}_i) as a function of the zonal slope magnitude (T_x units are in $\text{m}^{-1}\text{s}^{-1}$). For the rest of the parameters in the numerical simulations, values shown in table 2.1 were used.	24
3.4 Correlation coefficients and the maximum/minimum lag-correlation coefficients between the time-mean cross-jet profiles of the linear stress terms and mean PV (\bar{Q}_i) for the medium-slope simulation. Here, a lag period of 180° is equal to the width (in q direction) of one jet pair.	25
3.5 Correlation coefficients and the maximum/minimum lag-correlation coefficients between the time-mean cross-jet profiles of the nonlinear stress terms and mean PV (\bar{Q}_i) for the medium-slope simulation. Here, a lag period of 180° is equal to the width (in q direction) of one jet pair.	25
4.1 Energy gains, exchanges and losses by the mean flow and eddies (units are in $10^4 \text{ m}^3\text{s}^{-3}$). E_m (E_e) represents the energy gain by the jets (eddies) from the imposed vertical shear. T_v and T_b are energy exchanges between the jets and eddies through momentum and buoyancy exchanges. The rest of the terms represent the energy loss through viscous dissipation and bottom friction. The terms were integrated over the whole domain and averaged over time (for the last 10,000 days in the simulations). The computations were performed in the frame of reference moving with the jets (see figure 3.3).	33

5.1	Variances and drift velocities, obtained from the numerical simulations (NS) as well as using the linear dispersion relation (DR), of the J and Z modes as a function of the slope magnitude. The rest of the parameters were kept the same in the simulations, see table 2.1. \hat{i} and \hat{j} are the zonal and meridional unit vectors, respectively. n_y is equal to the number of meridional wavelengths of a mode that is equal to the meridional width of the domain. In all simulations, the zonal wavelength of the J modes is equal to the zonal extent of the domain. $f_{BT} = \bar{E}_{BT}/(\bar{E}_{BT} + \bar{E}_{BC})$ is the the mean barotropic KE fraction, where $E_{BT} = 1/2 \int_A \mathbf{u}_{BT} ^2$ and $E_{BC} = 1/2 \int_A \mathbf{u}_{BC} ^2$ are the barotropic and baroclinic KE, respectively, integrated over the whole domain.	40
5.2	Variances and propagation velocities of the J and Z modes for different values of eddy viscosity (ν) in simulations run with $T_x = 1.4 \times 10^{-12} \text{ m}^{-1}\text{s}^{-1}$ and $\gamma = 2 \times 10^{-8} \text{ s}^{-1}$. The rest of the parameters were kept the same in the simulations (see table 2.1). \hat{i} and \hat{j} are the zonal and meridional unit vectors, respectively. $f_{BT} = \bar{E}_{BT}/(\bar{E}_{BT} + \bar{E}_{BC})$ is the the mean barotropic KE fraction, where $E_{BT} = 1/2 \int_A \mathbf{u}_{BT} ^2$ and $E_{BC} = 1/2 \int_A \mathbf{u}_{BC} ^2$ are the barotropic and baroclinic KE, respectively, integrated over the whole domain.	43
5.3	Variances and propagation velocities of the J and Z modes for different values of bottom friction (γ) in simulations run with $T_x = 1.4 \times 10^{-12} \text{ m}^{-1}\text{s}^{-1}$ and $\nu = 100 \text{ m}^2 \text{ s}^{-1}$. The rest of the parameters were kept the same in the simulations (see table 2.1). \hat{i} and \hat{j} are the zonal and meridional unit vectors, respectively. $f_{BT} = \bar{E}_{BT}/(\bar{E}_{BT} + \bar{E}_{BC})$ is the the mean barotropic KE fraction, where $E_{BT} = 1/2 \int_A \mathbf{u}_{BT} ^2$ and $E_{BC} = 1/2 \int_A \mathbf{u}_{BC} ^2$ are the barotropic and baroclinic KE, respectively, integrated over the whole domain.	43
6.1	Correlation coefficients, \mathcal{C} , computed by correlating the meridional profiles of the mean relative vorticity and buoyancy with the meridional profiles of the Reynolds stress term and form stress term. $i = 1$ ($i = 2$) indicates the top (bottom) layer and $\epsilon_1 = -\epsilon_2 = 1$	57
6.2	Energy exchange between the mean zonal flow and eddies through the RSC and FSC terms, and energy loss through viscous dissipation and bottom friction terms (averaged over the whole domain and time for the last 10 years) in the top and bottom layers. The units are in $10^{-7} \text{ m}^3\text{s}^{-3}$. δ_{ij} is the Kronecker delta and $\epsilon_1 = -\epsilon_2 = 1$	61

CONTENTS

1	INTRODUCTION	1
1.1	Formation of zonal jets	1
1.2	Jets in the oceans	3
1.3	Thesis outline	4
2	MODEL DESCRIPTION	6
2.1	Governing equations	7
2.2	Baroclinic instability	8
2.3	Numerical computations	10
3	MECHANISM FOR JET DRIFT	12
3.1	Jet dynamics in the equilibrium state	12
3.2	Drift velocities from the linear dispersion relation	16
3.3	Nonlinear effects and the role of eddies	17
3.4	Jet drift mechanism	24
3.5	Interpretation of the linear forcing	26
3.6	Energy equilibration and the long-time flow adjustment	27
3.7	Summary	28
4	ENERGETICS OF TILTED JETS	30
4.1	Energy budget analysis	30
4.2	Heat and PV diffusivities	34
4.3	Summary	35
5	EFFECTS OF VANISHING EDDY VISCOSITY	37
5.1	EOF analysis	38
5.2	Effects of eddy viscosity and bottom friction	42
5.3	Wave solutions for the Z modes	46
5.4	Linear stability analysis	47
5.5	Summary	52

6	ROLE OF EDDY FLUXES IN THE MAINTENANCE OF JETS	53
6.1	Dynamics of zonal jets and eddies	54
6.2	Reynolds and form stress terms	56
6.3	Zonal energy balance	59
6.4	Effect of bottom friction	61
6.5	Comparison with previous studies	63
6.6	Disparity in the upper and lower layer Reynolds stress correlations	64
6.7	Summary	68
7	CONCLUSIONS	70
7.1	Jet drift and the linear dynamics	71
7.2	Jet-topography interactions	71
7.3	Jet dynamics in weak dissipation regimes	72
7.4	Eddy fluxes and jet maintenance	74
7.5	Broader implications and future direction	74
APPENDIX A COORDINATE TRANSFORMATION		77
A.1	Governing equations in a rotated non-stationary frame of reference	77
A.2	PV budget in the statistical equilibrium	78
A.3	Energetics derivation	79
A.3.1	Energy budgets of the mean flow and eddies	81
A.4	Linearisation of the governing equations	83
APPENDIX B JETS IN CHANNEL SIMULATIONS		86
B.1	Jet tilt and drift in a channel simulation	86
B.2	<i>J</i> and <i>Z</i> modes in a channel simulation	87
B.3	EOFs in doubly-periodic simulations	87
APPENDIX C COPYRIGHT PERMISSIONS		89
REFERENCES		100

1

INTRODUCTION

On rapidly rotating planets, large-scale flows behave like quasi-two-dimensional flows, in which vertical velocities are of much smaller magnitude than horizontal velocity magnitudes. In such scenarios, kinetic energy injected at small spatial scales cascades upscale resulting in the formation of large-scale flows (Kraichnan, 1967; Charney, 1971). One of the most common examples of this mechanism is the presence of zonally-banded structures commonly referred to as “alternating jets” in the atmospheres of Jupiter and Saturn (Beebe et al., 1980; Gierasch et al., 1986; Read et al., 2009). In these atmospheres, the energy released at small-scales by baroclinic instabilities and small-scale convection due to internal heating is transferred to larger scales (see Young and Read, 2017) and this upscale energy transfer leads to the formation of alternating jet patterns. Similar multiple alternating jets have been witnessed in Earth’s oceans in satellite altimetry, float datasets and eddy-resolving ocean general circulation models (Maximenko et al., 2005; Nakano and Hasumi, 2005; Richards et al., 2006; Sokolov and Rintoul, 2007; Van Sebille et al., 2011; Cravatte et al., 2012; Buckingham and Cornillon, 2013; Cravatte et al., 2017).

1.1 FORMATION OF ZONAL JETS

The two-dimensional turbulence theory applies to an isotropic turbulent field (Kraichnan, 1967), whereas the zonal jet formation results in a highly anisotropic field. The first physical explanation of the jet formation was given by Rhines (1975). They argued that the isotropic inverse cascade of energy is modified in the presence of Rossby waves, which are present due to the rotation of the planet, and the energy is channelled into zonal structures. Also, the meridional scale of the jets is set by the magnitudes of eddy energy and β , which is the meridional gradient in the Coriolis parameter f ($f = 2\Omega \sin \phi$, where

Ω is the rotation rate of the planet and ϕ is the latitude). This scale is commonly known as the ‘Rhines scale’ L_R ,

$$L_R = \sqrt{\frac{2U}{\beta}}, \quad (1.1)$$

where U is the root-mean-square eddy velocity. The presence of alternating jets has been confirmed in a variety of eddy-resolving numerical models (Williams, 1979; Panetta, 1993; Vallis and Maltrud, 1993; Cho and Polvani, 1996; Huang and Robinson, 1998, and others) as well as in laboratory experiments (Read et al., 2004, 2007). It is seen that the meridional width of the jets agrees well with Rhines scaling (Rhines, 1975; Maltrud and Vallis, 1991; Vallis and Maltrud, 1993; Sukoriansky et al., 2007; Scott and Polvani, 2007; Chemke and Kaspi, 2015a).

The main feature of the alternating jet structure is that eastward jets are sharper and stronger than the westward return flows, which are relatively broader. The jets are forced by mesoscale eddies, which grow via baroclinic instability and transfer momentum up-gradient into the eastward jet cores (Panetta, 1993; Lee, 1997; Huang and Robinson, 1998; Thompson and Young, 2007). Due to the presence of the strong zonal flow, zonal jets act like partial barriers to meridional transport and the eddy diffusivity is significantly reduced across strong jets (Srinivasan and Young, 2014; Kong and Jansen, 2017). These features are well captured in stochastically forced, dissipative barotropic quasi-geostrophic (QG) models (Maltrud and Vallis, 1991; Danilov and Gryankin, 2004; Danilov and Gurarie, 2004; Suhas and Sukhatme, 2015) as well as in baroclinic QG models forced with a background vertical shear (Panetta, 1993; Thompson and Young, 2007; Berloff et al., 2009b).

Although jet formation is seen in a variety of numerical models, ambiguities remain about the importance of the vertical flow structure, and the interactions between the jets and eddies. It has been suggested that energy can also be transferred upscale nonlocally to zonal jets by interactions among barotropic and baroclinic modes (Thompson and Young, 2007; Berloff et al., 2009b; Berloff and Kamenkovich, 2013a,b). For example, Wordsworth et al. (2008) studied jet dynamics in a differentially heated, rotating annulus experiment and found evidence of nonlocal energy transfer from eddies to the jets. The stochastic structural stability theory and cumulant expansion methods also show that jets can be formed in the β -plane barotropic turbulence (Farrell and Ioannou, 2007; Marston et al., 2008; Srinivasan and Young, 2012; Constantinou et al., 2014). These studies suggest that zonal jets can emerge due to interactions between the mean zonal flow and eddies, even in the absence of an inverse cascade. This mechanism is known as ‘zonostrophic instability’ (Srinivasan and Young, 2012). It has also been suggested that the jet formation can be explained in terms of spatially inhomogeneous stirring of potential vorticity (PV) by eddies. This process results in a ‘staircase’ structure in the meridional PV profile and the zonal jets are generated at the PV interfaces (Baldwin et al., 2007; Dunkerton and Scott,

2008; Dritschel and McIntyre, 2008). In the oceans, multiple alternating jets can also be generated through other processes, e.g., instability of meridional boundary currents (Hristova et al., 2008; Wang et al., 2012), secondary or modulational instability of Rossby waves (Berloff, 2005b; Connaughton et al., 2010; Qiu et al., 2013), bottom topography (Sinha and Richards, 1999).

1.2 JETS IN THE OCEANS

Multiple jets have been witnessed in Earth's oceans (Maximenko et al., 2005; Sokolov and Rintoul, 2007; Van Sebille et al., 2011). Oceanic jets are about 200-400 km wide in the meridional direction and can extend up to two-three thousand km in the zonal direction (see figure 1.1). There is a good agreement that oceanic jets are dynamically similar to the zonal jets seen in planetary atmospheres and, at the leading order, oceanic jets can be explained with QG dynamics on the β -plane (Kramer et al., 2006; Nadiga, 2006). However, there are important differences between atmospheric and oceanic jets. Unlike the extremely persistent jets in planetary atmospheres, jets in the oceans show temporal and spatial variability (Thompson and Richards, 2011; Thompson and Sallée, 2012); thus, they are sometimes referred to as 'striations' or 'latent jets'. The jets in the oceans are not always zonal and can also drift meridionally, which has been observed in comprehensive ocean models and observational datasets (Nakano and Hasumi, 2005; Van Sebille et al., 2011; Stern et al., 2015; Chen et al., 2016).

Ocean bathymetry is one of the primary reasons for jet variability in the oceans. In many places in the global ocean, transient jets steered by topography have been found (Sokolov and Rintoul, 2007; Thompson, 2010; Thompson and Richards, 2011; Chen et al., 2015). Spatially non-uniform PV gradients are created in the presence of nonuniform topography and this affects the ocean circulation (Radko and Kamenkovich, 2017). Large-scale flows can become barotropically unstable over topography (Tansley and Marshall, 2001; Poulin and Flierl, 2005). In addition, bottom topography affects the baroclinic growth rates and stability of oceanic flows (Hart, 1975a,b; Benilov, 2001; Chen and Kamenkovich, 2013; Chen et al., 2015). In the presence of topography, cross-jet transport properties are significantly affected. For example, Thompson (2010) studied jet dynamics over a two-dimensional sinusoidal topography and found that eddy transport in the meridional direction increases with increasing the topographic steepness because of the generation of nonzonal mean flows (also see Tréguier and Panetta, 1994).

This thesis mainly concentrates on the drifting behaviour of multiple oceanic jets over topography. Drifting jets can play an important role in ocean transport. It is seen that spatially nonuniform PV gradients can result in asymmetric Reynolds stresses across jet cores, which then make the jets drift (Thompson, 2010; Stern et al., 2015). For example, over meridional ridges, jets propagate in the meridional direction because of off-

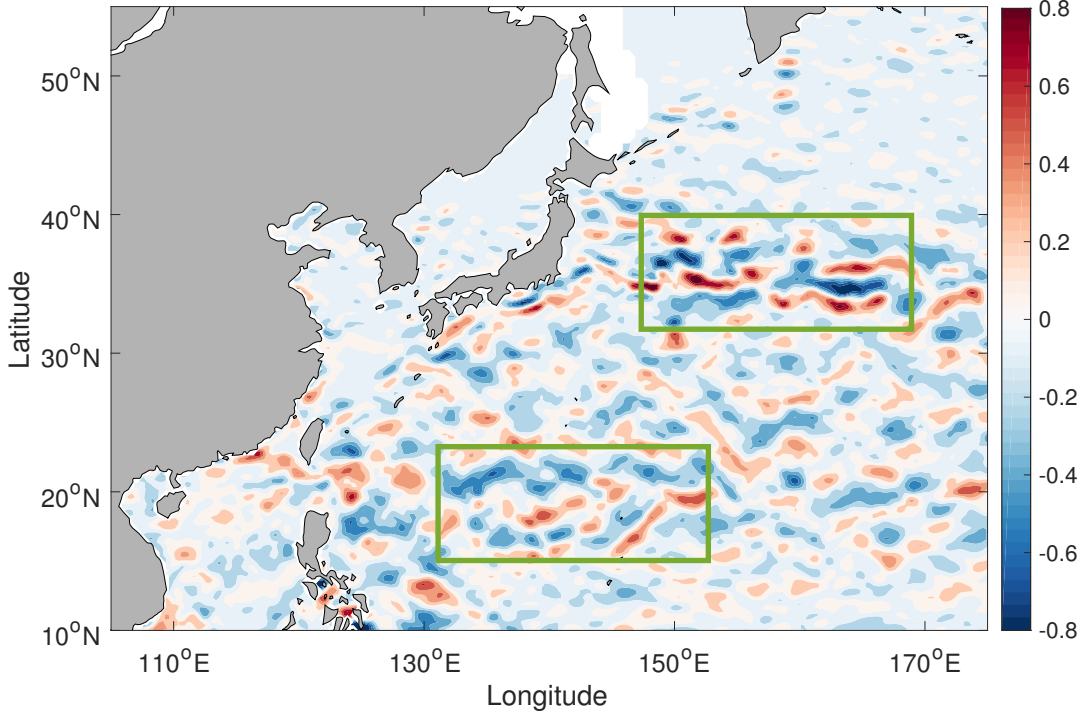


Figure 1.1: Snapshot of geostrophic velocity anomaly (30th June) on the ocean surface from satellite altimetry data in the North-West Pacific. The zonal velocity is shown in colour (units are in m s^{-1}). Alternating jet patterns can be seen inside the green boxes.

set nonlinear eddy forcing (Thompson and Richards, 2011; Chen et al., 2015). Even very gentle topographic slopes can induce jet drift. Boland et al. (2012) studied the effects of a zonally sloping topography on jet dynamics and found that jets drift meridionally and tilt with respect to the zonal direction towards the tilted isolines of the mean barotropic PV. They anticipate that the linear dynamics controls the jet drift, which is different from the explanation that the nonlinear eddy forcing causes the jet drift. It is not completely clear what controls the jet drift in different scenarios. The primary focus of this thesis to understand the jet drift mechanism.

1.3 THESIS OUTLINE

In this thesis, we seek to explore the physical mechanism that controls the jet drift over topographic slopes and investigate the impacts of the tilted, drifting jets on the overall dynamics. Similar to Boland et al. (2012), we consider a simple topography that increases linearly in the zonal direction and use the two-layer QG model forced with a uniform background vertical shear in the study. The model details are described in chapter 2. In agreement with Boland et al. (2012), tilted meridionally drifting jets are observed in our numerical simulations.

In chapter 3, we analyse the role of nonlinear eddy forcing and linear stress terms, which arise due to the tilted jets and the presence of sloping topography, in the time-

averaged dynamical PV balances. In order to separate eddies from the drifting jets, we rewrite the governing equations in a non-stationary tilted frame of reference in which the jets are purely zonal and stationary. This transformation makes it much easier to analyse the interactions between the jets and eddies in the presence of topography. Also, the jet drift speed becomes an explicit parameter in the new governing equations and this helps in studying the jet drift mechanism. It is found that the linear stress terms dominate in the time-mean PV budget and, for small slope magnitudes, the jet drift speeds are in a good agreement with the phase speeds of linear Rossby waves. The linear stress terms largely negate the effects of each other and the difference between the linear stress terms is balanced by eddy forcing. The results show that the linear dynamics have major control over the jet drift. It is further observed that the titled jets can be coupled to the imposed background vertical shear via topography and this alters the energy exchange rates between the jets and eddies.

In chapter 4, we derive the energy conservation equation in the titled frame of reference and compute energy exchanges between the jets and eddies in numerical simulations run with different slope magnitudes. We show that the tilted jets are able to gain energy directly from the imposed vertical shear and lose energy to eddies in the overall balance, which is in contrast to the case of eddy-driven zonal jets. An explanation based on the relative magnitudes of eddy vorticity and buoyancy fluxes is provided. Further, we compute eddy heat and PV diffusivities as a function of the slope magnitude. The results indicate that topography can significantly impact eddy-mean flow interactions and play an important role in guiding nonlocal energy transfers between different spatial scales.

In chapter 5, principal component analysis is used to identify the dominant modes in the numerical simulations. It is observed that, apart from the tilted jets, many large-scale modes exist, and these large-scale modes can interact efficiently and exchange energy. We analyse these interactions using two-dimensional kinetic energy spectra and discuss implications of these interactions on oceanic jets. Further, linear stability analysis is performed to study the impacts of the magnitudes of the eddy viscosity and bottom friction parameters on these nonlinear interactions.

In chapter 6, the roles of eddy relative vorticity and buoyancy flux convergences, which constitute the nonlinear eddy forcing term, in the maintenance of zonal jets are studied. These two components of eddy forcing are the main factors which control the vertical structure and strength of the jets in a system, and their relative magnitudes determine if the jets gain or lose energy to eddies. Here, we perform layer-wise analyses to assess the importance of the two factors in individual layers in systems forced with either an eastward or a westward vertical shear. It is shown that eddy momentum fluxes primarily force the jets in the layer that experiences a net positive meridional PV gradient and an explanation based on Rossby wave group velocity is proposed for the same. The thesis is concluded in chapter 7.

2

MODEL DESCRIPTION

In this thesis, we use the standard two-layer quasi-geostrophic (QG) model, which comprises of two coupled isopycnal layers and solves for the evolution of the geostrophic flow field. This is the simplest model that can support intrinsic baroclinic instability and the model is widely used to study the dynamics of large-scale flows and eddies in the atmosphere and oceans (e.g. see Holland, 1978; Haidvogel and Held, 1980; Panetta, 1993). In the oceans, density isolines tilt in the meridional direction due to the equator-to-pole temperature gradient and surface wind forcing, and this generates a vertical velocity shear governed by thermal-wind balance (see chapter 2 in Vallis, 2017). This velocity shear is generally baroclinically unstable and, consequently, mesoscale eddies grow by extracting the available potential energy due to the vertical velocity shear. This mechanism can be easily implemented in the two-layer QG model.

The large-scale flows in the atmosphere and oceans are largely in geostrophic balance, i.e., the dominant balance is between the Coriolis force and horizontal pressure gradient forces. The QG theory, which is used to predict the evolution of the geostrophic flow field in time, is based on the assumption that the rotation effects are important in the dynamics (Charney, 1948). This condition is satisfied when the ratio of the advective term to the Coriolis term in the momentum equations is smaller than one (see equation 5.3 in Vallis, 2017), i.e. Rossy number is small ($Ro = U/fL \ll 1$, where f is the Coriolis parameter, and U and L are the velocity and length scales, respectively). The QG equations are derived by using asymptotic expansion and expanding the variables in powers of small Rossby numbers in the momentum and continuity equations. Consequently, fast motions like gravity waves are filtered out from the system and the resulting equations only have a contribution from the geostrophic flow component. The full derivation of the QG equations can be found in chapter 5 in Vallis (2017).

2.1 GOVERNING EQUATIONS

We use the two-layer QG model on the β plane in the presence of bottom topography and the topographic height increases linearly in the zonal direction (see figure 2.1). In order to force the model, an eastward background flow U_b is imposed in the upper layer, which creates a uniform velocity shear in the vertical direction. The governing equations are (Vallis, 2017)

$$\frac{\partial \Pi_i}{\partial t} + J(\psi_i - \delta_{i1} U_b y, \Pi_i) = \nu \nabla^4 \psi_i - \delta_{i2} \gamma \nabla^2 \psi_i, \quad (2.1)$$

where $J(a, b)$ represents the Jacobian and t is time. Indices $i = 1$ and $i = 2$ correspond to the top and bottom layers, respectively, and δ_{ij} is the Kronecker delta. Π_i represents the layer-wise full potential vorticity (PV), which is given as

$$\Pi_i = \nabla^2 \psi_i + \epsilon_i S_i (\psi_2 - \psi_1) + (\beta + \epsilon_i S_i U_b) y + \delta_{i2} \frac{f_o}{H_2} \eta_T. \quad (2.2)$$

Here, $\epsilon_1 = -\epsilon_2 = 1$. ψ_i and $S_i = f_o^2 / g' H_i$ ($g' = g(\rho_2 - \rho_1) / \rho_1$ is the reduced gravity, where ρ_i is the layer density) represent the layer-wise velocity streamfunction and stratification parameter, respectively. β is the meridional gradient in the Coriolis parameter and f_o is the Coriolis parameter at some reference latitude. H_i is the layer thickness and η_T is the topographic height. ν and γ are eddy viscosity and bottom friction parameters, respectively.

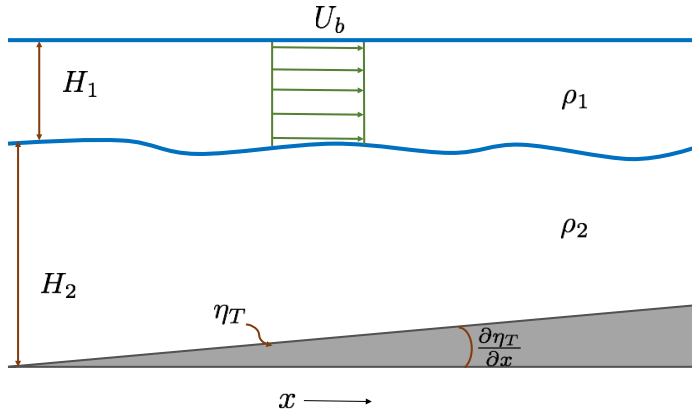


Figure 2.1: Adopted from Khatri and Berloff (2018a). Sketch of the model domain. A uniform eastward background flow U_b is imposed in the upper layer. H_i , ρ_i are the layer depth and density, respectively. η_T is the topographic height. x axis is along the zonal direction and the meridional axis y points into the sketch.

The values of the parameters used in the numerical simulations are given in table 2.1. The value of β corresponds to a reference latitude of 30° and the stratification parameter values correspond to a baroclinic Rossby radius of 25 km, which is typical

for the mid-latitudinal ocean (Chelton et al., 1998). The zonal slope magnitudes were kept small to ensure that T_x is smaller than β in magnitude and the baroclinic growth rates do not change significantly. This was necessary to maintain the computational efficiency. The change in depth over the zonal extent of the domain is smaller than the thickness of the lower layer (for the largest chosen slope, the change in depth is about 400 m). Also, the magnitude of the imposed background flow in the upper layer was chosen such that the system is baroclinically unstable for the chosen values of β and stratification parameters while maintaining the computational efficiency in the simulations. The details are discussed in the next section where we use linear stability analysis to assess the impact of the slope magnitude on the baroclinic growth rates. In numerical models, the eddy viscosity term is used to parameterise unresolved sub-grid motions and dissipate enstrophy at the grid scale. In this thesis, we mainly focus on motions having scales of greater than 100 km and the eddy viscosity term is used to parameterise the effects of motions at scales of about 10 km. In ocean models, 10^{-7} s^{-1} is generally used for the bottom friction coefficient. However, we chose relatively smaller values for the bottom drag coefficient such that the developed jets are strong and clear (see Berloff et al., 2011, for a brief discussion on the impacts of bottom friction on zonal jets). We ran a number of simulations to assess the impacts of the magnitudes of the zonal slope and dissipation parameters while keeping other parameters fixed. The results are discussed in chapters 3-5.

Parameter	Value
Domain size	$L_x = 3600 \text{ km}, L_y = 1800 \text{ km}$
Layer Depth	$H_1 = 1 \text{ km}, H_2 = 3 \text{ km}$
Background flow	$U_b = 0.06 \text{ m s}^{-1}$
Coriolis Parameter	$f_o = 7.27 \times 10^{-5} \text{ s}^{-1}$
Coriolis gradient	$\beta = 2 \times 10^{-11} \text{ m}^{-1}\text{s}^{-1}$
Stratification	$S_1 = 1.2 \times 10^{-9} \text{ m}^{-2}, S_2 = 0.4 \times 10^{-9} \text{ m}^{-2}$
Baroclinic Rosby Radius	$R_d = 25 \text{ km}$
Topographic slope term	$T_x = \frac{f_o}{H_2} \frac{\partial \eta_T}{\partial x} = 0 - 2.8 \times 10^{-12} \text{ m}^{-1}\text{s}^{-1}$
Eddy viscosity	$\nu = 50 - 200 \text{ m}^2\text{s}^{-1}$
Bottom friction	$\gamma = 1 \times 10^{-8} - 4 \times 10^{-8} \text{ s}^{-1}$

Table 2.1: Parameter values used in the numerical simulations. We ran different simulations for a range of magnitudes of T_x , ν and γ . Whenever not specified, $T_x = 1.4 \times 10^{-12} \text{ m}^{-1}\text{s}^{-1}$, $\nu = 100 \text{ m}^2\text{s}^{-1}$ and $\gamma = 2 \times 10^{-8} \text{ s}^{-1}$ were used in those cases.

2.2 BAROCLINIC INSTABILITY

In our model, mesoscale eddies grow by gaining energy from the imposed vertical velocity shear, which is baroclinically unstable. Here, we perform a linear stability analysis and compute the baroclinic growth rates as a function of the magnitudes of the background

flow in the upper layer and zonal slope. For this purpose, we derive the linear dispersion relation by substituting $\psi_i = \tilde{\psi}_i e^{i(k_x x + k_y y - \omega t)}$ in equation (2.1) and neglecting the nonlinear terms. The final linearised equations can be represented in the following matrix form

$$\begin{bmatrix} \omega(k_x^2 + k_y^2 + S_1) + k_x(\beta - U_b(k_x^2 + k_y^2)) & -S_1\omega + S_1U_bk_x \\ +i\nu(k_x^4 + k_y^4) & \\ -S_2\omega & \omega(k_x^2 + k_y^2 + S_2) - k_yT_x + k_x(\beta - U_bS_2) \\ & +i\nu(k_x^4 + k_y^4) + i\gamma(k_x^2 + k_y^2) \end{bmatrix} \begin{bmatrix} \tilde{\psi}_1 \\ \tilde{\psi}_2 \end{bmatrix} = 0, \quad (2.3)$$

where (k_x, k_y) represent the zonal and meridional wavenumbers, respectively, and ω is the frequency. For nontrivial solutions, the determinant of the matrix vanishes and results in a quadratic equation, which we solve for different wavenumber pairs (k_x, k_y) .

The baroclinic growth rates (imaginary parts of the frequency solutions) of the most unstable modes are plotted as a function of U_b for three different values of T_x in figure 2.2. It is worth noting that the system becomes unstable for eastward and westward background flows of magnitudes larger than about 0.05 m s^{-1} and 0.03 m s^{-1} , respectively. Hence, we chose $U_b = 0.06 \text{ m s}^{-1}$ in our simulations. Also, in order for the system to be baroclinically unstable, meridional PV gradients in the upper and lower layers must change sign in the vertical direction (Charney and Stern, 1962). This condition is satisfied in the cases, which have positive growth rates, as the background PV gradients in the top and bottom layers are of opposite signs. Note that, for the chosen zonal slope magnitudes, the growth rates change slightly but the change is not significant (see Chen and Kamenkovich, 2013, for details). In order to maintain the computational efficiency and have similar energy levels in the equilibrium state across different simulations, we preferred to use quite small zonal slope magnitudes in the simulations. We further discuss this aspect later in the thesis.

In figure 2.3, the real and imaginary parts of the frequency solutions are shown for a flat bottom case (top panels) as well as for a sloped topography case (bottom panels). In the flat bottom case, the growth rate maxima (ω_2^i) lie on the $k_y = 0$ line while the maxima shift to a nonzero meridional wavenumber in the presence of a zonal topographic slope. Thus, over a flat bottom, the most unstable Fourier modes are meridionally oriented, whereas the most unstable modes are slightly tilted from the meridional direction in the sloped topography case (compare the top and bottom panels in figure 2.3b). These Fourier modes correspond to mesoscale eddies, which grow via baroclinic instability and are responsible for the formation of multiple jets. The real parts of the frequency solutions represent the propagation of Rossby waves. Over a flat bottom, Rossby waves effectively propagate in the zonal direction. On the other hand, the frequency contours rotate in the case of sloped topography and this is especially clear in ω_2^r contours. Here, the direction of

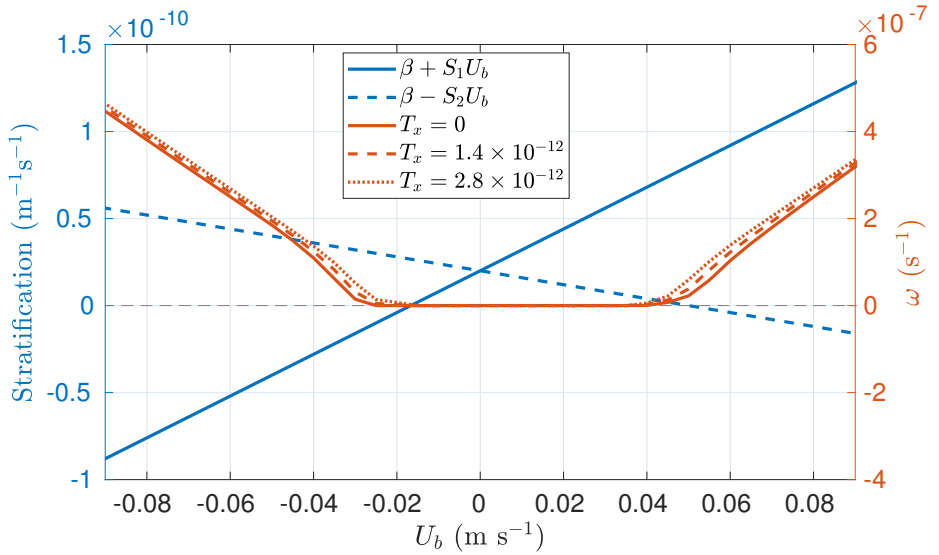


Figure 2.2: Baroclinic growth rates (red curves) of the most unstable modes for different magnitudes of U_b and T_x . For the rest of the parameters, values shown in table 2.1 were used in the computations. Blue curves represent the background PV gradients in the meridional direction in individual layers.

Rossby wave propagation is determined by the combined effect of β and T_x . This affects the orientation of multiple jets and we discuss this aspect in the next chapter.

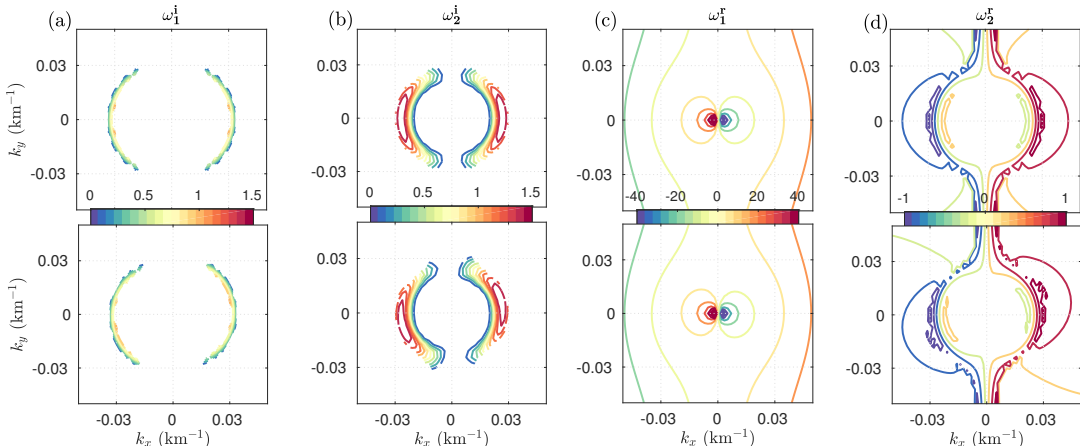


Figure 2.3: Imaginary (ω^i) and real parts (ω^r) of frequencies obtained from the dispersion relation (equation 2.3). k_x and k_y are the zonal and meridional wavenumbers, respectively. Top panels are for the flat topography case and bottom panels correspond to the zonally sloped topography case with $T_x = 1.4 \times 10^{-12} \text{ m}^{-1}\text{s}^{-1}$. For the rest of the parameters, values shown in table 2.1 were used. Colorbar units are in 10^{-7}s^{-1} . Note that the top and bottom panels have the same colorbar shown between the panels.

2.3 NUMERICAL COMPUTATIONS

In the numerical simulations, the second-order finite-difference method was used to discretise the governing equations and a flux-preserving numerical scheme called “Compact accurately boundary adjusting high-resolution technique (CABARET)” was used to integrate the solution in time. The main advantage of using CABARET is that the scheme is weakly dissipative and low in dispersion; thus, it is very effective in simulating high Reynolds number eddy-resolving flows (Karabasov et al., 2009; Karabasov and Goloviznin,

2009). The scheme is also computationally very efficient. In the numerical simulations, a rectangular domain having a grid resolution of about 7 km (512×256 grid points) was used. The grid resolution is sufficient to resolve the baroclinic instability as the fastest growing modes have zonal wavelengths of $2\pi R_d$, i.e. roughly 150 km. In the simulations, periodic boundary conditions were used on both zonal and meridional boundaries. Nevertheless, for the purpose of comparison and verification, we also ran channel simulations and few simulations with 1024×512 grid points. Note that the background flow U_b itself satisfies the governing equations. Hence, the model was initialised from a perturbed state and the perturbations grow via baroclinic instability.

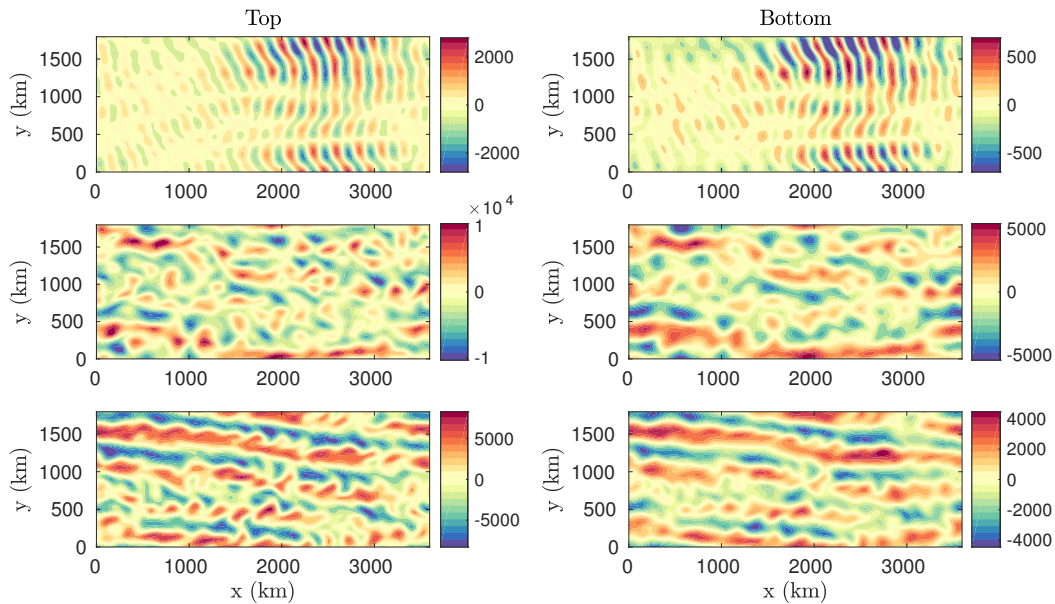


Figure 2.4: Snapshots of the streamfunction field, ψ_i (units are in $\text{m}^2 \text{s}^{-1}$), in the top (left panels) and bottom (right panels) layers at different times (top to bottom: snapshots at 600, 1000, 1400 days) over a zonally sloped topography. The simulation was run on a doubly periodic domain having 1024×512 grid points and the parameter values shown in table 2.1 were used. The core of the numerical model used in this thesis has been developed by Dr Pavel Berloff and his collaborators over the years. Topography was later included in the numerical model as a part of the research work presented in this thesis.

Snapshots of the streamfunction field in the top and bottom layers are shown in figure 2.4. The system initially develops meridionally oriented structures, which are in agreement with the linear baroclinic instability process (see figure 2.3). These meridional patterns further become unstable and transfer energy upscale resulting in the formation of alternating jets (see Berloff et al., 2009a, for details). These growing meridional patterns are generally called eddies. It is seen that, in general, meridionally oriented eddies result in anti-frictional Reynolds stresses or, in other words, the corresponding eddy momentum fluxes are up-gradient (Holloway, 2010; Srinivasan and Young, 2014). Thus, eddies force the large-scale zonal jets. We ran the simulations until the system reached a statistical equilibrium state, in which energy input due to the imposed vertical shear balances the energy loss by viscous dissipation and bottom friction. In the next chapters, we analyse momentum and energy balances to understand the impacts of the sloped topography on the dynamics of jets and eddies.

3

MECHANISM FOR JET DRIFT

The contents of this chapter have been published in the research article titled “*A mechanism for jet drift over topography*” in the *Journal of Fluid Mechanics* (Khatri and Berloff, 2018a).

Boland et al. (2012) first showed that the jets tend to tilt from the zonal direction over a zonally sloped topography and drift in the meridional direction. However, it remains unclear what causes the jet drift in this scenario. The main objective of this chapter is to understand the physical mechanism that controls the jet drift. For this purpose, we study the jet dynamics in the two-layer quasi-geostrophic (QG) numerical solutions run with different zonal slope magnitudes. We compare the jet drift speeds with predictions from the linear dispersion relation as well as examine the role of nonlinear eddy effects in the maintenance of the jets. In particular, we assess the impacts of the time-mean cross-jet profiles of eddy forcing, meridional eddy fluxes on the mean flow in the energy equilibrium state in a non-stationary, tilted frame of reference propagating with the tilted jets.

3.1 JET DYNAMICS IN THE EQUILIBRIUM STATE

We first analyse the jet dynamics in the statistical equilibrium state. In figure 3.1, snapshots and Hovmöller diagram of the potential vorticity (PV) anomaly field are shown for three simulations run with different zonal slope magnitudes ($T_x = 0.83 \times 10^{-12}$, 1.4×10^{-12} and $2.8 \times 10^{-12} \text{ m}^{-1}\text{s}^{-1}$ were used in the simulations). In this chapter, these simulations are referred to as ‘small-slope’, ‘medium-slope’ and ‘large-slope’, respectively. In agreement with Boland et al. (2012), the jets tilt from the zonal direction and propagate meridionally. We observed that the tilt angle, as well as the drift speed, increases with

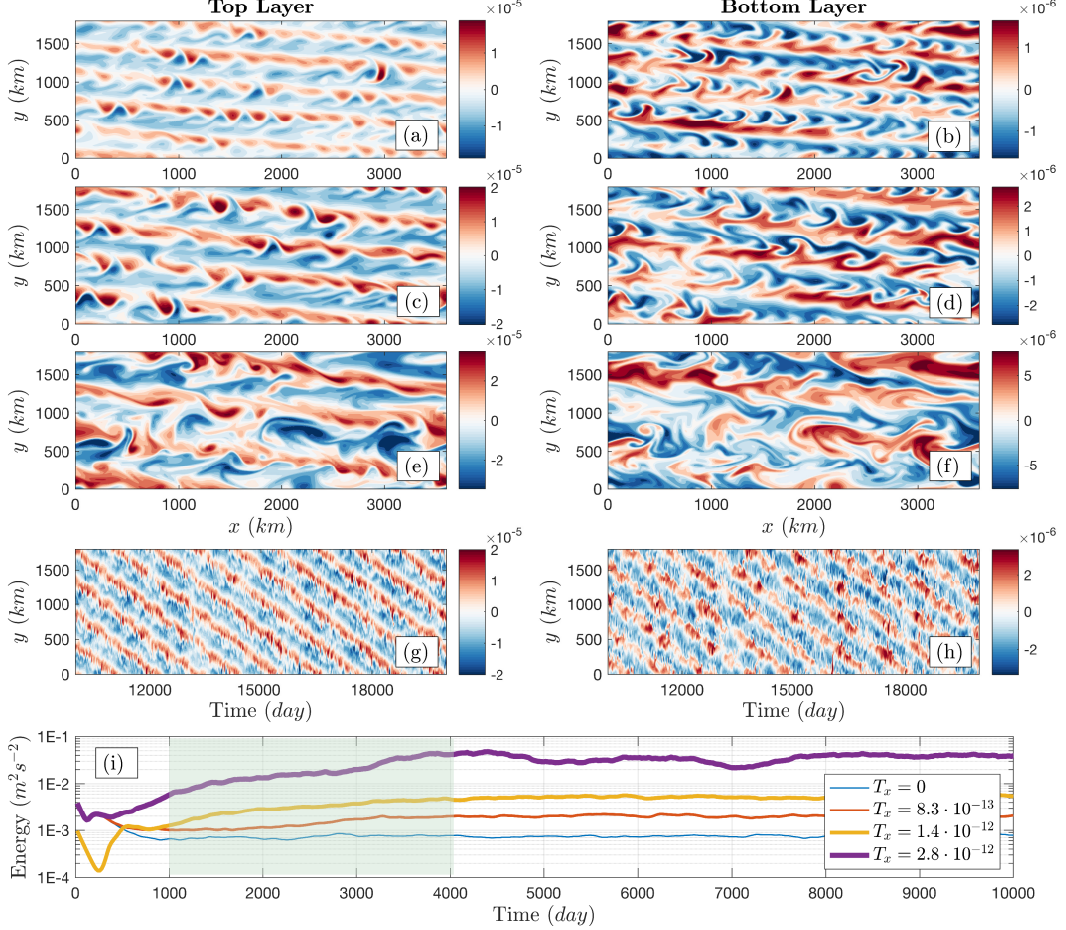


Figure 3.1: Adopted from Khatri and Berloff (2018a). Jet flow patterns in the equilibrium state; (a-f): Snapshots of the PV anomaly field in the top layer ($\nabla^2\psi_1 + S_1(\psi_2 - \psi_1)$) and bottom layer ($\nabla^2\psi_2 + S_2(\psi_1 - \psi_2)$) from three different simulations run with $T_x = 0.83 \times 10^{-12}$, 1.4×10^{-12} and $2.8 \times 10^{-12} \text{ m}^{-1}\text{s}^{-1}$, respectively (colorbar units are in s^{-1}); (g,h): PV anomaly Hovmöller diagrams in the top and bottom layers (a meridional cross-section of PV anomaly at the centre of the domain is plotted against time for the medium-slope simulation); (i): Total energy time series in the three simulations (for reference, energy time series for a flat bottom case $T_x = 0$ is shown). The jet tilt angles are 5.71° , 7.13° , 9.46° and southward drift speeds are 0.20 , 0.48 , 0.74 cm s^{-1} , respectively.

increasing the slope magnitude. The jets tilt in response to the tilted PV isolines due to the sloped topography (Boland et al., 2012). Over a flat bottom, the background PV gradient due to the planetary vorticity is directed in the meridional direction only and Rossby waves propagate in the east-west direction (see figure 2.3). As a result, alternating jets are always zonal and parallel to the mean PV isolines. In the presence of a zonally sloped topography, the zonal component of the PV gradient is nonzero and this affects the Rossby wave propagation direction resulting in titled jets. For example, in a barotropic model, the jet tilt angle can be estimated as $\tan^{-1}(\frac{T_x}{\beta})$.

In the two-layer QG model, the dynamics are more complex and the jet tilt is determined by the combined dynamics of both layers. Here, the background PV gradient in the upper layer ($\nabla[f_o + (\beta + S_1 U_b)y]$) is purely meridional, whereas the background PV gradient in the lower layer ($\nabla[f_o + (\beta - S_2 U_b)y + T_x x]$) has both zonal and meridional components. Thus, PV gradients in the top and bottom layers do not have the same

orientation. It has been observed that, in a two-layer QG model, the jets tend to align with the mean barotropic PV isolines (Boland et al., 2012). The tilt angle of the barotropic PV isolines from the zonal direction is given as

$$\theta = \tan^{-1} \left(\frac{H_2 T_x}{(H_1 + H_2) \beta} \right). \quad (3.1)$$

In our simulations, the jet tilt angles are 5.71° , 7.13° and 9.46° in the three cases. These tilt angles are larger than the tilt angles estimated using equation (3.1), which are 1.78° , 3.01° and 5.99° . One of the reasons for the mismatch is the use of periodic boundary conditions in the simulations, which restrict the jets to tilt at specific angles and require the jet pairs to be evenly spaced. Note that the spatial structures of the PV anomaly field in the top and bottom layers are significantly different. This is because the layer-wise PV gradients are not oriented in the same direction and the mean PV isolines in the upper and lower layers are not parallel. In contrast, the jets in the top and bottom layers are perfectly aligned with each other. As a result, the jets cross the layer-wise mean PV isolines, which leads to the differences in the PV spatial structure. In float observations and ocean models, tilted jets are also seen to have tilt angles of about $5^\circ - 10^\circ$ (Melnichenko et al., 2010; Van Sebille et al., 2011).

Moreover, the jets drift in the meridional direction (see Hovmöller diagram in figure 3.1). For positive (negative) values of T_x , the jets drift southwards (northwards). The jets propagate with nearly constant speeds and, in the numerical solutions, the jet propagation speeds in the direction perpendicular to jets' phase lines are about 0.20, 0.48, and 0.74 cm s^{-1} . We computed the exact drift velocities by applying principal component (PC) analysis to the streamfunction field in the equilibrium state. We decomposed the streamfunction field into a set of orthogonal patterns (refer Hannachi et al., 2007, for a brief review of the technique). The drifting jets are captured by the first two empirical orthogonal functions (EOFs) and the power spectra of the corresponding PCs peak at a single frequency (figure 3.2). This frequency peak corresponds to the jet drift velocity. We then used the peak frequency ω and the wavevector \mathbf{k} corresponding to the tilted jets to compute the drift velocity by using the following relation:

$$\mathbf{c} = \frac{\omega}{|\mathbf{k}|^2} \mathbf{k}, \quad (3.2)$$

where \mathbf{c} is the jet drift velocity and $\mathbf{k} = \frac{2\pi}{L_x} \hat{i} + \frac{2\pi n}{L_y} \hat{j}$ (n represents the number of jet pairs, and \hat{i} , \hat{j} represent the zonal and meridional unit vectors, respectively).

Another important aspect to note is that the system takes a long time to attain an energy equilibrium state (figure 3.1*i*), which is in contrast to the case of zonal jets over a flat bottom. Although the system develops multiple jets in the simulations by 1,000 days (see figure 2.4), the total energy continuously increases until about 4,000

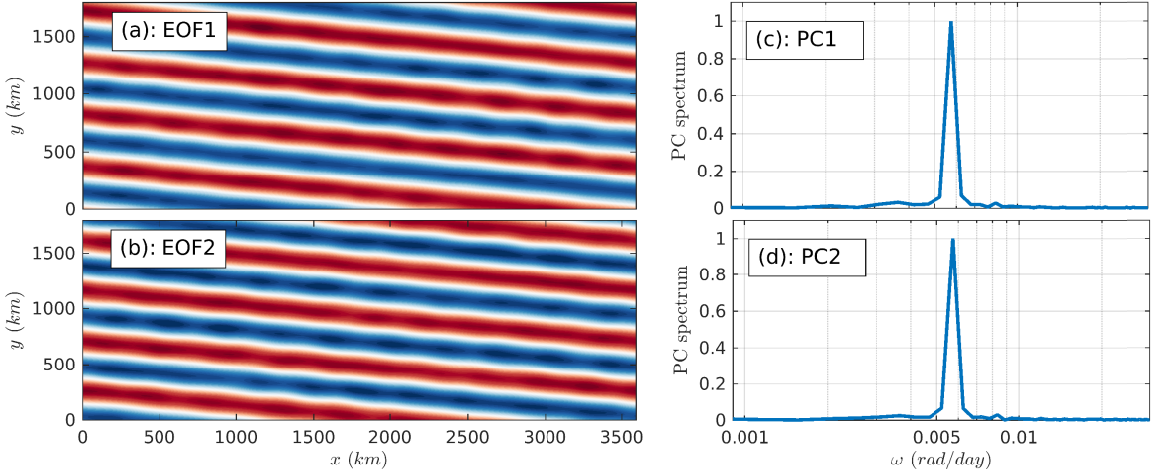


Figure 3.2: Adopted from Khatri and Berloff (2018a). EOF analysis of the streamfunction field in the medium-slope simulation (data for the last 10,000 days, i.e. 500 snapshots, in the simulation was used for the EOF analysis); (a,b): EOF 1-2 in the top layer (colorbar range is [-1 1]); (c,d): Power spectra (normalised to unity) of the PCs corresponding to these EOFs. One could think of drifting jets as a propagating wave. We know that a propagating wave can be represented with two EOFs, which are identical but with a phase shift of $\pi/2$, and their PCs continuously oscillate between the maximum and minimum values to reflect the propagation. Thus, the power spectra of the PCs show distinct peaks in the frequency space. The wavevector \mathbf{k} and peak frequency ω corresponding to the EOFs can be used to compute the jet drift velocity as $\mathbf{c} = (\omega/|\mathbf{k}|^2)\mathbf{k}$.

days before reaching statistical equilibrium. Also, the total energy ($\frac{1}{2A} \int_A [H_1 |\nabla \psi_1|^2 + H_2 |\nabla \psi_2|^2 + H_1 S_1 (\psi_1 - \psi_2)^2]$, where A is the domain area, and note that $H_1 S_1 = H_2 S_2$) in the equilibrium state increases with the zonal slope magnitude; however, there is a negligible change in the baroclinic growth rates for the chosen slope magnitudes (figures 2.2-2.3). We further discuss these aspects later in this chapter. We ran the simulations for 20,000 days and used the data of the last 10,000 days (i.e. 500 snapshots) for the analysis discussed in this chapter. In our simulations, Rossby number is about 0.01 at length scales of 100 km as velocities are of order of 0.1 m s^{-1} and this agrees with the typical velocity and length scales in the oceans. Hence, it is appropriate to study the jet dynamics in a QG model.

We ran a number of simulations with different horizontal resolution and domain size, and did not observe any significant change in the jet tilt angles and drift speeds. We also ran channel simulations (see appendix B.1 for details), where we used partial-slip boundary conditions on the meridional boundaries and also ensured no-normal flow on the meridional boundaries. The partial-slip boundary conditions are used to parameterise unresolved near-boundary processes (Berloff and McWilliams, 1999). In these simulations too, we found tilted, drifting jets. However, the dynamics become quite complicated in the presence of meridional boundaries, as secondary circulations develop along the boundaries. We do not study the impacts of these secondary circulations in this thesis and focus on the dynamics of jets and eddies in doubly-periodic domains.

For the choice of parameter values, only 3-5 jet pairs are formed in the whole domain and, as a consequence, jets can have only certain tilt angles allowed by periodic boundaries. Given this, the jet tilt angles and drift speeds in doubly-periodic simulations tend to be greater than in channel simulations. These artefacts could be minimised by using a very large domain, as it would increase the number of jet pairs in the domain. However, it would require significantly more computational resources. The primary aim of this work is to understand the jet drift mechanism and investigate how large-scale dynamics is affected by topography. Hence, the choice of a doubly periodic domain is reasonable.

It is worth mentioning that, in many places in the oceans, alternating jets experience steep topography, where the topographic gradients are much larger than the slope magnitudes considered here. The results of this work may not apply to those situations directly. With this work, we intend to understand jet dynamics in mid-oceans over slowly varying topography and away from continental boundaries. Also, note that topographic impacts are significantly enhanced in the two-layer QG model because topography affects the motion of the full lower layer, which is 3 km deep in our model. It is expected that, in real oceans or continuously stratified models, the topographic slope magnitudes chosen in this work would result in smaller jet tilt angles and drift speeds than the ones observed in our simulations.

3.2 DRIFT VELOCITIES FROM THE LINEAR DISPERSION RELATION

In general, both linear dynamics and nonlinear eddy effects can induce jet drift. We first analyse the role of the linear dynamics. In this section, we compare the jet drift velocities, which we computed using the linear dispersion relation, with the jet drift observed in the fully nonlinear numerical solutions. In particular, we used equation (2.3) to compute frequencies of the Fourier modes matching the jets in the simulations. We found that the real parts of these frequencies are nonzero. This means that, even in the linear system, tilted Fourier modes propagate. We then computed the phase velocities of these Fourier modes using equation (3.2)*. These phase velocities, as well as the jet drift velocities estimated from the simulations, are shown in table 3.1. The estimates from the dispersion relation match well with the drift speeds in the fully nonlinear simulations and the effects of eddies on the jet drift is quite small. The eddies seem to act against the jet drift, as the observed drift speeds are slightly smaller than the predictions from the dispersion relation. This difference is more for steeper zonal slopes and is about 30% in the large-slope simulation. These comparisons indicate that jet drift speeds can be estimated

*Equation (2.3) results in two frequency solutions for each wavenumber pair (k_x, k_y) . Thus, for each wavenumber, there are two different drift velocities, which are directed in opposite directions and are of different magnitudes. In order to compare the jet drift velocities, we considered the frequency solution predicting the same drift direction as seen in the simulations.

from the linear dispersion relation, at least for small slope magnitudes. However, in cases where T_x and β are similar in magnitude, tilted jets may not follow the phase speeds of linear Rossby waves. Although the jet formation is a strongly nonlinear phenomenon, the linear dynamics has strong control over the large-scale flow (Berloff and Kamenkovich, 2013a,b). Over a flat bottom, the linear dynamics predicts the presence of stationary zonal eigenmodes, which correspond to zonal jets. However, tilted eigenmodes are not stationary and propagate with constant velocities, and this property agrees well with the numerical simulations. Eddies also affect the jet drift, which is discussed in the next section.

T_x (m $^{-1}$ s $^{-1}$)	Drift: Simulations	Drift: Dispersion Relation
0.83×10^{-12}	$-0.02\hat{i} - 0.21\hat{j}$	$-0.02\hat{i} - 0.23\hat{j}$
1.4×10^{-12}	$-0.06\hat{i} - 0.47\hat{j}$	$-0.06\hat{i} - 0.53\hat{j}$
2.8×10^{-12}	$-0.12\hat{i} - 0.73\hat{j}$	$-0.18\hat{i} - 1.06\hat{j}$

Table 3.1: Jet drift velocity (cm s $^{-1}$) estimates from the numerical simulations and dispersion relation. \hat{i} and \hat{j} represent the unit vectors in the zonal and meridional directions, respectively.

3.3 NONLINEAR EFFECTS AND THE ROLE OF EDDIES

Mesoscale eddies, which gain energy from the available potential energy through baroclinic instability, exchange momentum and buoyancy with the large-scale flow and affect the jet dynamics. The impacts of these exchange processes on the jets can be studied by comparing the cross-jet profiles of eddy forcing and time-mean PV. In the case of stationary zonal jets, the nonlinear eddy stress terms can be analysed by decomposing the flow field into the time-mean large-scale flow and eddies (e.g. Panetta, 1993; Berloff et al., 2009a). However, in the case of drifting jets over the sloped topography, the large-scale flow itself is time-dependent and it is difficult to separate eddies from the jets. To overcome this issue, we used a frame of reference propagating with the tilted jets such that the jets appear stationary and zonal. In this configuration (figure 3.3), the speed of the frame of reference c and tilt angle θ correspond to the jet drift speed and tilt angle, respectively, which we estimated from the simulations. We rewrote the governing equation (2.1) in the new drifting, rotated frame of reference. By doing this, we do not violate the PV conservation as the new frame of reference does not accelerate. The new governing equations are (see derivation in appendix A.1 and note that $\psi_i = \psi_i(p, q, t)$):

$$\left[\frac{\partial}{\partial t} - c \frac{\partial}{\partial q} \right] \Pi_i = - \left(\frac{\partial \psi_i}{\partial p} - \delta_{i1} U_b \sin \theta \right) \frac{\partial \Pi_i}{\partial q} + \left(\frac{\partial \psi_i}{\partial q} - \delta_{i1} U_b \cos \theta \right) \frac{\partial \Pi_i}{\partial p} + \nu \nabla^4 \psi_i - \delta_{i2} \gamma \nabla^2 \psi_i, \quad (3.3)$$

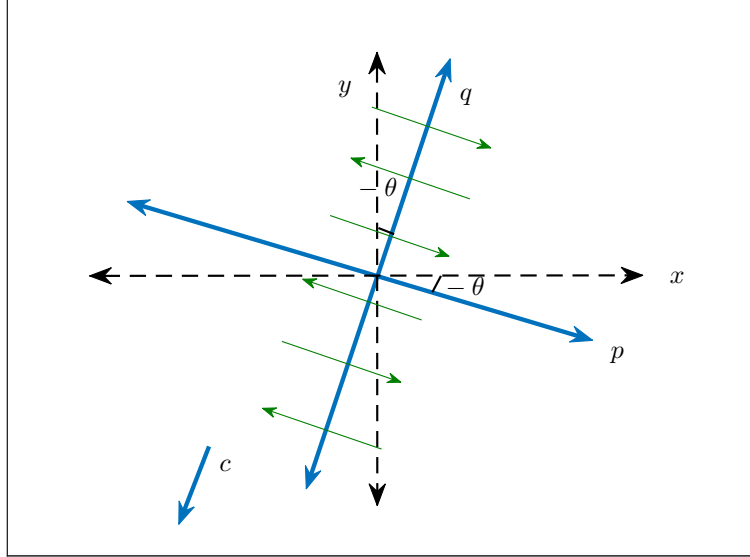


Figure 3.3: Adopted from Khatri and Berloff (2018a). New coordinate system (p, q are the new axes), which is at an angle θ (positive for anticlockwise rotation) from the original xy coordinate system and is propagating with speed c (positive in q direction). θ and c correspond to the jet tilt angle and drift speed, respectively, estimated from the numerical solutions. Alternating jets are represented with green arrows and the time-mean profile of the jets depends on q only.

where

$$\left. \begin{aligned} \Pi_1 &= \overbrace{\nabla^2 \psi_1 + S_1(\psi_2 - \psi_1)}^{Q_1} + (\beta + S_1 U_b)(q \cos \theta + p \sin \theta + ct \cos \theta), \\ \Pi_2 &= \overbrace{\nabla^2 \psi_2 + S_2(\psi_1 - \psi_2)}^{Q_2} + (\beta - S_2 U_b)(q \cos \theta + p \sin \theta + ct \cos \theta) \\ &\quad + T_x(-q \sin \theta + p \cos \theta - ct \sin \theta). \end{aligned} \right\} \quad (3.4)$$

Here, Π_i is the layer-wise absolute PV, which is the sum of Q_i (PV of the generated flow) and the background PV. Also, all variables are functions of spatial directions (p, q) and time. $\nabla = (\frac{\partial}{\partial p}, \frac{\partial}{\partial q})$ and δ_{ij} is the Kronecker delta. The first two terms on the right-hand side (RHS) of equation (3.3) capture the PV generation by the imposed background flow and PV redistribution by eddies. The rest of the terms on the RHS are viscous dissipation and bottom drag terms, which remove enstrophy and energy from the system. The role of these terms can be assessed in the time-mean PV balances, which we derived from equation (3.3). We used Reynolds-style decomposition in the moving frame of reference to represent the variables as a sum of the time-mean flow ($\bar{Q}_i, \bar{\psi}_i$) and transient eddies (Q'_i, ψ'_i), and further averaged the equations over time (complete derivation can be found in appendix A.2). The layer-wise time-averaged equations are:

$$\frac{\partial \bar{Q}_1}{\partial t} = \underbrace{-\nabla \cdot (\bar{\mathbf{u}}'_1 \bar{Q}'_1)}_{\text{Eddy Forcing}} + \underbrace{(c + U_b \sin \theta) \frac{\partial \bar{Q}_1}{\partial q}}_{\text{Linear Stress Terms}} - \underbrace{(\beta + S_1 U_b) \sin \theta \cdot \bar{u}_1}_{L_1^m} + \underbrace{\nu \nabla^2 \bar{\zeta}_1}_{D_1^\nu}, \quad (3.5)$$

$$\frac{\partial \bar{Q}_2}{\partial t} = \underbrace{-\nabla \cdot (\bar{\mathbf{u}}'_2 \bar{Q}'_2)}_{\text{Eddy Forcing}} + \underbrace{c \frac{\partial \bar{Q}_2}{\partial q}}_{L_2^c} - \underbrace{[(\beta - S_2 U_b) \sin \theta + T_x \cos \theta] \cdot \bar{u}_2}_{L_2^m} + \underbrace{\nu \nabla^2 \bar{\zeta}_2}_{D_2^\nu} - \underbrace{\gamma \bar{\zeta}_2}_{D_2^\gamma}, \quad (3.6)$$

where \mathbf{u}_i represents the velocity field ($\mathbf{u}_i = (u_i, v_i) = (-\partial \psi_i / \partial q, \partial \psi_i / \partial p)$) and ζ_i is the relative vorticity ($\zeta_i = \nabla^2 \psi_i$) in each layer. Note that the terms containing time derivatives of the mean PV (in the rest of the chapter, “mean PV” refers to the time-mean PV due to the developed flow only, i.e. \bar{Q}_i) vanish in the energy equilibrium state and are kept just for clarity. It is clear from equations (3.5-3.6) that, in the statistical equilibrium state, the nonlinear terms (referred to as “eddy forcing” or “nonlinear stress terms”, hereafter) and linear terms (“linear stress terms”: $L_i^c + L_i^m$, and “dissipation terms”: $D_i^\nu + D_i^\gamma$) balance each other. We analyse the role of these linear and nonlinear stress terms by comparing their cross-jet profiles.

In order to compute the stress terms, we used linear interpolation to interpolate the streamfunction field on the rotated pq coordinate system at every time step and then aligned these individual snapshots in the moving frame of reference. We then computed eddy forcing and linear terms present on the RHS in equations (3.5-3.6). We further averaged these terms over time and in the direction along the jets to create the cross-jet profiles (shown in figure 3.4 for the medium-slope simulation). As expected, the linear and nonlinear stress terms largely cancel[†] each other (figure 3.4a,b). We also examine the relative contributions of the individual linear terms (see figure 3.4c,d), which contribute to the net linear stress terms. In the top layer, L^c and L^m terms (hereafter we refer to these as “radiation stress term” and “inertial stress term”, respectively) are roughly four times in magnitude than the magnitude of the eddy forcing term in the top layer. On the other hand, linear stress terms and nonlinear stress terms are of similar strength in the bottom layer. The radiation and inertial stress terms are in opposite phases; hence, they compensate for each other and the difference is balanced by the eddy forcing term. The contribution of the dissipation terms is quite small, so we neglect the dissipation terms in the rest of the analysis. These observations support our hypothesis that the linear

[†]Linear interpolation leads to small deviations from zero and a higher-order interpolation scheme could be used for better accuracy. However, linear interpolation was found to be sufficient here. In order to verify the results, the stress terms were also evaluated in the original xy coordinate system and the stress fields were then interpolated in the moving frame of reference. There were no significant differences.

dynamics can be used to understand the jet drift in our simulations.

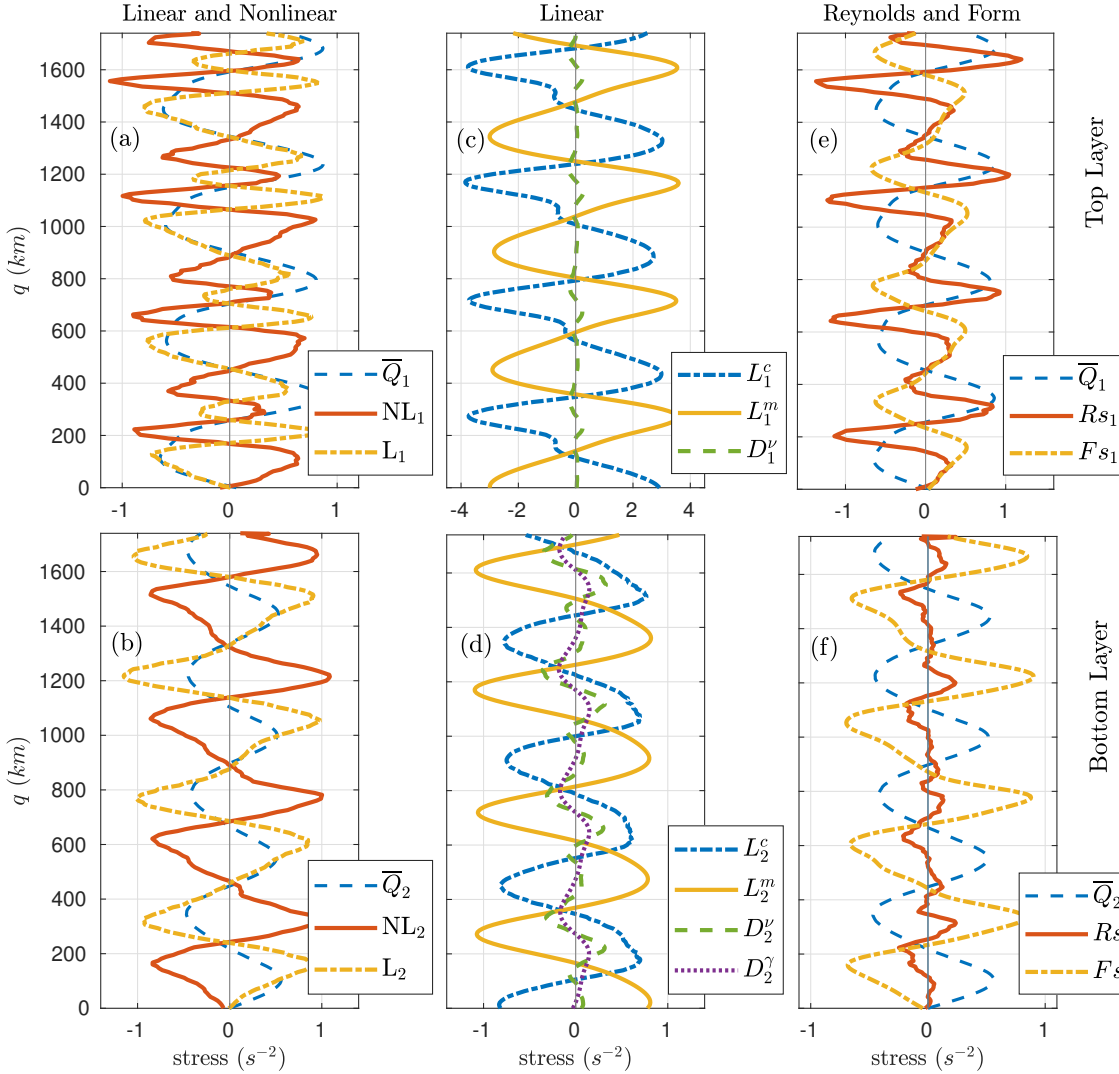


Figure 3.4: Adopted from Khatri and Berloff (2018a). Time-mean cross-jet profiles for the medium-slope simulation; (a,b): eddy forcing (NL_i) and linear stress terms + dissipation terms (L_i); (c,d): radiation stress term (L_i^c), inertial stress term (L_i^m), and dissipation terms (D_i^ν , D_i^γ); and (e,f): Reynolds stress term (Rs_i) and form stress term (Fs_i). The cross-jet profiles of the Reynolds stress term and form stress term were smoothed with 10-point moving averages. The profiles were averaged in the moving frame in the interval 10,000-20,000 days. Top and bottom panels are for the upper and lower layers, respectively. The stress terms (units are in s^{-2}) were normalised by multiplying them to factors of 5×10^{12} and 2×10^{13} in the upper and lower layers, respectively. The time-mean PV profiles (\bar{Q}_i , normalised) are denoted with dashed blue curves (a,b,e,f) and were multiplied by factors of 2.2×10^5 and 8.8×10^5 in the upper and lower layers, respectively.

It is quite interesting that, in both layers, the linear stress terms are in phase with the mean PV profiles while the eddy forcing terms tend to smoothen the PV profiles (figure 3.4a,b). As shown in table 3.2, the linear stress terms show a strong positive correlation (~ 0.6) with the time-mean PV, whereas the eddy forcing is negatively correlated with the time-mean PV (correlation coefficient ~ -0.3). This indicates that the jets are forced by the linear stress terms and eddies act to weaken the jets. Previous works on zonal jet formation in the oceans and planetary atmospheres have shown that eddies drive the jets (Ingersoll et al., 1981; Panetta, 1993; Ingersoll et al., 2000; Berloff et al., 2009a,b; Chen et al., 2015). However, the correlation coefficients in table 3.2 suggest the opposite. In

order to clarify this issue, we computed the Reynolds stress term Rs and form stress term Fs (eddy forcing is the sum of the Reynolds stress term and form stress term):

$$Rs_i = -\nabla \cdot \overline{(\mathbf{u}'_i \zeta'_i)}, \quad (3.7)$$

$$Fs_i = -\epsilon_i S_i \nabla \cdot \overline{(\mathbf{u}'_i (\psi'_2 - \psi'_1))}, \quad (3.8)$$

where $i = 1, 2$ represent the upper and lower layers, respectively, and $\epsilon_1 = -\epsilon_2 = 1$. The rest of the variables are the same as defined in equations (3.5-3.6).

As seen in figure 3.4(e,f), the Reynolds stress term and form stress term have opposite effects on the mean PV profile. The Reynolds stress term tends to make the mean PV profile sharper in the top layer; however, we do not observe any clear impact of the Reynolds stress term in the bottom layer (see the correlation coefficients in table 3.2). This indicates that the Reynolds stress term forces the jets mainly in the upper layer (see also the discussion in Thompson and Young, 2007; Khatri and Berloff, 2018b). We study this aspect in detail in chapter 6. On the other hand, the form stress term tends to smoothen the mean PV profile as the form stress term and mean PV profiles are negatively correlated in both layers (see the correlation coefficients in table 3.2). This is because eddies gain energy from the available potential energy of the mean flow and act to reduce the vertical shear in the system. As a result, the form stress term is anti-correlated to the mean PV. These observations are in agreement with theoretical aspects. In a system forced with an eastward background vertical shear, we expect the form stress term to act against the mean PV in both layers and the Reynolds stress term to force the jets in the upper layer (Berloff et al., 2009a; Khatri and Berloff, 2018b).

Layer	Linear ($L_i^c + L_i^m$)	Eddy ($Rs_i + Fs_i$)	Reynolds (Rs_i)	Form (Fs_i)
Top ($i = 1$)	0.60	-0.24	0.26	-0.93
Bottom ($i = 2$)	0.86	-0.33	-0.01	-0.89

Table 3.2: Correlation coefficients between the time-mean cross-jet profiles of the linear and nonlinear stress terms, and the mean PV (\overline{Q}_i) in both layers for the medium-slope simulation. The jets are forced by the linear stress terms while eddies act against the jets.

Note that the Reynolds stress term and form stress term are of comparable magnitudes in the top layer (figure 3.4e). In the case of zonal jets over a flat bottom, the Reynolds term is generally much stronger than the form stress term in the top layer and, in the overall balance, eddy forcing tends to make the mean PV profile sharper; thus, eddies force the jets. However, in the presence of the sloped topography, the effect of the form stress term is more prominent and, in fact, it overcomes the Reynolds stress term in the upper layer. As a result, eddies act against the jets and gain energy from the jets, which are forced by the linear stress terms. Kamenkovich et al. (2009) studied the dynamics of multiple jets in the North Atlantic ocean and found evidence of both kinds

of eddy feedbacks (also see Melnichenko et al., 2010; Barthel et al., 2017; Youngs et al., 2017). It is important to note that if the Reynolds decomposition is used in a stationary frame of reference to compute eddy field, then eddies would also include the contribution from the drifting jets; thus, eddy forcing would include the terms interpreted as linear stress terms in this work. This could make it difficult to compare our results to earlier studies.

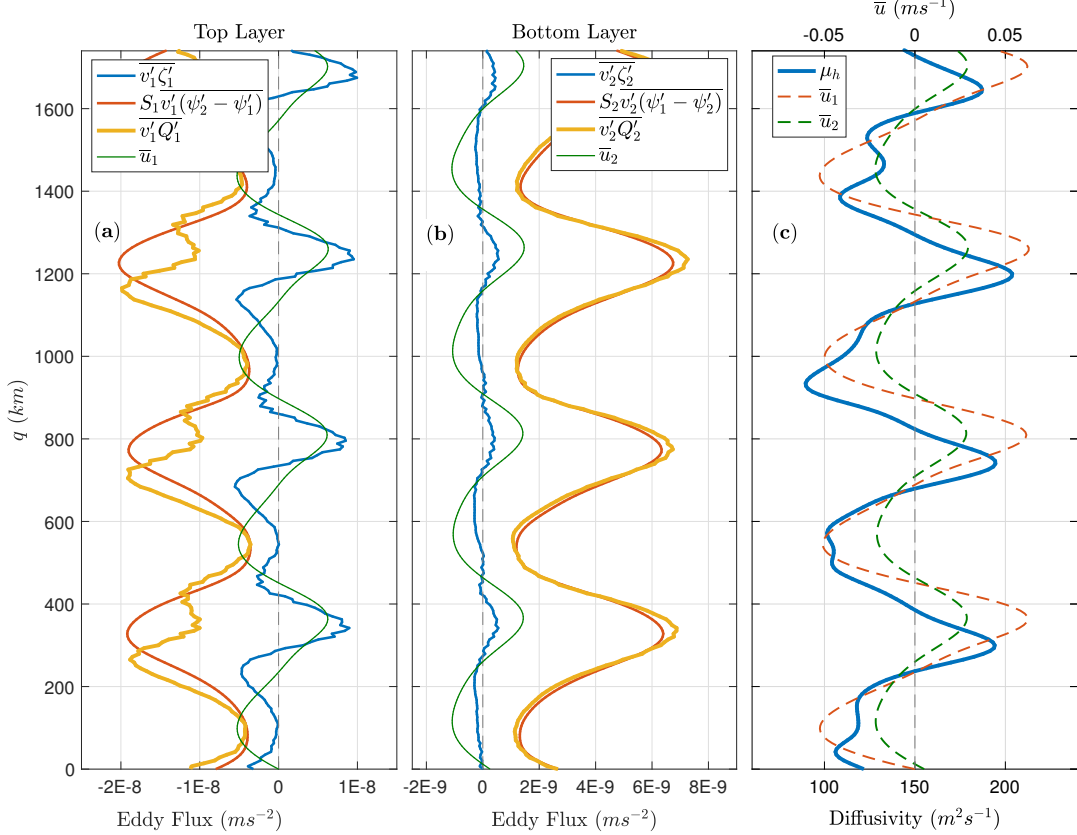


Figure 3.5: Adopted from Khatri and Berloff (2018a). Time-mean cross-jet profiles for the medium-slope simulation; (a,b): Eddy relative vorticity flux $\overline{v'_i \zeta'_i}$, eddy buoyancy flux $\epsilon_i S_i \overline{v'_i (\psi'_2 - \psi'_1)}$ and eddy PV flux $\overline{v'_i Q'_i}$; (c): Heat diffusivity. The profiles were averaged in the moving frame in the interval 10,000–20,000 days. The green curves in (a,b) represent the mean flow (normalised), and the actual velocity magnitudes are shown in (c).

We also computed the cross-jet profiles of layer-wise eddy PV fluxes ($\overline{v'_i Q'_i}$), eddy relative vorticity fluxes ($\overline{v'_i \zeta'_i}$) and eddy buoyancy fluxes ($\epsilon_i S_i \overline{v'_i (\psi'_2 - \psi'_1)}$) across the jets (figure 3.5a,b). The eddy buoyancy fluxes (also called as “eddy heat fluxes”) contribute the most to the eddy PV fluxes. Here, eddies transport buoyancy and PV anomalies southwards (northwards) in the top (bottom) layer. We further computed eddy heat diffusivity μ_h :

$$\mu_h = \frac{\epsilon_i S_i \overline{v'_i (\psi'_2 - \psi'_1)}}{-\partial_q \bar{b}_i} = \frac{\epsilon_i S_i \overline{v'_i (\psi'_2 - \psi'_1)}}{-\partial_q (\epsilon_i S_i (\bar{\psi}_2 - \bar{\psi}_1) + \epsilon_i S_i U_b q \cos \theta)} = \frac{\overline{v'_i (\psi'_2 - \psi'_1)}}{\bar{u}_2 - \bar{u}_1 - U_b \cos \theta}, \quad (3.9)$$

where \bar{b}_i is the layer-wise time-mean buoyancy and other notations are the same as in

equations (3.7-3.8). Although the expressions for the heat diffusivity are different in individual layers, they are mathematically equivalent and the computed cross-jet profiles of the layer-wise heat diffusivity are the same. As seen in figure 3.5c, the heat diffusivity is positive at all latitudes. Hence, the eddies advect buoyancy anomaly down-gradient, which leads to smoothening of the PV gradients. Also, note that the maxima (minima) in the heat diffusivity profile roughly coincide with the eastward (westward) jets. Since the eddy flux is at maximum in the eastward jet cores, the dynamics do not agree with the theory of barotropic “PV staircases”, which predict reduced eddy transport across eastward jets (e.g. Dritschel and McIntyre, 2008). The eddy relative vorticity fluxes, on the other hand, are positively correlated with the mean flow (figure 3.5a,b); thus, they force the jets or, in other words, eddy relative vorticity fluxes are up-gradient. Overall, the behaviour of these fluxes is the same as seen in zonal jets over a flat bottom (Panetta, 1993; Thompson and Young, 2007). Only the relative contributions of the eddy relative vorticity and buoyancy fluxes to the eddy PV fluxes change because of the presence of the sloped topography. The magnitude of the heat diffusivity is significantly affected by the zonal slope magnitude and we analyse this aspect in the next chapter.

As discussed above, in the presence of the topography, the form stress term dominates over the Reynolds stress term and, in the overall balance, eddies tend to act against the jets. In order to observe the change in the eddy behaviour from being jet-supporting to jet-opposing more clearly, the correlation coefficients between the eddy forcing and mean PV profiles were computed in simulations run with different zonal slope magnitudes (table 3.3). The correlation in the top layer changes from a positive value to negative values with increasing the slope magnitude. This shows that, over a flat bottom, eddies support the jets, whereas eddies tend to act against the jets over a sloped topography due to an increase in the strength of the form stress term. Note that, in the bottom layer, the correlation is always negative. This is because, in the bottom layer, the eddy forcing is dominated by the form stress term (Thompson and Young, 2007; Khatri and Berloff, 2018b) and the mean PV has the majority of the contribution from the buoyancy term, $S_2(\bar{\psi}_1 - \bar{\psi}_2)$. Since the eddy buoyancy fluxes are always down-gradient, the correlation is always negative in the bottom layer. We discuss the role of layer-wise eddy fluxes in detail in chapter 6. It is important to note here that the computed critical slope magnitude, at which the correlation changes the sign, is not unique and strongly depends on the chosen parameter values. The critical slope may also be affected by the imposed periodic boundary conditions in the model.

The analyses of the eddy forcing and eddy PV fluxes show that the vertical flow structure is a major factor that decides the impact of eddies on the large-scale flow. Our hypothesis is that the primary role of eddies here is to stabilise the system by either forcing or acting against the jets. In the case of zonal jets over a flat bottom, eddies deposit momentum into the jets and counteract the viscous dissipation and bottom friction. On

T_x	0	0.55×10^{-12}	0.83×10^{-12}	1.4×10^{-12}	1.94×10^{-12}	2.8×10^{-12}
Top	0.67	0.24	-0.07	-0.24	-0.64	-0.56
Bottom	-0.52	-0.82	-0.84	-0.33	-0.97	-0.66

Table 3.3: Correlation coefficients between the cross-jet profiles of the time-mean layer-wise eddy forcing ($EF_i = Rs_i + Fs_i$, where $i = 1$ and $i = 2$ indicate the top and bottom layers, respectively) and the time-mean PV (\bar{Q}_i) as a function of the zonal slope magnitude (T_x units are in $m^{-1}s^{-1}$). For the rest of the parameters in the numerical simulations, values shown in table 2.1 were used.

the other hand, over a sloped topography, the tilted jets are directly forced by the inertial stress term L^m and eddies remove energy from the jets to compensate for the linear forcing. This way, eddies help in stabilising the system.

3.4 JET DRIFT MECHANISM

On the basis of the analysis in the previous sections, we argue that the jet drift is mainly controlled by the linear dynamics in our simulations. This can be understood by examining the linear stress terms in equations (3.5-3.6) more closely. The inertial stress term L_i^m , which directly forces the jets by sharpening the mean PV profile, is proportional to the mean along-jet velocity in each layer. By construction, the absolute maxima of \bar{u}_i and \bar{Q}_i are not aligned and have a large offset. In a similar manner, the cross-jet profiles of the radiation stress term L_i^c , which counteracts the inertial stress term, and mean PV are also significantly offset. In fact, the profiles of L_i^c and \bar{Q}_i are exactly orthogonal to each other (i.e. zero correlation), as L_i^c is proportional to $\partial\bar{Q}_i/\partial q$ in both layers (the maximum/minimum correlation coefficients computed using the time-lagged profiles and the corresponding lead/lag phases are shown in table 3.4). The inertial stress terms tend to enhance the mean cross-jet PV gradients resulting in the strengthening of the jets (see figure 3.4c,d). The maximum increase in the absolute PV values is associated with the maxima in the mean flow (a schematic is shown in figure 3.6). Also, in the equilibrium state, the domain integrated PV is conserved governed by the QG dynamics. Thus, in order to have both a local PV increase induced by the inertial stress terms and the global PV conservation, the jets drift southwards. The same applies to the case of a negative zonal slope, in which only the jet drift direction reverses. On the contrary, the absolute maxima in the cross-jet eddy forcing and mean PV profiles are almost aligned (table 3.5) and eddies have a very limited impact on the jet drift. Hence, the off-core linear forcing terms make the jets drift.

Boland et al. (2012) anticipate that the tilted jets drift meridionally to negate the effect of PV advection by the mean flow across PV isolines. The mechanism proposed in this thesis is in agreement with Boland et al. (2012) . It is evident from equations (3.5-3.6) that the inertial stress terms are associated with PV advection by the mean

Layer	Radiation stress term (L_i^c)			Inertial stress term (L_i^m)		
	Cor.	Min. lag-cor.	Lag (deg.)	Cor.	Max. lag-cor.	Lag (deg.)
Top ($i = 1$)	0	-0.91	84.4	0.13	0.97	78.8
Bottom ($i = 2$)	0	-0.97	90	0.58	0.97	56.3

Table 3.4: Correlation coefficients and the maximum/minimum lag-correlation coefficients between the time-mean cross-jet profiles of the linear stress terms and mean PV (\bar{Q}_i) for the medium-slope simulation. Here, a lag period of 180° is equal to the width (in q direction) of one jet pair.

Layer	Reynolds stress term (Rs_i)			Form stress term (Fs_i)		
	Cor.	Max. lag-cor.	Lag (deg.)	Cor.	Min. lag-cor.	Lag (deg.)
Top ($i = 1$)	0.26	0.29	16.9	-0.93	-0.96	11.3
Bottom ($i = 2$)	-0.01	0.08	-129	-0.89	-0.90	-11.3

Table 3.5: Correlation coefficients and the maximum/minimum lag-correlation coefficients between the time-mean cross-jet profiles of the nonlinear stress terms and mean PV (\bar{Q}_i) for the medium-slope simulation. Here, a lag period of 180° is equal to the width (in q direction) of one jet pair.

flow and the radiation stress terms, which capture the jet drift, compensate for this PV advection. Melnichenko et al. (2010) analysed the time-mean relative vorticity and PV balances to study the dynamics of drifting striations in the Pacific ocean using the output from an ocean general circulation model and altimetry dataset. They found the presence of linear advection terms in the time-averaged PV budget due to a nonzero angle between the large-scale flow and tilted striations, and they suspect that these linear advection terms could potentially induce jet drift. Note that, in our simulations, the eddy forcing and mean PV profiles also have a small offset (table 3.5), which could force the jets to move northwards, which is opposite to the observed drift direction. Indeed, eddies tend to slow the jets down (see table 3.1); however, it is not sufficient to stop the drift induced by the linear stress terms. On the other hand, eddies may have a significant impact on jet drift in the presence of steep topography and this has been seen in some studies (e.g. Thompson and Richards, 2011; Chen et al., 2015).

There are other mechanisms that can cause jet drift even in the absence of topography. For example, jets drift in systems forced with a meridionally non-uniform stress term, which results in meridionally asymmetric eddy momentum fluxes leading to jet drift in the meridional direction (Williams, 2003; Chan et al., 2007; Chemke and Kaspi, 2015b). It has been suggested that jets propagate in systems in which the reflectional (or mirror) symmetry is broken (Srinivasan, 2013). In general, idealised studies forced with either a uniform background vertical shear or an isotropic small-scale forcing generate stationary zonal jets, as the choices of the forcing terms preserve the mirror symmetry. Even in a barotropic model, an anisotropic forcing term can break this symmetry resulting in the formation of drifting jets (see chapter 3 in Srinivasan, 2013). In our work, the zonal topographic slope breaks this symmetry. However, the jets are tilted over topography, whereas

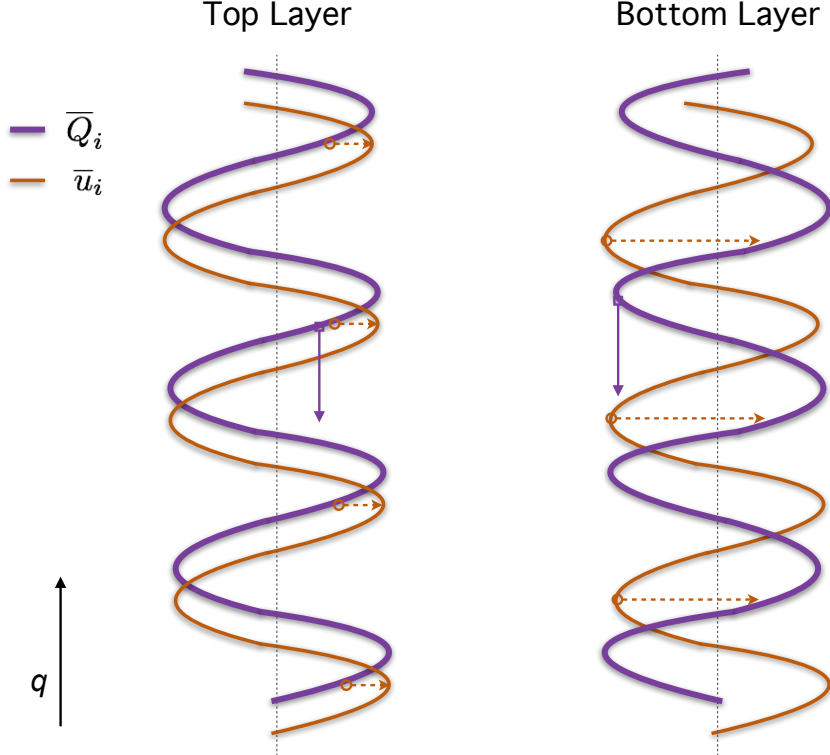


Figure 3.6: Adopted from Khatri and Berloff (2018a). Sketch of the cross-jet profiles of the mean PV (violet) and mean along-jet velocity (red). The profiles show the offset in the alignment observed in the numerical simulations (relative magnitudes are not to scale). The locations of the maximum increase/decrease in PV are indicated with red dashed arrows and the resulting direction of jet drift is shown with violet arrows. The zero lines are shown with black dotted lines.

the drifting jets can stay purely zonal in systems forced with an anisotropic forcing.

3.5 INTERPRETATION OF THE LINEAR FORCING

We observe that the inertial stress terms force the tilted jets and eddies remove energy from the jets. Here, the tilted jets and background shear are coupled via the sloped topography. The jets are able to gain energy directly from the imposed background shear and the forcing intensity depends on the mean flow strength. On the other hand, eddies gain energy from the jets as well as from the background shear. This is confirmed in chapter 4, where we analyse energetics of the tilted jets and eddies in the equilibrium state. This balance works only in continuously forced-dissipative systems as the flow dynamics would be very different in the absence of the background shear, which is the energy source for the jets. This aspect is addressed in detail in chapter 5.

3.6 ENERGY EQUILIBRATION AND THE LONG-TIME FLOW ADJUSTMENT

In addition to the jet tilt and drift, the energy of the system in the equilibrium state increases significantly with the zonal slope magnitude (figure 3.1i), even though the baroclinic growth rates are roughly the same. This happens because eddies grow by gaining energy from the background vertical shear through baroclinic instability as well as from the tilted jets. At the same time, the tilted jets are directly forced by the imposed shear and this energy gain is more for steeper zonal slopes. As a result, the system tends to be more energetic. It has been shown previously that eddies tend to be more energetic in systems in which the background shear has a nonzero meridional component and the rate of increase in the eddy energy is roughly proportional to the angle between the direction of the imposed shear and PV isolines (Arbic and Flierl, 2004b; Smith, 2007). In our study, PV isolines are tilted from the zonal direction due to the presence of the sloped topography and this introduces a nonzero angle between the vertical shear and background PV isolines. Thus, the energy of the system increases in the equilibrium state.

Another important observation we made is that, in the presence of topography, the system takes a long time to attain energy equilibrium. As seen in figure 3.1i, the total energy continuously increases in the interval 1,000-4,000 days, although the jets are formed by 1,000 days (figure 2.4). In order to investigate this matter, we first compare the energies of the barotropic and baroclinic flow components during this transient period (figure 3.7). It can be seen that both barotropic and baroclinic components grow at similar rates and the ratio of the barotropic kinetic energy to the total kinetic energy (barotropic + baroclinic, $E_{BT} + E_{BC}$) remains roughly constant during this time. Hence, this does not explain why energy of the system increases in the transient period.

Another possibility is that this slow energy increase is associated with the direct forcing, which is due to the imposed vertical shear, experienced by the jets. The inertial stress terms, which force the jets, are directly proportional to the mean along-jet velocity and this direct forcing becomes active only after the formation of the jets. Note that, initially, eddies grow via baroclinic instability and transfer energy upscale resulting in the formation of the jets. Later, however, the formed jets start gaining energy from the background flow through the inertial stress terms and eddies start acting against the jets. Given this, there should be a transition in the eddy behaviour from being jet-supporting to jet-opposing. In order to confirm the hypothesis, we computed correlation coefficients between the cross-jet profiles of the eddy forcing and PV in the time interval 500-4,000 days. As seen in figure 3.7c, the correlation coefficient in the top layer changes from a positive value to negative values with time. This shows that the form stress term becomes much stronger than the Reynolds stress term during this transient period and the overall impact of eddies is to weaken the jets. In the bottom layer, the correlation coefficient always remains negative because the Reynolds stress term in the lower layer is very weak

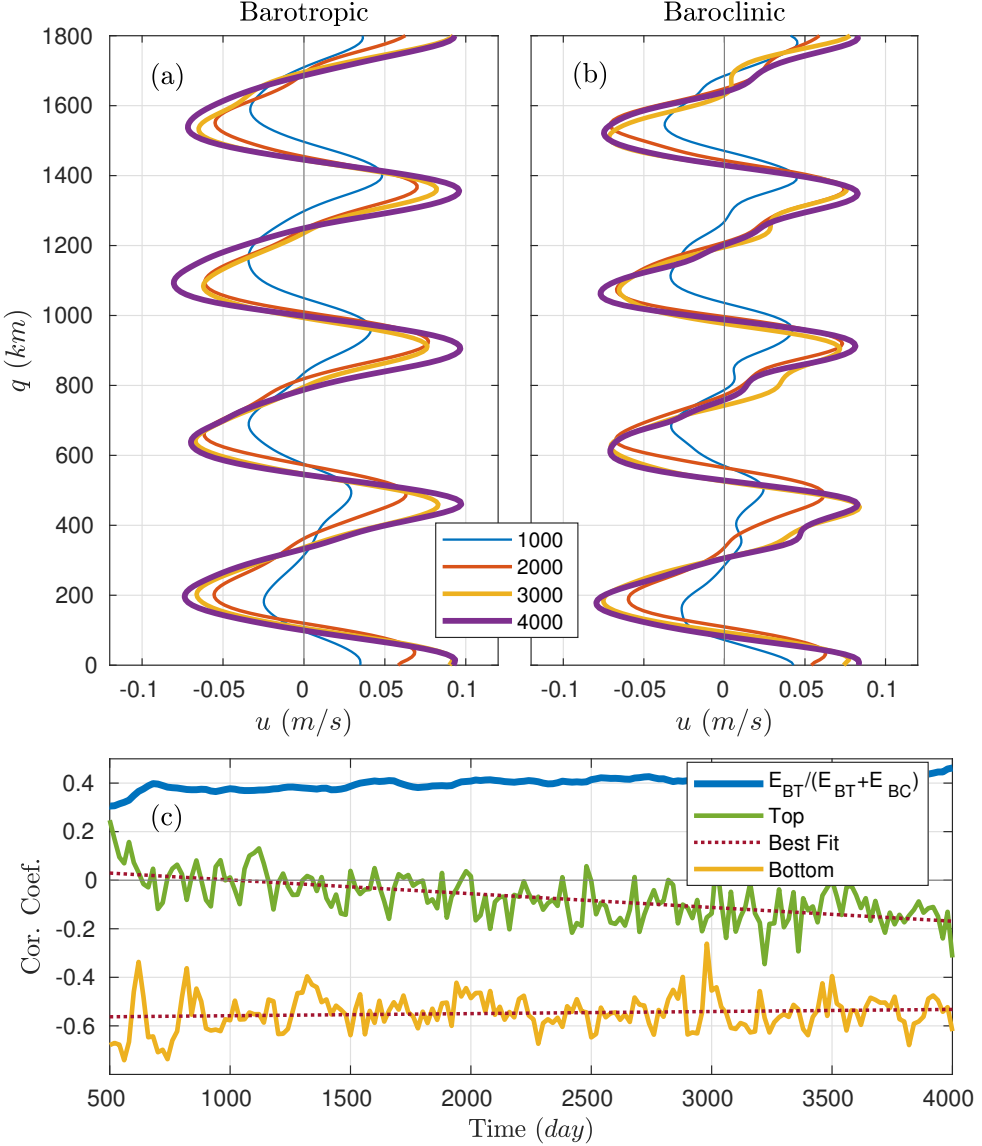


Figure 3.7: Adopted from Khatri and Berloff (2018a). Time evolution in the medium-slope simulation (a) Barotropic velocity $= \frac{1}{H_1+H_2}(H_1u_1 + H_2u_2)$, (b) Baroclinic velocity $= u_1 - u_2$ (cross-jet profiles, averaged in p direction, were aligned in the frame of reference propagating with the drifting jets; legend units are in days), and (c) Correlation coefficients computed between the eddy forcing and PV profiles, and the barotropic kinetic energy fraction. Note that we computed the eddy field using the full flow-field at every time step because we could not compute a mean flow in the transient state.

and the form stress term contributes the most to the eddy forcing term (also read the discussion of table 3.3). These results agree with our hypothesis and provide a reasonable explanation for the long-time energy adjustment.

3.7 SUMMARY

In this chapter, we studied the physical mechanism of jet drift over a zonally sloped topography in a two-layer QG model. We observe that jet drift is predicted by the linear dispersion relation and the drift speeds agree well with the phase speeds of linear Rossby

waves for gentle slopes. However, the deviations can be significant for steep slopes. We further analysed the PV budget in a frame of reference moving with the jets and it is found that linear stress terms, which we referred to as radiation stress and inertial stress terms, appear in the time-mean PV balances due to the presence of topography. The linear stress terms and eddy forcing largely balance each other. We also show that the radiation stress and inertial stress terms are much stronger than the nonlinear eddy forcing and the linear dynamics controls the jet drift. The jets drift meridionally to compensate for PV advection by the mean flow across PV isolines, which is in agreement with Boland et al. (2012). Also, we found that the tilted jets are coupled to the imposed shear and are able to gain energy directly from the background vertical shear. On the other hand, eddies act against the jets. This is because eddy buoyancy effects are significantly enhanced over topography and the form stress term tends to dominate over the Reynolds stress term in the top layer. As a result, the impact of eddies is the opposite to the case of eddy-driven stationary zonal jets (Rhines, 1975). The results suggest that, in the oceans, eddies can also act to weaken multiple jets in some regimes.

4

ENERGETICS OF TILTED JETS

As seen in the previous chapter, in the presence of the sloped topography, tilted jets are able to gain energy directly from the imposed vertical shear. Here, we use energy equations, which we derived from equation (3.3), for the mean flow and eddies to compute energy gain by the jets and eddies directly from the imposed vertical shear as a function of the slope magnitude. We further analyse the energy exchanges between the jets and eddies as well as energy loss due to viscous dissipation and bottom friction in the numerical simulations run with different magnitudes of the zonal slope. Also, the impacts of the slope magnitude on eddy potential vorticity (PV) and heat diffusivities are investigated.

4.1 ENERGY BUDGET ANALYSIS

We derived the energy equations for the mean flow, i.e. drifting jets, and eddies in the non-stationary frame of reference, which is described in chapter 3. In order to derive the mean flow and eddy energy budgets, we multiplied $\bar{\psi}_i$ (represents the time-mean flow) and ψ'_i (presents the transient eddy field), respectively, to the governing equation (3.3) and integrated over the whole domain. We further averaged the energy equations in time and the final equations are (refer appendix A.3 for the complete derivation):

$$\begin{aligned}
\int_A \frac{\partial}{\partial t} (\overline{KE}_m + \overline{PE}_m) &= \underbrace{- \int_A \sum_{i=1}^2 H_i \overline{\zeta_i \mathbf{u}_i} \cdot \nabla \overline{\psi_i}}_{T_v} - \underbrace{\int_A \sum_{i=1}^2 H_i \epsilon_i S_i \overline{(\psi_2 - \psi_1) \mathbf{u}_i} \cdot \nabla \overline{\psi_i}}_{T_b} \\
&+ \underbrace{\int_A H_1 S_1 U_b \left(\underbrace{\cos \theta \overline{\psi_1} \frac{\partial \overline{\psi_2}}{\partial p} - \sin \theta \overline{\psi_1} \frac{\partial \overline{\psi_2}}{\partial q}}_{\approx 0} \right)}_{E_m} \\
&- \underbrace{\int_A \nu \sum_{i=1}^2 H_i |\overline{\zeta_i}|^2}_{V_m} - \underbrace{\int_A \gamma H_2 |\nabla \overline{\psi_2}|^2}_{D_m}, \tag{4.1}
\end{aligned}$$

$$\begin{aligned}
\int_A \frac{\partial}{\partial t} (\overline{KE}_e + \overline{PE}_e) &= \underbrace{- \int_A \sum_{i=1}^2 H_i \overline{\zeta_i \mathbf{u}_i} \cdot \nabla \overline{\psi'_i}}_{-T_v} - \underbrace{\int_A \sum_{i=1}^2 H_i \epsilon_i S_i \overline{(\psi_2 - \psi_1) \mathbf{u}_i} \cdot \nabla \overline{\psi'_i}}_{-T_b} \\
&+ \underbrace{\int_A H_1 S_1 U_b \left(\cos \theta \overline{\psi'_1} \frac{\partial \overline{\psi'_2}}{\partial p} - \sin \theta \overline{\psi'_1} \frac{\partial \overline{\psi'_2}}{\partial q} \right)}_{E_e} \\
&- \underbrace{\int_A \nu \sum_{i=1}^2 H_i |\overline{\zeta'_i}|^2}_{V_e} - \underbrace{\int_A \gamma H_2 |\nabla \overline{\psi'_2}|^2}_{D_e}, \tag{4.2}
\end{aligned}$$

where

$$\left. \begin{aligned}
KE_m &= \sum_{i=1}^2 \frac{H_i}{2} |\nabla \overline{\psi_i}|^2, \\
PE_m &= \frac{H_1 S_1}{2} (\overline{\psi_1} - \overline{\psi_2})^2, \\
KE_e &= \sum_{i=1}^2 \frac{H_i}{2} |\nabla \overline{\psi'_i}|^2, \\
PE_e &= \frac{H_1 S_1}{2} (\overline{\psi'_1} - \overline{\psi'_2})^2.
\end{aligned} \right\} \tag{4.3}$$

Here, $i = 1$ ($i = 2$) denotes the top (bottom) layer and $\epsilon_1 = -\epsilon_2 = 1$. ψ_i is the layer-wise velocity streamfunction, $\mathbf{u}_i = (u_i, v_i)$ is the velocity and ζ_i is the relative vorticity. KE_m and KE_e represent the kinetic energy of the mean flow and eddies, respectively. PE_m and PE_e are the potential energy of the mean flow and eddies, respectively. The rest of the parameters are the same as defined in table 2.1. In the state of energy equilibrium, the time-derivatives of the sum of kinetic energy and potential energy for the mean flow and eddies in the above equations vanish. Hence, the energy gain by the jets and eddies,

denoted by E_m (note that $\cos \theta \bar{\psi}_1 (\partial \bar{\psi}_2 / \partial p) \approx 0$ because the mean flow is a function of q only) and E_e (conversion of the background available potential energy into eddy kinetic energy through baroclinic instability), from the imposed vertical shear is balanced by energy loss due to viscous dissipation (V_m, V_e) and bottom drag (D_m, D_e). Also, as seen in equations (4.1-4.2), the jets and eddies continuously exchange energy via exchanges of eddy momentum (T_v) and buoyancy (T_b). In our notation, T_v and T_b are positive if eddies lose energy to the jets. Note that, if eddies (the jets) gain energy due to eddy-jet interactions, then the jets (eddies) lose energy by the same amount. Thus, the first two terms on the right-hand-side in each of the equations (4.1-4.2) are of equal magnitudes and opposite signs (refer equation (A.26) for details). A schematic of all these processes is shown in figure 4.1. Additional terms, which can be represented in flux form, appear in the derivations of the energy equations. The integrals of those terms over the whole domain vanish as there is no flux input/output from the boundaries (see details in appendix A.3).

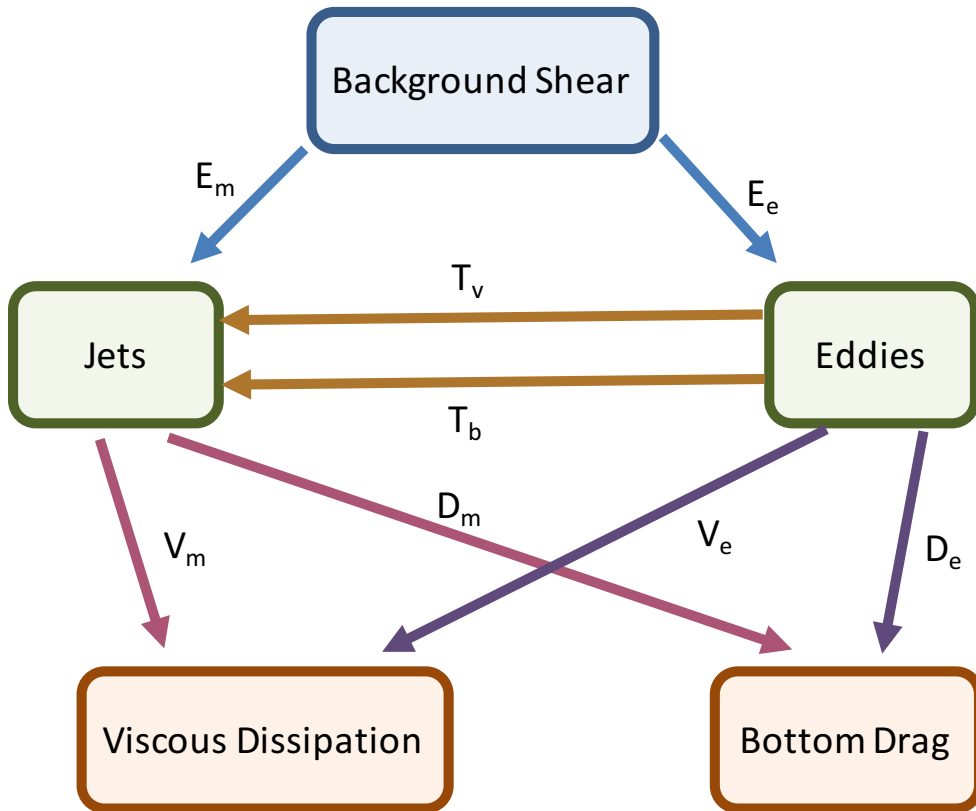


Figure 4.1: Schematic of energetics. E_m (E_e) represents the energy gain by jets (eddies) from the imposed vertical shear. T_v and T_b are energy exchanges between the jets and eddies through momentum and buoyancy exchanges. The rest of the terms represent the energy loss through viscous dissipation and bottom friction.

Similar to the approach adopted in chapter 3, we first interpolated the streamfunction field on the moving frame of reference for every snapshot in the energy equilibrium state and computed the time-mean flow (data in the time interval 10,000-20,000 days in the numerical simulations was used). We then subtracted the time-mean flow from the full field to compute the eddy field at different times. We computed the energy gain, energy exchange and energy loss terms for the numerical simulations run with different magnitudes of the zonal slope (table 4.1). In the case of purely zonal jets over a flat

bottom ($T_x = 0$), the energy gain by the jets from the imposed shear is negligible and almost all of the energy is gained by eddies from the background vertical shear. This makes sense because purely zonal jets cannot extract energy from the imposed vertical shear (see the expressions for E_m in equation (4.1)). The energy gain by the jets (E_m) increases with the magnitude of the slope because E_m is directly proportional to the tilt angle and the jet tilt angle increases with the slope magnitude. In fact, for steeper slopes, the energy gain by the jets from the imposed shear is more than the energy gain by eddies through baroclinic instability process. As a result, the system tends to be more energetic for steeper slopes, which we observe in the previous chapter. In a way, the direct energy transfer from the imposed shear to the jets is similar to the baroclinic instability process as the expressions for E_m and E_e are very similar. Hence, E_m represents the conversion of the background available potential energy into the mean kinetic energy of the large-scale flow.

T_x (m $^{-1}$ s $^{-1}$)	Energy gain		Jet-eddy exchange		Energy loss			
	E_m	E_e	T_v	T_b	V_m	D_m	V_e	D_e
0×10^{-12}	0.13	3.55	1.35	-0.29	-0.63	-0.46	-2.10	-0.49
0.55×10^{-12}	0.82	3.58	2.48	-1.16	-1.41	-0.80	-2.01	-0.42
0.83×10^{-12}	2.21	5.54	3.56	-2.52	-2.18	-1.28	-3.99	-1.04
1.4×10^{-12}	6.65	8.48	7.84	-8.35	-4.00	-3.52	-7.62	-2.07
1.9×10^{-12}	17.89	15.23	11.43	-18.85	-6.72	-6.27	-17.34	-7.49

Table 4.1: Energy gains, exchanges and losses by the mean flow and eddies (units are in 10^4 m 3 s $^{-3}$). E_m (E_e) represents the energy gain by the jets (eddies) from the imposed vertical shear. T_v and T_b are energy exchanges between the jets and eddies through momentum and buoyancy exchanges. The rest of the terms represent the energy loss through viscous dissipation and bottom friction. The terms were integrated over the whole domain and averaged over time (for the last 10,000 days in the simulations). The computations were performed in the frame of reference moving with the jets (see figure 3.3).

The rates of energy exchanges between the jets and eddies, which are denoted with T_v and T_b , are also affected because of the presence of topography. As discussed in chapter 3, eddies force the jets by transferring momentum to the jets and this results in positive values for T_v (see table 4.1). On the other hand, eddies remove energy from the jets through eddy buoyancy effects; hence, T_b is negative in all cases. The overall impact of eddies on the jets is determined by the sum of these two energy exchange terms. Over a flat bottom, eddies transfer energy to the jets on the net; thus, the jets are eddy-driven. This is in agreement with previous works on the formation of stationary zonal jets (e.g. Panetta, 1993; Lee, 1997; Thompson and Young, 2007). However, over a zonally sloped topography, the magnitudes of these exchange terms increase with the slope magnitude. We observe that the magnitude of T_b increases much faster than the magnitude of T_v and, in the numerical simulations run with relatively steeper slopes, the absolute value of T_b is more than the absolute value of T_v . Thus, in these cases, eddies remove energy from the jets on the net and act against the alternating jets. The same eddy behaviour is

seen when we look at correlation coefficients between the cross-jet profiles of eddy forcing and the mean PV as a function of the slope magnitude (see table 3.3). In the numerical simulations corresponding to steeper slopes, negative correlation coefficients between eddy forcing and the mean PV profiles show that eddies act against the jets. In this scenario, the jets are directly maintained by the imposed vertical shear and eddies play a secondary role. Eddies remove excess energy from the jets and help the system to attain an energy equilibrium state.

In the equilibrium state, the energy gain from the imposed shear is balanced by viscous dissipation and bottom friction terms. As the slope magnitude is increased, the rate of energy dissipation also increases to compensate against the increasing magnitudes of the energy gain terms and the total energy of the system is maintained in the equilibrium state. Note that, the absolute values of the energy gain terms and dissipation terms do not exactly balance each other in table 4.1. The deviations from zero are due to the interpolation scheme used in interpolating the streamfunction field on the moving frame of reference in the energy analysis. Nevertheless, the computational errors are small and do not affect the final conclusions.

4.2 HEAT AND PV DIFFUSIVITIES

In chapter 3, we compute heat diffusivity in the moving frame of reference and it is found that eddy buoyancy fluxes are down-gradient in the presence of the sloped topography. Since the strength of buoyancy fluxes increases significantly with the slope magnitude, it is helpful to analyse the impacts of topography on the magnitude of the heat diffusivity. In addition, we also compute PV diffusivity. These diffusivity coefficients are useful in quantifying the strength of eddy transport in the oceans. In general, eddy buoyancy and PV fluxes are down-gradient, and the diffusivity coefficients are positive at all locations along the cross-jet profile (e.g. see figure 3.5). Hence, we mainly focus on diffusivity coefficients averaged over the whole domain. We computed the mean heat and PV diffusivity coefficients using the following relations,

$$\begin{aligned} \mu_h &= \left\langle \frac{\epsilon_i S_i \overline{v'_i(\psi'_2 - \psi'_1)}}{-\partial_q(\epsilon_i S_i(\bar{\psi}_2 - \bar{\psi}_1) + \epsilon_i S_i U_b q \cos \theta)} \right\rangle = \left\langle \frac{\overline{v'_i(\psi'_2 - \psi'_1)}}{\bar{u}_2 - \bar{u}_1 - U_b \cos \theta} \right\rangle, \\ \mu_p &= \left\langle \frac{\overline{v'_i Q'_i}}{-\partial_q(\bar{Q}_i + (\beta + \epsilon_i S_i U_b)q \cos \theta)} \right\rangle = \left\langle \frac{\overline{v'_i \zeta'_i} + \epsilon_i S_i \overline{v'_i(\psi'_2 - \psi'_1)}}{-\partial_q \bar{\zeta}_i + \epsilon_i S_i (\bar{u}_2 - \bar{u}_1) - (\beta + \epsilon_i S_i U_b) \cos \theta} \right\rangle. \end{aligned} \quad (4.4)$$

Here, $i = 1$ ($i = 2$) denotes the top (bottom) layer, $\epsilon_1 = -\epsilon_2 = 1$ and $\langle \cdot \rangle$ represents the mean over the whole domain. ψ_i and $Q_i = \nabla^2 \psi_i + \epsilon_i S_i(\psi_2 - \psi_1)$ are the layer-wise

velocity streamfunction and PV anomaly, respectively. $\mathbf{u}_i = (u_i, v_i)$ and ζ_i are the velocity and relative vorticity, respectively, computed in the moving frame of reference. The rest of the parameters are the same as defined in table 2.1. Overbar represents the mean in the along-jet direction as well as over time, whereas primes represent the eddy field.

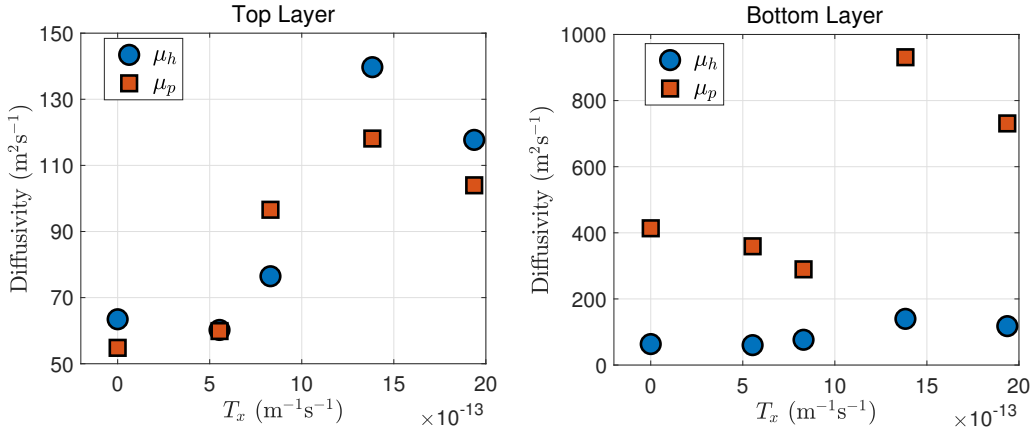


Figure 4.2: Domain-averaged heat and PV diffusivity coefficients as a function of T_x . The computations were performed over the last 10,000 days in the frame of reference moving with the jets (see figure 3.3).

The computed values of the heat and PV diffusivities are shown in figure 4.2. The values of the heat diffusivity in the upper and lower layers are the same because the layer-wise heat diffusivity relations in equation (4.4) are mathematically equivalent. Both the heat and PV diffusivities increase with the slope magnitude. One of the reasons for this increase is that the strength of eddy fluxes is enhanced over topography as eddies tend to be more energetic (eddies gain energy from the jets as well as from the imposed shear, see table 4.1). A similar increasing trend in the magnitudes of the diffusivity coefficients is expected over rough topography in the oceans (e.g. Tamsitt et al., 2017), although the absolute values may not match with our idealised simulations. Our results are in agreement with the works of Thompson (2010); Boland et al. (2012), who analysed transport properties in drifting jets over topography. These studies computed effective diffusivities in a stationary frame of reference; hence, their formulation included the effects of both the drifting jets and eddies. On the other hand, in our analysis, the diffusivity computations were performed in the moving frame of reference and only eddy fluxes were considered.

4.3 SUMMARY

In this chapter, we analysed the energy budgets of the drifting tilted jets and eddies in a non-stationary frame of reference moving with the jets. We show that the tilted jets are able to gain energy directly from the imposed eastward shear and the expression of this energy gain term resembles the term representing the conversion of the available potential energy to eddy kinetic energy through baroclinic instability process. However, in the case of tilted jets, this is the conversion of the available potential energy due to the imposed

shear directly to the mean kinetic energy of the large-scale flow. The rates of energy gain by the jets and eddies from the imposed shear increase with the topographic slope and the system stabilises at higher energy levels for steeper slopes. On the other hand, eddies play more of a secondary role and remove excess energy from the jets. In the presence of the sloped topography, eddy buoyancy fluxes are enhanced and, for sufficiently steep slopes, eddies remove more energy from the jets through eddy buoyancy effects than they transfer to the jets by transferring momentum into the jets. We also computed the heat and PV diffusivities as a function of the slope magnitude. We find that the diffusivity magnitudes are greater for steeper slopes. This indicates that rough topography may enhance eddy transport locally in the oceans.

5

EFFECTS OF VANISHING EDDY VISCOSITY

The contents of this chapter are derived from the manuscript titled “*Tilted, drifting jets over a zonally sloped topography: Effects of vanishing eddy viscosity*”, which has been accepted for publication in the *Journal of Fluid Mechanics*.

In the previous chapters, the dynamics of the jets were studied in continuously forced-dissipative systems, in which both the tilted jets and mesoscale eddies gain energy from the background vertical shear (Khatri and Berloff, 2018a). In the energy equilibrium state, this energy gain from the imposed vertical shear is balanced by energy loss through viscous dissipation and bottom friction. This suggests that reducing the dissipative parameters while keeping the strength of the background flow fixed may have a considerable impact on the dynamics, as the balance between the forcing and dissipation terms plays an important role in governing the large-scale dynamics. Also, the system dynamics in the case of freely evolving turbulence, in which the background flow is absent, is not understood. In ocean models, the primary role of eddy viscosity is to dissipate enstrophy at the grid scale; however, a considerable amount of energy is also dissipated at small-scales due to viscous effects and this affects the dynamics.

In this chapter, our focus is on investigating the impacts of dissipation strength on the drifting jets and studying the system dynamics in weak-dissipation flow regimes. Here, we study the jet dynamics in a number of simulations, which we ran with different magnitudes of dissipative parameters while keeping the strength of the imposed background shear fixed. In particular, we employed empirical orthogonal function (EOF) analysis to identify dominant flow patterns in the model solutions. As we will see in the next section, in addition to the tilted jets, other large-scale spatial patterns, which also propagate, are observed in the flow field. The presence of many large-scale patterns is in contrast to the case of zonal jet formation scenario, in which the flow field mainly consists

of zonal jets and mesoscale eddies. We further analyse the nonlinear interactions among these large-scale patterns and perform linear stability analysis to assess the impacts of dissipative parameters on the nonlinear interactions.

5.1 EOF ANALYSIS

In order to decompose the streamfunction field into a set of mutually orthogonal spatial patterns* and their principal components (PCs), we applied EOF analysis technique to the streamfunction field data of the last 10,000 days from the doubly-periodic simulations. We used the streamfunction field during the time period when the system was in an energy equilibrium state (see figure 3.1). The primary purpose of using EOF analysis is to identify the large-scale spatial patterns which contribute to the full flow field. Although individual EOFs do not correspond to the dynamical eigenmodes in the system, EOFs do provide some information about the presence of different energetic scales in the system. As seen in figure 5.1, the leading four EOFs capture two types of large-scale patterns. Note that consecutive EOFs appear in quadratures, as at least two EOFs are required to represent a propagating pattern. The first pair of EOFs captures the titled jets (will be referred to as J mode in the rest of the chapter) and the second pair of EOFs captures a purely zonal mode (will be referred to as Z mode in the rest of the chapter). In order to analyse the evolution of the J mode in time, we multiplied the first and second EOFs by their PCs and added them to reconstruct the J mode. Similarly, we used the second pair of EOFs and the corresponding PCs to reconstruct the Z mode. The power spectra of the PCs corresponding to these EOFs indicate that both the J and Z modes propagate with constant speeds corresponding to distinct frequency peaks in the power spectra (see bottom panels in figure 5.1). The Z mode moves northward, i.e. opposite to the J mode (see middle panels in figure 5.1). The Z mode moves much faster than the J mode. We also verified that the J and Z modes exist irrespective of the model configuration and boundary conditions (for J and Z modes in a channel simulation, see appendix B.2). However, for simplicity, we only focus on doubly-periodic simulations in the rest of the chapter.

We also noticed that the relative contributions of the J and Z modes to the flow field are highly dependent on the magnitude of the zonal slope (variances captured by the J and Z modes in different simulations are listed in table 5.1). The contribution of the

*We computed EOFs corresponding to the streamfunction field because streamfunction captures the large-scale flow structure much better than velocity and potential vorticity (PV) fields. In fact, we tried extracting large-scale modes by applying EOF analysis to the PV field; however, the leading EOFs mainly captured small-scale eddies, which contain most of the circulation in the system. Also, we used the streamfunction field in both layers together to compute EOFs having the full three-dimensional structure, i.e. variation in the zonal and meridional directions as well as in the individual layers. For the purpose of comparison, we also applied EOF analysis to the streamfunction field in the individual layers to compute EOFs in the upper and lower layers separately. The results did not show any considerable difference. The leading EOFs were the same, although variances captured by different EOFs were slightly different.

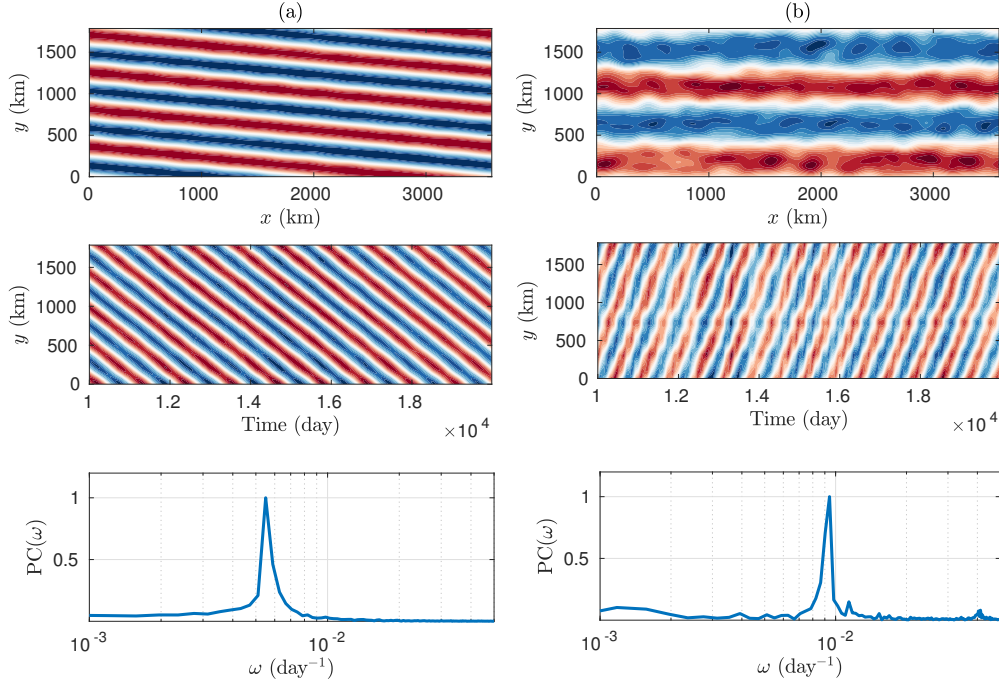


Figure 5.1: Leading EOFs of the streamfunction field in the simulation corresponding to figure 3.2 (data in the interval 10,000–20,000 days, i.e. 500 snapshots, was used for the EOF analysis); (a) EOF1, EOF2 (b) EOF3, EOF4. The spatial structure of the EOFs in the top layer is shown in the top panels, and Hovmöller diagrams of the J and Z modes reconstructed using EOFs and their PCs are shown in the middle panels (meridional cross-section of the modes at the centre of the domain is plotted against time). Colorbar range is [-1,1], blue to red. The power spectra of PCs (normalised to unity) corresponding to the EOFs are shown in the bottom panels. Note that the second and fourth EOFs are counterparts of the first and third EOFs, with the same spatial structure but with a phase shift of $\pi/2$. Here, one of the EOFs in a pair is shown. The J and Z modes together capture about 75% of the variance.

J (Z) mode to the flow field decreases (increases) with increasing the magnitude of the zonal slope. In fact, in the numerical simulation run with $T_x = 2.8 \times 10^{-12} \text{ m}^{-1}\text{s}^{-1}$, the variance captured by the Z mode is more than the variance of the J mode. Together, the J and Z modes capture most of the variance in all simulations. The propagation (drift) velocities of these modes are also shown in table 5.1, which were computed using equation (3.2). We compare the drift speeds of the modes with phase speeds of the linear Rossby waves obtained from the linear dispersion relation. In chapter 3, we show that the jet drift speeds agree well with the estimates from the linear dispersion relation. It is quite amazing that, in addition to the tilted J mode, the propagation speeds of the Z mode in the numerical simulations are also well predicted from the linear dispersion relation. This further strengthens the claim that the linear dynamics controls a major part of the flow dynamics.

As shown in chapter 3, tilted jets drift to compensate for the potential vorticity (PV) advection by the mean flow across PV isolines (Boland et al., 2012; Khatri and Berloff, 2018a) and the same physical mechanism can be used to understand the propagation of the Z mode. The J mode advects PV across PV isolines in both layers, as the J mode tends to be aligned with the mean barotropic PV isolines (Boland et al., 2012). On the

$T_x \times 10^{12}$ (m $^{-1}$ s $^{-1}$)	Var. (%)		Velocity NS (cm s $^{-1}$)		Velocity DR (cm s $^{-1}$)		n_y	f_{BT}	
	J	Z	J	Z	J	Z			
1.4	66.8	9.2	$-0.05\hat{i} - 0.46\hat{j}$	$1.56\hat{j}$	$-0.07\hat{i} - 0.53\hat{j}$	$2.15\hat{j}$	4	2	0.45
2.1	26.6	16.4	$-0.04\hat{i} - 0.31\hat{j}$	$12.58\hat{j}$	$-0.04\hat{i} - 0.34\hat{j}$	$12.80\hat{j}$	4	1	0.56
2.8	8.3	66.8	$-0.13\hat{i} - 0.81\hat{j}$	$17.26\hat{j}$	$-0.18\hat{i} - 1.06\hat{j}$	$17.07\hat{j}$	3	1	0.72

Table 5.1: Variances and drift velocities, obtained from the numerical simulations (NS) as well as using the linear dispersion relation (DR), of the J and Z modes as a function of the slope magnitude. The rest of the parameters were kept the same in the simulations, see table 2.1. \hat{i} and \hat{j} are the zonal and meridional unit vectors, respectively. n_y is equal to the number of meridional wavelengths of a mode that is equal to the meridional width of the domain. In all simulations, the zonal wavelength of the J modes is equal to the zonal extent of the domain. $f_{BT} = \bar{E}_{BT}/(\bar{E}_{BT} + \bar{E}_{BC})$ is the mean barotropic KE fraction, where $E_{BT} = 1/2 \int_A |\mathbf{u}_{BT}|^2$ and $E_{BC} = 1/2 \int_A |\mathbf{u}_{BC}|^2$ are the barotropic and baroclinic KE, respectively, integrated over the whole domain.

other hand, the purely zonal Z mode advects PV across PV isolines in the lower layer only. The J and Z modes propagate in nearly opposite directions. It is possible that the J and Z modes propagate in opposite directions because, on average, these modes advect PV in opposite directions across PV isolines. For example, if the J mode advects PV from a high PV region to a low PV region, then the Z mode advects PV from a low PV region to a high PV region. As a consequence, the J and Z modes tend to propagate in opposite directions. It is important to note here that the J and Z modes correspond to the leading tilted and purely zonal patterns observed in the EOF analysis. These modes need not be present at the same wavenumber across all simulations. For example, the meridional wavelengths of these modes are longer in the simulations run with steeper slopes (see table 5.1). This is also one of the reasons for the differences in their propagation speeds, i.e. modes with longer meridional wavelengths propagate faster.

We also look the impacts of the J and Z modes on the vertical flow structure. In particular, we computed the ratio of kinetic energy (KE) of the barotropic velocity component, $\mathbf{u}_{BT} = (H_1 \mathbf{u}_1 + H_2 \mathbf{u}_2)/(H_1 + H_2)$, to the sum of the mean KE of the barotropic and baroclinic velocity, $\mathbf{u}_{BC} = \mathbf{u}_1 - \mathbf{u}_2$, components in the full flow field. As shown in table 5.1, the energy fraction increases as the slope magnitude is increased in the numerical simulation. This suggests that the flow field tends to be more barotropic in the presence of the Z mode, as the energy fraction of the barotropic flow increases with an increase in the variance captured by the Z mode. It is quite likely that the barotropic flow component becomes stronger to dissipate more energy through bottom friction, as the system tends to be more energetic over steeper slopes (see table 4.1). We further discuss this aspect later in this chapter.

In addition to the J and Z modes, many other large-scale modes are captured by higher EOFs. All of these modes differ in their spatial structure, and these modes also have different tilt angles and propagation speeds (first twenty EOFs are shown in figure B.3). Many of these EOFs are comparable to the J and Z modes in size and are also much

larger than the size of mesoscale eddies. As it was discussed in chapter 3, the tilted jets tend to align with the tilted barotropic PV isolines. It is possible that, in a similar manner, these large-scale EOFs also tend to align with PV fields in one of the layers or a linear combination of layer-wise PV fields. However, the imposed periodic boundary conditions in the simulations greatly affect these large-scale modes as the boundary conditions restrict the EOFs to have only certain tilt angles. All these EOFs, which capture different large-scale modes, can be broadly categorised into two families: the first family contains tilted EOFs (J family) and the second family contains purely zonal EOFs (Z family). The aim of this study is to understand why many tilted and zonal large-scale modes, irrespective of what their meridional width and drift speeds are, coexist. We do not study specific EOFs in the system, as these EOFs need not be unique in different scenarios. Also, the relative contributions of EOFs vary across different simulations.

The presence of various large-scale modes makes the dynamics more complex than in the system of zonal jets formed over a flat bottom, where the large-scale flow mainly consists of stationary zonal jets and the rest of the flow field is dominated by mesoscale eddies. The stationary zonal jets gain energy from mesoscale eddies, which grow through baroclinic instability. In contrast, in our study, the flow field tends to be more complicated as the flow field consists of multiple propagating large-scale modes (see appendix B.3). This suggests that the upscale transfer of energy from mesoscale eddies need not lead to the formation of only one type of alternating jets, rather many alternating patterns can coexist. Also, in the presence of topography, the energy transfer rates across different spatial scales are affected because of the coupling between the background flow and tilted large-scale modes (see chapters 3,4). Many works have studied the spatial and temporal variability in multiple jets in the oceans (e.g. Thompson, 2010; Thompson and Richards, 2011; Stern et al., 2015; Rudko et al., 2018). However, little success has been achieved in isolating different large-scale alternating patterns constituting the flow field. Berloff et al. (2009a,b) propose that stationary zonal jets over a flat bottom can originate due to the presence of several phase-locked stationary zonal eigenmodes, which are solutions of the linearised governing equations. This means that multiple stable equilibria with a different number of jet pairs are feasible and the zonal jets correspond to one of the equilibrium solutions. Similarly, it is possible that the large-scale modes observed in the EOF analysis correspond to multiple stable eigenmodes comprising of both zonal and tilted modes that exist over a sloped topography. The main difference is that, over a sloped topography, even zonal eigenmodes are not stationary and propagate with constant speeds. These tilted and zonal eigenmodes can also interact nonlinearly and exchange energy, which is discussed in the next section.

5.2 EFFECTS OF EDDY VISCOSITY AND BOTTOM FRICTION

A number of numerical simulations were run in which the magnitudes of the dissipative parameters were varied while keeping the values of other parameters fixed (see table 2.1). It is observed that variances captured by the J and Z modes are strongly affected by the eddy viscosity (ν) and bottom friction (γ) parameter values. The variances captured by the J and Z modes and their propagation velocities in different simulations are shown in tables 5.2, 5.3. The variance captured by the Z mode increases as either eddy viscosity or bottom friction is decreased (vice versa is true for the J mode). In fact, the Z mode is not even observed in the flow field if the values of the dissipative parameters are beyond some critical values. These critical values are not unique and depend on boundary conditions and problem parameters. On the other hand, the propagation speeds of the J and Z modes do not show a considerable change in different simulations. The J and Z modes move meridionally in opposite directions, and the Z mode propagates approximately three times faster than the J mode. However, in the case of $\nu = 50 \text{ m}^2\text{s}^{-1}$, the Z mode is almost twenty times faster than the J mode (see table 5.2). In this case, the meridional wavelength of the Z mode is equal to the meridional width of the domain and the Z mode has only one pair of jets (figure not shown) as opposed to two pairs in other cases. Since the meridional wavelength of the Z mode is longer in the $\nu = 50 \text{ m}^2\text{s}^{-1}$ case in comparison to other cases, the Z mode tends to propagate faster. We further discuss this aspect in the next section. The presence of a wider Z mode indicates the upscale transfer of energy to very low meridional wavenumbers. One possibility is that the system tends to stabilise at higher energy levels due to weaker dissipation; hence, a wider Z mode can be formed. As discussed in the previous section, the EOFs need not be exactly the same in different flow regimes. Hence, the primary focus in this study is on the two general types of modes, i.e. tilted and purely zonal.

Although the propagation speeds of the J and Z modes do not vary significantly across different simulations, the J mode seems to feel some impact due to the presence of the Z mode, as the J mode propagates slower in the numerical solutions in which the flow field has a relatively higher contribution from the Z mode (see table 5.2). The differences in the propagation speeds of the J mode are quite small across different simulations; however, the differences are not explained by the linear dispersion relation. The linear dispersion relation shows negligible changes in the propagation speeds for different magnitudes of the eddy viscosity and bottom friction parameters (not shown). It is most likely that these differences are due to nonlinear effects. In addition, the fraction of the mean barotropic KE increases as the contribution of the Z mode increases (see also the discussion of table 5.1). The barotropic component of the flow is expected to become stronger with a reduction in the magnitude of the bottom friction parameter (Arbic and Flierl, 2004a). However, it is not clear how the presence of the zonal mode is linked to the vertical flow structure.

ν (m^2s^{-1})	Variance (%)		Velocity (cm s^{-1})		f_{BT}
	J	Z	J	Z	
200	80.6	0	$-0.06\hat{i} - 0.48\hat{j}$	-	0.30
150	81.6	0	$-0.06\hat{i} - 0.48\hat{j}$	-	0.33
100	66.8	9.2	$-0.06\hat{i} - 0.46\hat{j}$	$1.56\hat{j}$	0.45
75	53.0	15.1	$-0.05\hat{i} - 0.41\hat{j}$	$1.48\hat{j}$	0.49
50	26.6	12.4	$-0.05\hat{i} - 0.38\hat{j}$	$8.58\hat{j}$	0.59

Table 5.2: Variances and propagation velocities of the J and Z modes for different values of eddy viscosity (ν) in simulations run with $T_x = 1.4 \times 10^{-12} \text{ m}^{-1}\text{s}^{-1}$ and $\gamma = 2 \times 10^{-8} \text{ s}^{-1}$. The rest of the parameters were kept the same in the simulations (see table 2.1). \hat{i} and \hat{j} are the zonal and meridional unit vectors, respectively. $f_{BT} = \bar{E}_{BT}/(\bar{E}_{BT} + \bar{E}_{BC})$ is the the mean barotropic KE fraction, where $E_{BT} = 1/2 \int_A |\mathbf{u}_{BT}|^2$ and $E_{BC} = 1/2 \int_A |\mathbf{u}_{BC}|^2$ are the barotropic and baroclinic KE, respectively, integrated over the whole domain.

γ (s^{-1})	Variance (%)		Velocity (cm s^{-1})		f_{BT}
	J	Z	J	Z	
4×10^{-8}	80.2	0	$-0.06\hat{i} - 0.46\hat{j}$	-	0.38
2×10^{-8}	66.8	9.2	$-0.06\hat{i} - 0.46\hat{j}$	$1.56\hat{j}$	0.45
10^{-8}	47.6	25.2	$-0.05\hat{j} - 0.42\hat{j}$	$1.56\hat{j}$	0.47

Table 5.3: Variances and propagation velocities of the J and Z modes for different values of bottom friction (γ) in simulations run with $T_x = 1.4 \times 10^{-12} \text{ m}^{-1}\text{s}^{-1}$ and $\nu = 100 \text{ m}^2 \text{s}^{-1}$. The rest of the parameters were kept the same in the simulations (see table 2.1). \hat{i} and \hat{j} are the zonal and meridional unit vectors, respectively. $f_{BT} = \bar{E}_{BT}/(\bar{E}_{BT} + \bar{E}_{BC})$ is the the mean barotropic KE fraction, where $E_{BT} = 1/2 \int_A |\mathbf{u}_{BT}|^2$ and $E_{BC} = 1/2 \int_A |\mathbf{u}_{BC}|^2$ are the barotropic and baroclinic KE, respectively, integrated over the whole domain.

In order to understand the impacts of eddy viscosity on the dynamics and investigate why the contribution of the Z mode in the flow field tends to be enhanced in weak dissipation flow regimes, we first analyse the two-dimensional KE spectrum (figure 5.2). We compare the KE spectra computed using the flow fields in $\nu = 200$ and $50 \text{ m}^2\text{s}^{-1}$ cases. Since the Z mode is only observed in the latter case (see table 5.2), we can analyse the differences in the KE spectra. From a visual inspection of figure 5.2, it is quite evident that the Z mode possesses a significant amount of energy in the bottom layer in the lower eddy viscosity case. This indicates that the vertical flow structure tends to be more barotropic in the presence of the Z mode. This also agrees with the observations from the EOF analysis (tables 5.1-5.3). Another important aspect to note is that many different spatial scales seem to be active in the lower eddy viscosity case (especially in the bottom layer in figure 5.2). The KE spectra show that, in the lower eddy viscosity case, additional Fourier modes possess significantly more energy than in the higher eddy viscosity case (compare top and bottom panels in figure 5.2). These additional Fourier modes are present at relatively smaller spatial scales (or larger wavenumbers) than the J and Z modes. It is possible that these additional energetic Fourier modes are able to exchange energy with the J and Z modes. We hypothesise that these small-scales interact

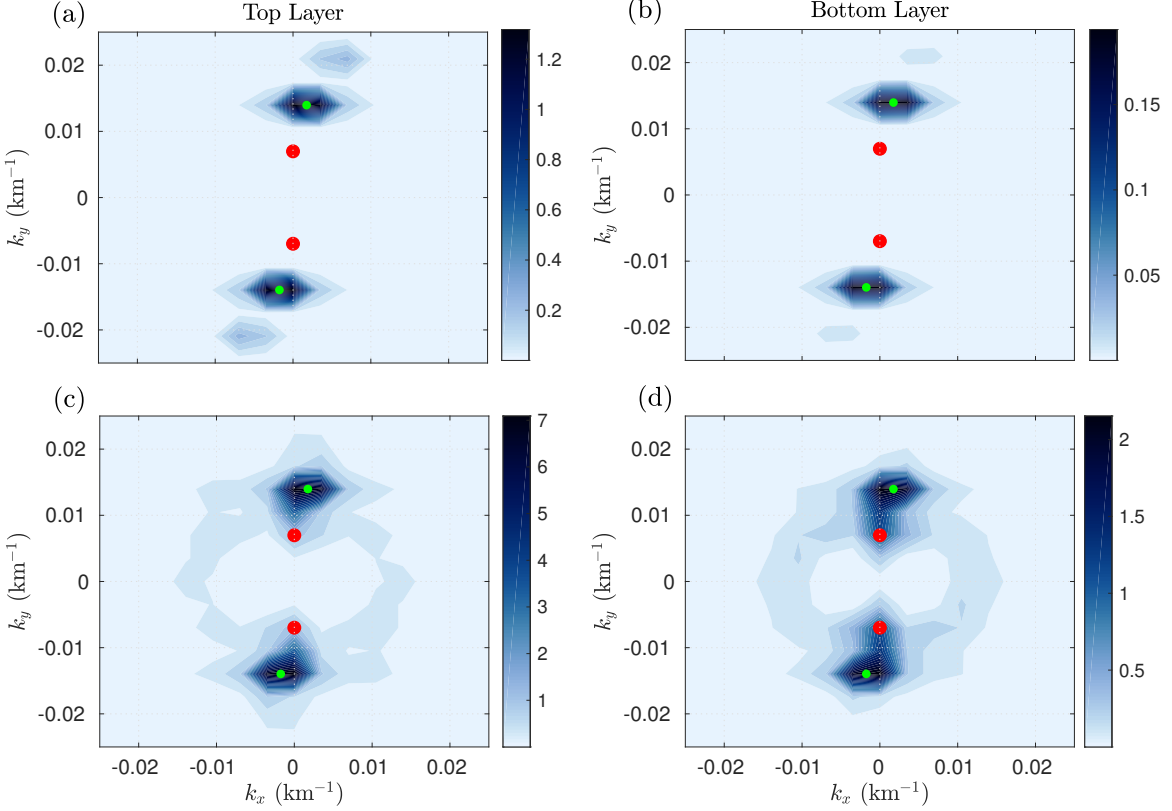


Figure 5.2: KE spectrum (units are in cm^2s^{-2}) averaged over 2,000 days (100 snapshots between 18,000–20,000 days); (a,b) $\nu = 200 \text{ m}^2\text{s}^{-1}$ and (c,d) $\nu = 50 \text{ m}^2\text{s}^{-1}$. The zonal and meridional wavenumbers are denoted by (k_x, k_y) . Green and red dots represent the wavenumbers corresponding to the J and Z modes, respectively. In the lower eddy viscosity case, the J and Z modes seem to interact nonlinearly and possibly exchange energy.

with the J mode, which is directly forced by the imposed background shear (Khatri and Berloff, 2018a), and feed energy to the Z mode in the lower eddy viscosity case.

In order to confirm the hypothesis, a test numerical simulation was run in which the background flow, eddy viscosity and bottom friction parameters were set to zero. The model was initialised using the reference solution from the $\nu = 200 \text{ m}^2\text{s}^{-1}$ case and the simulation was run for 10,000 days. The evolution of the KE spectrum is shown in figure 5.3 and it can be clearly seen that many additional Fourier modes become more energetic. Since the background flow is absent, these additional Fourier modes must have received energy from the J mode through nonlinear interactions, as the J mode initially contained most of the energy in the system. The system quickly attains an equilibrium state, in which the Z mode contains most of the energy in the system and the J mode almost disappears. This shows that these additional energetic Fourier modes efficiently interact with the J and Z modes. As a result, mesoscale eddies are able to transfer energy to meridional scales even larger than the meridional width of the J mode. In the case of zonal jets over a flat bottom, the meridional width of the jets (known as the Rhines scale) is generally set by available eddy energy and Rossby waves in the system (Rhines, 1975). In other words, the upscale energy transfer from eddies is halted at the scale equal to

the meridional wavelength of the jets. However, the results in this study indicate that, in the presence of topography, the meridional width of an alternating jet pattern need not be bounded by the Rhines scale. Over topography, it may be possible to excite very low meridional wavenumbers through interactions among various large-scale modes. It is intriguing that the system evolves to purely zonal structures in the case of freely evolving turbulence. It is not yet clear why only zonal patterns emerge and this needs to be further investigated.

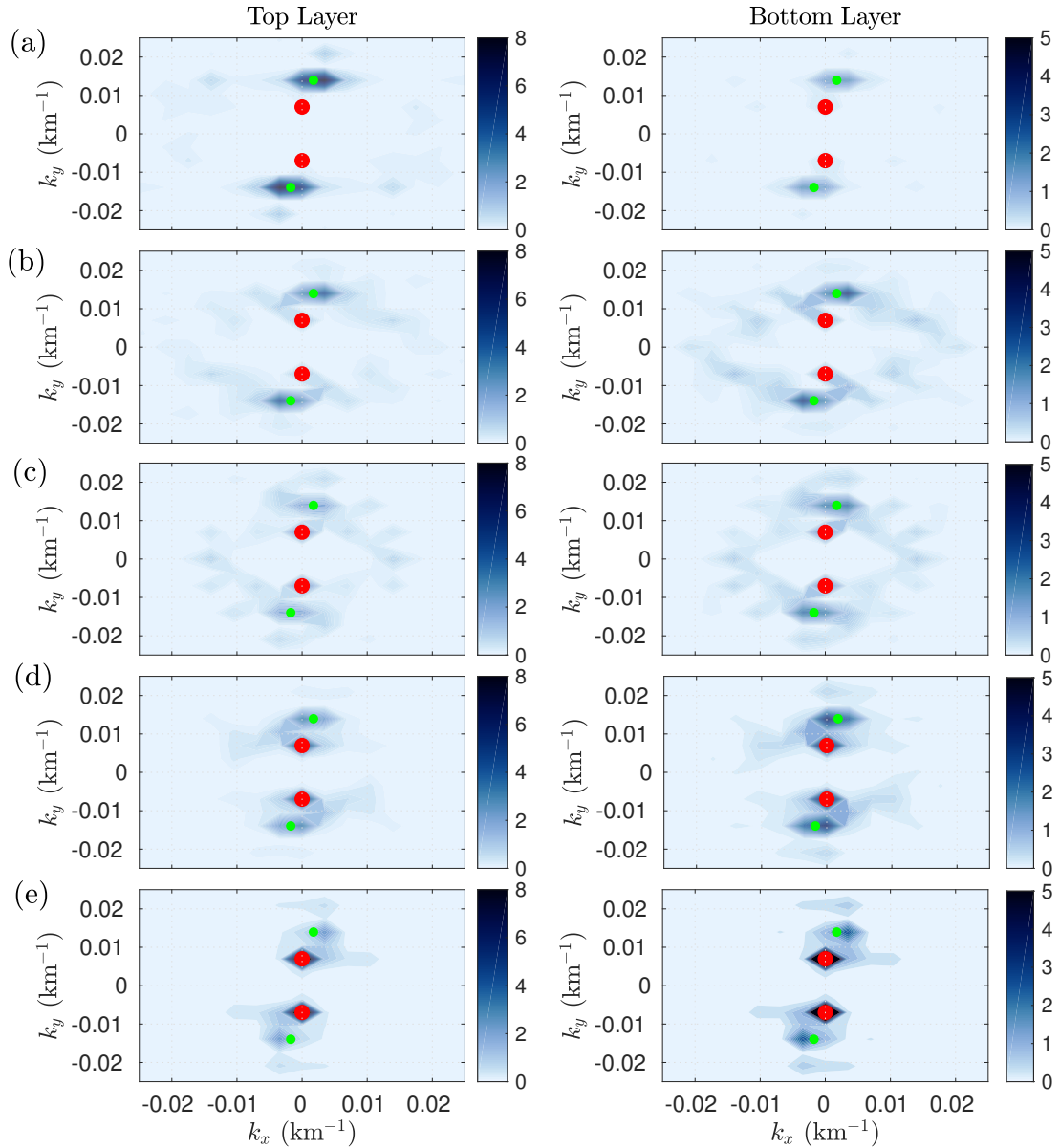


Figure 5.3: Time evolution of the KE spectrum (snapshots, units are in cm^2s^{-2}) in the simulation in which the background flow, eddy viscosity and bottom friction parameters were set to zero (a-e): KE spectra at 200, 400, 500, 600 and 800 days, respectively. The zonal and meridional wavenumbers are denoted by (k_x, k_y) . Green and red dots represent the wavenumbers corresponding to the J and Z modes, respectively.

Many studies have shown that eddy viscosity has an important role in ocean models (Jochum et al., 2008; Arbic et al., 2013). The geostrophic turbulence theory predicts

that most of the KE (enstrophy) flows upscale (downscale) from the energy injection scale, which generally corresponds to the scale of baroclinic instability in the system (Rhines, 1979). In the energy equilibrium state, most of the energy and enstrophy are dissipated through bottom friction and viscous dissipation, respectively. Thus, in ocean models, the viscous term is required to dissipate enstrophy at the grid scale. However, eddy viscosity also dissipates energy at small scales and this is not accounted for in the geostrophic turbulence theory (Rhines, 1979). This effectively damps out the small-scale eddy activity and suppresses the upscale energy transfer by eddies. The results in this work show that, for sufficiently small values of the eddy viscosity parameter, tilted jets formed over topography by the action of mesoscale eddies can become unstable and feed energy to even larger flow structures. The investigation into this upscale energy transfer to meridional scales larger than the Rhines scale has received little attention. In section 5.4, we use linear stability analysis to study these effects.

5.3 WAVE SOLUTIONS FOR THE Z MODES

As seen in the previous section, the propagation velocities of the Z modes agree well with the estimates from the linear dispersion relation. Also, the contribution of the Z mode in the full flow field increases with decreasing the values of the dissipative parameters (see tables 5.2,5.3). In fact, the flow field is dominated by purely zonal modes in the case of freely evolving turbulence (figure 5.3). Here, we derive a simplified expression for the propagation velocity of the Z modes using the linear dispersion relation. Since the contribution from purely zonal modes is at maximum in the absence of forcing and dissipative terms, we set $U_b = \nu = \gamma = 0$ in equation (2.3) to obtain an approximate dispersion relation (for a purely zonal mode, $k_x = 0$)

$$\begin{bmatrix} \omega(k_y^2 + S_1) & -S_1\omega \\ -S_2\omega & \omega(k_y^2 + S_2) - k_y T_x \end{bmatrix} \begin{bmatrix} \widetilde{\psi}_1 \\ \widetilde{\psi}_2 \end{bmatrix} \approx 0. \quad (5.1)$$

In order to derive an expression for the meridional phase speed for the Z modes, we substitute $\omega = c_w k_y$, where c_w is the phase speed of the wave, and solve the above matrix for nontrivial solutions (only the nonzero solutions for c_w are considered),

$$c_w^2 k_y^2 [(k_y^2 + S_1)(k_y^2 + S_2) - S_1 S_2] - c_w k_y^2 T_x (k_y^2 + S_1) \approx 0, \quad (5.2)$$

$$c_w \approx \frac{T_x (k_y^2 + S_1)}{k_y^2 (k_y^2 + S_1 + S_2)}. \quad (5.3)$$

The meridional velocity of a zonal mode increases linearly with the slope magnitude and decreases roughly as $1/k_y^2$ (for $k_y^2 \ll S_1 + S_2$ or $k_y^2 \gg S_1 + S_2$). This relationship

agrees well with the propagation speeds of the Z modes estimated from the nonlinear numerical simulations (see table 5.1). For example, the ratio of the propagation speeds of the Z mode in $T_x = 2.1 \times 10^{-12}$ and $T_x = 2.8 \times 10^{-12} \text{ m}^{-1}\text{s}^{-1}$ cases is 0.73, which matches the ratio of the slope magnitudes in the two cases. Similarly, in $\nu = 100$ and $\nu = 50 \text{ m}^2\text{s}^{-1}$ cases in table 5.2, the ratio of the propagation speeds of the Z mode is about one fifth and the ratio of the squares of the meridional wavenumbers corresponding to the Z mode is four. Thus, the simple expression predicts the propagation speeds of the Z mode reasonably well.

5.4 LINEAR STABILITY ANALYSIS

As shown in section 5.2, in weak dissipation regimes, many energetic Fourier modes appear at relatively smaller scales than the J and Z modes, and this results in an increase in the energy exchange among different Fourier modes through nonlinear interactions. In order to understand the effects of the dissipative parameters on the stability of these additional Fourier modes, we perform linear stability analysis around the time-mean propagating state of the tilted jets, which correspond to the J mode in our study. Similar to the technique used in chapter 3, we use a propagating frame of reference such that the jets are exactly zonal and stationary in it (see figure 3.3). The governing equation (3.3) was linearised around the time-mean tilted jets. The streamfunction field was then represented as a sum of the mean and perturbation terms, $\psi_i(p, q, t) = \bar{\psi}_i(q) + \psi'_i(p, q, t)$, and the nonlinear terms in perturbations were neglected. The final equations in terms of ψ'_i are (see the full derivation in appendix A.4):

$$\frac{\partial}{\partial t} [\nabla^2 \psi'_i + \epsilon_i S_i (\psi'_2 - \psi'_1)] + \left[A_i \frac{\partial}{\partial p} + B_i \frac{\partial}{\partial q} \right] [\nabla^2 \psi'_i + \epsilon_i S_i (\psi'_2 - \psi'_1)] + C_i \frac{\partial \psi'_i}{\partial p} + D_i \frac{\partial \psi'_i}{\partial q} = \nu \nabla^4 \psi'_i - \delta_{i2} \gamma \nabla^2 \psi'_i, \quad (5.4)$$

where

$$\left. \begin{aligned} A_1 &= U_b \cos \theta + \bar{u}_1, \\ A_2 &= \bar{u}_2, \\ B_1 &= -c - U_b \sin \theta, \\ B_2 &= -c, \\ C_1 &= (\beta + S_1 U_b) \cos \theta - \bar{u}_1'' + S_1 (\bar{u}_1 - \bar{u}_2), \\ C_2 &= (\beta - S_2 U_b) \cos \theta - T_x \sin \theta - \bar{u}_2'' + S_2 (\bar{u}_2 - \bar{u}_1), \\ D_1 &= -(\beta + S_1 U_b) \sin \theta, \\ D_2 &= -(\beta - S_2 U_b) \sin \theta - T_x \cos \theta. \end{aligned} \right\} \quad (5.5)$$

Here, $i = 1$ ($i = 2$) denotes that top (bottom) layer, δ_{ij} is the Kronecker delta and $\epsilon_1 = -\epsilon_2 = 1$. The tilt angle, θ , and drift speed of the frame of reference, c , are equal to the tilt angle and drift speed of the J mode, which were estimated using the EOF

analysis. $\bar{u}_i = -\partial\bar{\psi}_i/\partial q$ and \bar{u}_i'' are the mean flow (averaged in p direction) and its double derivative in q direction (shown in figure 5.4), respectively. The streamfunction data for the last 10,000 days in the simulation corresponding to figure 5.1 was used to compute the time-mean streamfunction field in the moving frame of reference and the time-mean streamfunction field was further averaged along direction p . The cross-jet profile of the time-mean streamfunction field was then used to generate the cross-jet profiles of \bar{u}_i and \bar{u}_i'' .

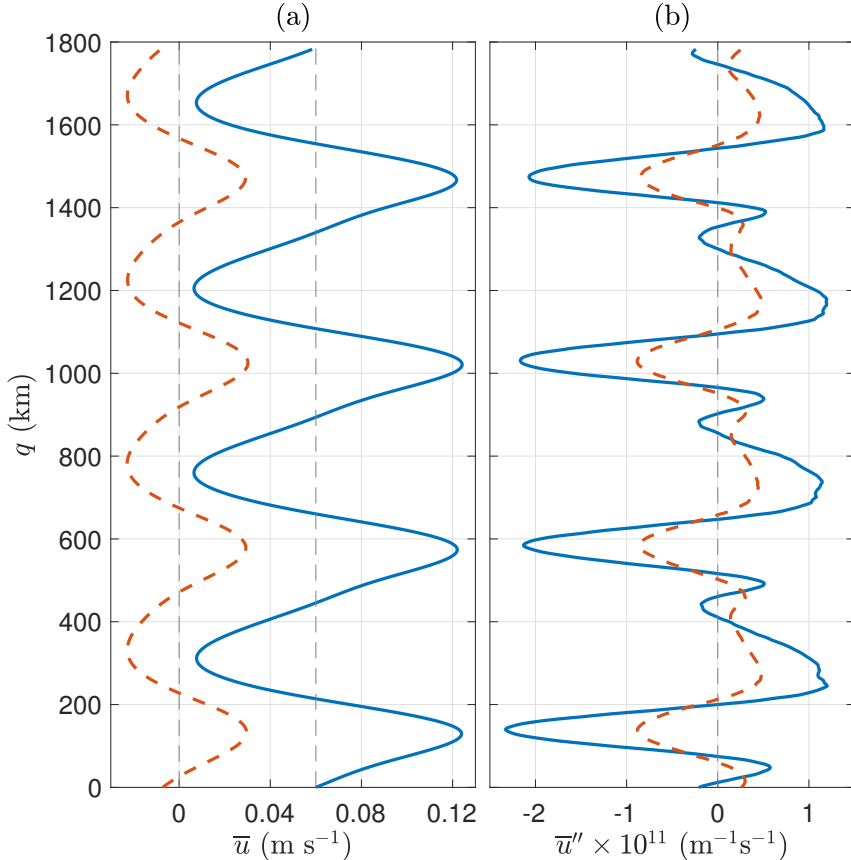


Figure 5.4: Profiles of \bar{u}_i and \bar{u}_i'' used in the stability analysis. The profiles were computed by applying spatial and time averaging in the direction along the jets in the moving frame of reference between 10,000-20,000 days for the simulation corresponding to figure 5.1 (blue solid line in the top layer and red dotted line in the bottom layer). The velocity profile in the top layer is shown relative to the imposed background flow of 0.06 m s^{-1} .

The system of equations (5.4) can be solved as the coefficients A_i , B_i , C_i and D_i are known, and the only unknown parameters are ψ'_1 and ψ'_2 . We used Fourier decomposition in p direction, i.e. along the jets, and finite-difference discretisation with 512 grid points in q direction. We assumed solutions of the kind $\psi'_i = \tilde{\psi}_i(q)e^{j(lp-\omega t)}$ for the perturbation terms. l is the wavenumber in p direction and periodic boundary conditions were used at the endpoints in q direction. This substitution results in an eigenvalue problem. The eigenvalue problem was solved for each wavenumber l separately and the analysis was repeated for different magnitudes of the eddy viscosity and bottom friction parameters for the same time-mean cross-jet flow profiles (details are in appendix A.4). This is similar

to the method used in Berloff et al. (2011); Berloff and Kamenkovich (2013a), but in the presence of topography.

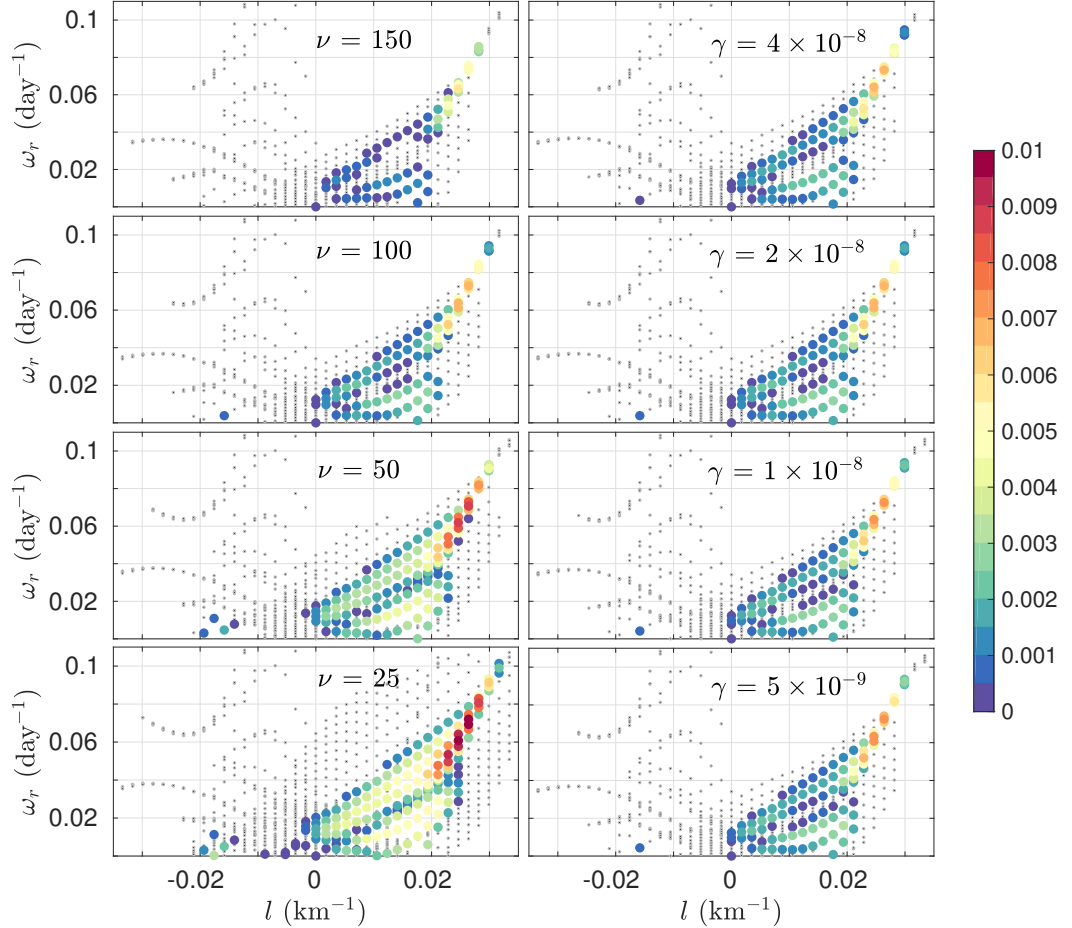


Figure 5.5: Real parts of eigenvalues (ω_r) obtained from the linear stability analysis for different values of eddy viscosity (left panels, for fixed $\gamma = 2 \times 10^{-8} \text{ s}^{-1}$) and bottom friction (right panels, for fixed $\nu = 100 \text{ m}^2 \text{s}^{-1}$) vs wavenumber. Growth rates (day^{-1}) are shown in the colorbar. Eigenmodes having growth rates in the range $[-0.01, 0]$ are shown with grey dots. Growth rates increase with decreasing ν and γ .

Frequencies obtained by solving the eigenvalue problem are shown in figure 5.5 for different magnitudes of the eddy viscosity and bottom friction parameters. It can be seen that eddy viscosity tends to stabilise the eigenmodes at all wavenumbers as the growth rates of the eigenmodes reduce with increasing the value of the eddy viscosity parameter. In fact, in the lower viscosity cases, many weakly unstable eigenmodes appear, which otherwise had negative growth rates (at wavenumbers smaller than 0.02 km^{-1}). These weakly unstable eigenmodes are present at relatively smaller wavenumbers than the wavenumbers of fastest growing mesoscale eddies, which are in the wavenumber range $0.02\text{--}0.03 \text{ km}^{-1}$. With a reduction in the value of the bottom friction parameter, the changes in the growth rates are less visible, but the growth rates do increase with decreasing γ . A few unstable modes can be seen appearing in the cases of weaker bottom friction (compare plots for $\gamma = 4 \times 10^{-8}$ and $\gamma = 2 \times 10^{-8} \text{ s}^{-1}$). Looking at the spatial structure of the fastest growing mode (figure 5.6), we find that the banana-shaped eddies are very similar to the

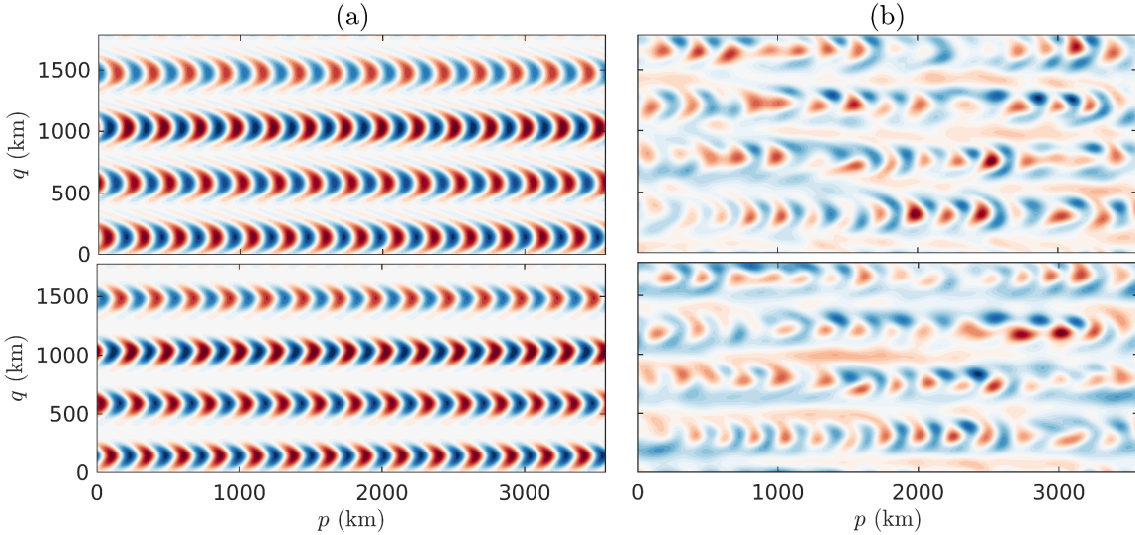


Figure 5.6: (a) The eigenvector corresponding to the fastest growing mode (b) Snapshots of the eddy field constructed using all EOFs except EOF1 and EOF2. Top and bottom panels correspond to the top and bottom layers, respectively. The snapshot of eddy field was constructed using the solution from the simulation run with $\nu = 150 \text{ m}^2 \text{ s}^{-1}$ (other parameters were the same as shown in table 2.1). In this case, there is a remarkable resemblance in the spatial structure between the eddy field and the fastest growing eigenmode. These banana-shaped eddies were also seen in the lower viscosity simulations; however, the banana-shaped structures appear less frequently because the eddy field tends to very complex in the presence of the Z mode.

eigenfunctions corresponding to the fastest growing mode in a flat-bottom case (see figure 13 in Berloff et al. (2011)). In fact, there is a good match between the banana-shaped eigenmode and eddy field reconstructed using all EOFs except the EOFs corresponding to J mode. This shows that the linear stability analysis is helpful in understanding the jet dynamics, even though the solutions considered in this study are highly nonlinear.

It is important to note here that, in the presence of the mean flow, even eigenmodes at very low wavenumbers have positive growth rates; however, the growth rates are very small. The presence of many weakly growing large-scale eigenmodes indicates that these eigenmodes can interact and exchange energy, as they can remain in the system for a sufficiently long time without dying. These results also suggest that, given the large-scale eigenmodes are weakly growing, the Z mode observed in some simulations must have received energy through nonlinear interactions among different eigenmodes, which can also be inferred from the KE spectrum contours in figure 5.2. The linear stability analysis shows that all eigenmodes are significantly damped due to eddy viscosity and there are fewer unstable modes present in the case of strong eddy viscosity. Consequently, the number of nonlinear interactions can reduce due to the presence of fewer energised eigenmodes and the efficiency of energy exchange among different eigenmodes can decline. This suggests that nonlinear interactions may have been suppressed in the simulations having strong dissipation and this can explain the absence of the Z mode in the EOF analysis in some cases (see table 5.2 for $\nu = 150, 200 \text{ m}^2 \text{s}^{-1}$ cases). It is possible that, in the simulations having strong viscous dissipation, there may not have been enough interactions to feed energy to the Z mode.

It is counterintuitive that, in the presence of the sloped topography, the system develops zonally elongated modes, which have meridional wavelengths longer than the meridional width of the tilted jets. Over a flat bottom, the β -effect leads to strong anisotropisation resulting in the formation of zonal jets, where the meridional width of the jets is set by a balance between nonlinear advection and Rossby waves (Rhines, 1975). Even in the presence of the sloped topography, the jets are initially formed by the action of mesoscale eddies and, later, the jets start to gain energy directly from the imposed vertical shear (see the discussion of figure 3.7). Hence, in a way, the width of the tilted jets is set by eddies and Rossby waves. However, the inhibition of the inverse energy transfer to meridional scales longer than the Rhines scale by Rossby waves is more of an indirect effect (Sukoriansky et al., 2007). The upscale energy transfer stops at the Rhines scale because, in order to transfer energy to lower meridional wavenumbers, the triad interactions would involve two almost parallel Fourier modes and such triad interactions are quite inefficient (Vallis and Maltrud, 1993). On the other hand, in the presence of the sloped topography, both zonal and tilted large-scale modes are present, as seen in the EOF analysis and two-dimensional KE spectra. We believe that the presence of many large-scale modes makes it possible to have efficient nonlinear interactions and transfer energy to meridional scales larger than the jet width. This could be the main reason why the Z mode is able to receive a significant amount of energy in the simulations.

In our analysis, we mainly discussed indirect evidence of efficient nonlinear interactions over topography using the two-dimensional KE spectra, in which we observed a significant increase in the number of nonlinear interactions in weak dissipation regimes. It may also be possible to test this hypothesis directly. One could try to identify the triads in which the Z mode gains energy or the J mode loses energy and compute energy exchange rates as a function of the magnitudes of the eddy viscosity and bottom friction parameters. The main issue with this kind of approach is that identifying all such triads, in which the Z mode gains energy or the J loses energy, is quite difficult. Also, it is difficult to confirm if the energy lost from the J mode ends up in the Z mode. The J mode need not transfer energy directly to the Z mode and it may take few interactions for the energy to reach the Z mode. Identifying specific triads is much more difficult than looking at the overall energy exchange at different wavenumbers, which is the general practice (e.g. see Khatri et al., 2018). There have been some efforts to compute energy exchanges in specific triads to understand the energy transfer process (Dar et al., 2001); however, the problem still remains quite difficult to tackle. This is beyond the scope of this thesis.

5.5 SUMMARY

In this chapter, we studied the dynamics of tilted jets, which gain energy directly from the imposed vertical shear, in weak dissipation regimes and also in the freely evolving turbulence regime. We find that, in addition to the tilted jets, many large-scale modes, which were extracted using the EOF analysis, coexist in the system. All of these large-scale scales modes possess spatiotemporal variability and can be broadly categorised into two families: the first family of tilted modes and the second family of purely zonal modes. The relative contributions of these modes to the full flow field are greatly affected by the magnitudes of the dissipative parameters. As we decrease the dissipation strength, the flow field tends to be dominated by purely zonal modes, which propagate meridionally and the propagation speed increases linearly with the slope magnitude and decreases roughly as the square of the meridional wavenumber. The analysis of the two-dimensional KE spectra show that these large-scale modes and mesoscale eddies can interact efficiently and exchange energy. As a result, the tilted jets lose energy to purely zonal modes. However, strong viscous dissipation tends to kill small-scale eddy activity resulting in the suppression of these nonlinear interactions, which we confirmed using the linear stability analysis performed around the time-mean state of the tilted jets in a moving frame of reference. These results suggest that, in the presence of topography, alternating jet patterns can also be formed via interactions among various large-scale modes and the meridional width of the jets need not follow the Rhines scaling (Rhines, 1975).

6

ROLE OF EDDY FLUXES IN THE MAINTENANCE OF JETS

The contents of this chapter have been published in the research article titled “*Role of eddies in the maintenance of multiple jets embedded in eastward and westward baroclinic shears*” in the *Fluids* journal (Khatri and Berloff, 2018b).

Mesoscale eddies interact with jets via exchanges of eddy momentum and buoyancy. In chapter 3, we observe that components of the eddy forcing term, i.e. Reynolds stress term and form stress term, affect the jets in different ways. In this chapter, we assess the impacts of eddy relative vorticity and buoyancy fluxes separately on zonal jets by analysing the time-mean potential vorticity (PV) budget in two-layer quasi-geostrophic (QG) simulations over a flat bottom. Another reason for studying the eddy vorticity and buoyancy effects separately is that the jet dynamics in a baroclinic QG model is significantly different from the jet dynamics in a barotropic QG model (Thompson and Young, 2007; Berloff et al., 2009a,b). For example, the rates of energy transfer to the mean zonal flow in individual layers via up-gradient momentum fluxes are significantly different, even in the case of a predominantly barotropic flow structure (Thompson and Young, 2007). In contrast to the previous chapters, in this chapter, both eastward and westward background shears have been considered, as oceanic jets can be formed in the presence of both types of background shears at different geographical locations, e.g., jets in oceanic midlatitude gyre circulations. It has been observed that the roles of eddy fluxes depend on the direction of the imposed vertical shear and this can lead to differences in the behaviour of barotropic-baroclinic (BT-BC) interactions (Berloff et al., 2009a,b, 2011). However, there is no clear understanding of how these differences arise due to a change in the direction of the mean vertical shear.

In this chapter, we compare our results with some of the previous studies that focused on the role of BT-BC interactions on the dynamics of jets. Here, we prefer to analyse the role of eddy fluxes in individual layers over using the BT-BC flow decomposition because, in the presence of the imposed vertical shear, the vertical eigenmodes have mixed barotropic-baroclinic structure (Berloff and Kamenkovich, 2013a,b). Assessing the role of eddies in terms of interacting barotropic and baroclinic modes is difficult and the interpretation of the dynamics in terms of the vertical modes can sometimes be misleading. Nevertheless, we compare the results with the previous works that studied the impacts of eddies on the barotropic and baroclinic flow structures of jets (Berloff et al., 2009a,b). We argue that the roles of the eddy fluxes are the same in systems forced with eastward and westward vertical shears, and the overall dynamics is largely the same. However, in terms of vertical modes, the eddy effects may look different.

6.1 DYNAMICS OF ZONAL JETS AND EDDIES

Here, we mainly focus on the roles of the Reynolds stress term and form stress term in the maintenance of jets (see equations (3.7-3.8)). For this purpose, we analyse the dynamics of jets and eddies over a flat bottom in systems forced with either an eastward or a westward vertical shear. For an eastward shear (ES), we imposed a background flow of 6 cm s^{-1} in the upper layer, whereas background flow of -4 cm s^{-1} was imposed in the upper layer to create a zonal westward shear (WS). Also note that, in the two-layer QG simulations used in this chapter, we used a rectangular domain having an area of $3000 \times 1500 \text{ km}^2$ with 1024×512 grid points and used periodic boundary conditions on all four sides of the domain. Also, we used $\beta = 1.6 \times 10^{-11} \text{ m}^{-1}\text{s}^{-1}$, which corresponds to a reference latitude of 45° , and $\nu = 25 \text{ m}^2\text{s}^{-1}$. The rest of the parameters were kept the same as shown in table 2.1. Similar to the simulations discussed earlier, we initialised the model from a perturbed state. The system quickly developed multiple jets and reached a statistical equilibrium state by 6-7 years (see section 2.3 for details). We ran the simulations for 20 years and used the last 10 years of data (about 180 snapshots) for computing the eddy fluxes and eddy forcing. The details are discussed in the next section.

In figure 6.1, the meridional profiles of the zonal velocity (averaged over the last 10 years as well as in the zonal direction) are shown. In both the ES and WS cases, alternating jets are present and the eastward jets are sharper than the westward jets. Also, the vertical flow structure is predominantly barotropic as we kept the strength of bottom friction quite weak, i.e. $\gamma = 2 \times 10^{-8} \text{ s}^{-1}$ (see section 2.1). However, there is one important difference between the two cases. In contrast to the ES case, the bottom layer is more energetic in the WS case and the jets are stronger in the bottom layer in comparison to the top layer. As a consequence, the mean barotropic, $\frac{H_1\bar{u}_1 + H_2\bar{u}_2}{H_1 + H_2}$, and baroclinic, $\bar{u}_1 - \bar{u}_2$, flow components are of opposite phases in the WS case. These observations are important

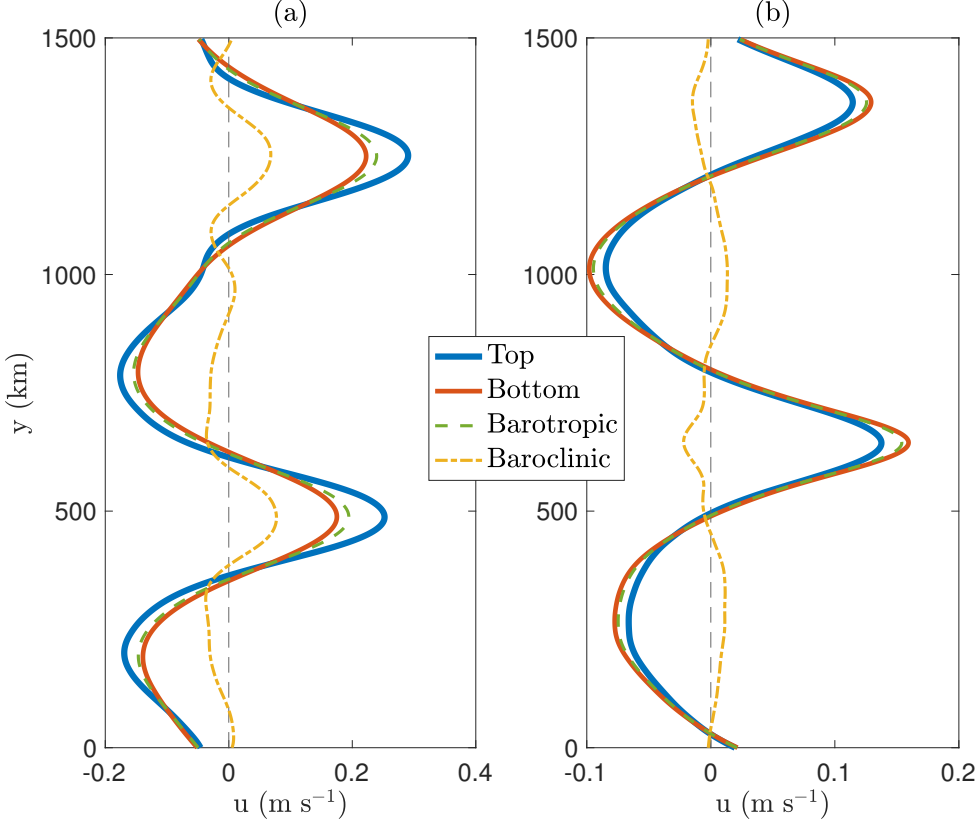


Figure 6.1: Adopted from Khatri and Berloff (2018b). Meridional profiles of the zonal velocity in the top and bottom layers (averaged in the zonal direction and time for the last 10 years); (a) ES and (b) WS. Dashed and dash-dotted curves represent the mean barotropic ($\frac{H_1\bar{u}_1+H_2\bar{u}_2}{H_1+H_2}$) and baroclinic ($\bar{u}_1 - \bar{u}_2$) components in the flow field, respectively.

in understanding the eddy dynamics and this is further discussed later in this chapter.

Similar to the technique adopted in chapter 3, we use the Reynolds decomposition to study the impacts of the Reynolds stress term and form stress term on the zonal jets. We decompose the flow field into the zonally averaged time-mean flow ($\bar{\psi}_i = \frac{1}{TL_x} \int_t \int_x \psi_i$, where T and L_x are the total time-period of averaging and the zonal extent of the domain, respectively) and transient eddy field ($\psi'_i = \psi_i - \bar{\psi}_i$). We use this decomposition in equation (2.1) and then average the equation in time as well as in the zonal direction. The resulting equations are given as

$$\frac{\partial}{\partial t} \underbrace{\left[\nabla^2 \bar{\psi}_i + \epsilon_i S_i (\bar{\psi}_2 - \bar{\psi}_1) \right]}_{\bar{q}_i} = \underbrace{-\nabla \cdot (\bar{\mathbf{u}}'_i \bar{\zeta}'_i)}_{\text{Rs}_i} - \underbrace{\epsilon_i S_i \nabla \cdot (\bar{\mathbf{u}}'_i (\bar{\psi}'_2 - \bar{\psi}'_1))}_{\text{Fs}_i} + \nu \nabla^2 \bar{\zeta}_i - \delta_{i2} \gamma \bar{\zeta}_i, \quad (6.1)$$

where $\mathbf{u} = (u, v) = (-\frac{\partial \psi}{\partial y}, \frac{\partial \psi}{\partial x})$ and $\zeta = \nabla^2 \psi$ (ψ is the velocity streamfunction) are the velocity and relative vorticity, respectively. $i = 1$ ($i = 2$) indicates the top (bottom) layer, δ_{i2} is the Kronecker delta and $\epsilon_1 = -\epsilon_2 = 1$. The overbar represents the mean in time as well as in the zonal direction. \bar{q}_i represents the layer-wise mean PV of the developed flow. The first two terms on the right-hand side (RHS) are convergence of eddy relative vorticity and eddy buoyancy fluxes in each layer. We refer to these eddy flux convergence terms

as Reynolds stress term (Rs_i) and form stress term (Fs_i). Depending on the sign, the stress terms can either sharpen or flatten the mean PV profile resulting in strengthening or weakening of the zonal jets (in this chapter, ‘mean PV’ is used to refer to the PV of the developed mean flow only). The sum of the Reynolds stress term and form stress term is generally referred to as ‘eddy forcing’ and, overall, the eddy forcing term is responsible for maintaining the zonal jets. The rest of the terms on the RHS remove energy from the system through viscous dissipation and bottom drag. In the time-mean, the time derivative of the mean PV vanishes and is kept only for clarity.

6.2 REYNOLDS AND FORM STRESS TERMS

In order to understand how the Reynolds stress term and form stress term affect the mean zonal flow, we compare the meridional profiles of the eddy stress terms and mean PV in each layer. In a baroclinic QG model, both relative vorticity and buoyancy contribute to the mean PV (see equation (6.1)). Thus, in order to make the comparison easier, we investigate the effects of individual stress terms on the mean relative vorticity and mean buoyancy separately. For this purpose, we computed correlation coefficients between the meridional profiles of the mean relative vorticity and mean buoyancy (note that buoyancy contribution due to the imposed background flow is not included) and the eddy stress terms.

The meridional profiles for both the ES and WS cases are shown in figure 6.2. The first important aspect to notice is that, in both cases, the Reynolds stress term is positively correlated with the mean relative vorticity profile in both layers (see table 6.1 for the correlation coefficients); thus, the Reynolds stress term forces the jets in the entire fluid column. In this scenario, eddies deposit momentum into the mean zonal flow and this process of up-gradient eddy momentum transfer is generally described as negative viscosity effect (Manfroi and Young, 1999; Dritschel and McIntyre, 2008). Indeed, the Reynolds stress terms in the top and bottom layers differ in strength and this is due to the importance of the baroclinic effects (Thompson and Young, 2007). In the ES case, the Reynolds stress term is more than five times stronger in the top layer than in the bottom layer. On the other hand, in the WS case, the Reynolds stress term is stronger in the bottom layer. The layer that experiences a stronger Reynolds stress term tends to be the more energetic layer (see figure 6.1). We discuss this aspect in detail later in the chapter.

On the other hand, the form stress term is negatively (positively) correlated with the mean buoyancy profile in the ES and WS cases (see table 6.1), respectively. This indicates that the form stress term has opposite effects on the mean zonal flow in the two cases. However, we argue that the behaviour of eddies is the same in both cases. A simple way to understand this is to look at the role of bottom friction in the system. Bottom

friction is the only large-scale energy sink in the model, which acts on the bottom layer. In both cases, eddies transfer momentum from the top to the bottom layer via the form stress term and this eddy momentum is then balanced by the bottom friction term. In the ES case, the mean flow in the top layer is stronger than the mean zonal flow in the bottom layer; hence, the eddy momentum transfer from the top to the bottom layer acts against the mean vertical shear ($\bar{u}_1 - \bar{u}_2$) in the system. Consequently, the form stress term acts opposite to the mean buoyancy in the system. This is similar to the case of Earth's atmosphere where baroclinic eddies transfer momentum from the middle atmosphere to the surface, which is then balanced by surface friction and the surface westerlies are produced (Edmon Jr et al., 1980). In contrast, in the WS case, the eddy momentum transfer from the top to the bottom layer tends to enhance (reduce) the strength of the mean zonal flow in the bottom (top) layer.

Layer	ES		WS	
	$\mathcal{C}(\nabla^2\bar{\psi}_i, \text{Rs}_i)$	$\mathcal{C}(\epsilon_i S_i(\bar{\psi}_2 - \bar{\psi}_1), \text{Fs}_i)$	$\mathcal{C}(\nabla^2\bar{\psi}_i, \text{Rs}_i)$	$\mathcal{C}(\epsilon_i S_i(\bar{\psi}_2 - \bar{\psi}_1), \text{Fs}_i)$
Top	0.89	-0.90	0.83	0.92
Bottom	0.08	-0.90	0.89	0.92

Table 6.1: Correlation coefficients, \mathcal{C} , computed by correlating the meridional profiles of the mean relative vorticity and buoyancy with the meridional profiles of the Reynolds stress term and form stress term. $i = 1$ ($i = 2$) indicates the top (bottom) layer and $\epsilon_1 = -\epsilon_2 = 1$.

In order to further confirm that the behaviour of eddies is the same in the two cases, we computed eddy heat diffusivity. In general, eddies tend to flatten the isopycnals as eddies extract energy from the available potential energy. As a consequence, the eddy buoyancy fluxes are down-gradient and this results in a positive heat diffusivity coefficient. In our study, we computed the heat diffusivity (μ_h) using the following relation (also see equation 3.9)

$$\mu_h = \frac{\overline{v'_i(\psi'_2 - \psi'_1)}}{\bar{u}_2 - \bar{u}_1 - U_b}, \quad (6.2)$$

where v'_i and ψ'_i are eddy meridional velocity and eddy streamfunction, respectively, in i^{th} layer. \bar{u}_i and U_b are the mean zonal flow and imposed background flow, respectively, and the overbar represents the mean in time as well as in the zonal direction. Note that the profiles of the heat diffusivity are the same in both layers as the layer-wise heat diffusivity expressions are mathematically equivalent. The meridional profiles of the heat diffusivity are shown in figure 6.3. In both the ES and WS cases, the heat diffusivity coefficients are positive and are of similar magnitudes. This confirms that the eddy buoyancy fluxes are down-gradient, which is in agreement with the theoretical expectations. However, there is an important difference in the heat diffusivity profiles. The locations of the heat diffusivity maxima relative to the jets are different in the two cases. In the ES case, the heat diffusivity coefficient is largest near the flanks of the eastward jets whereas, in the

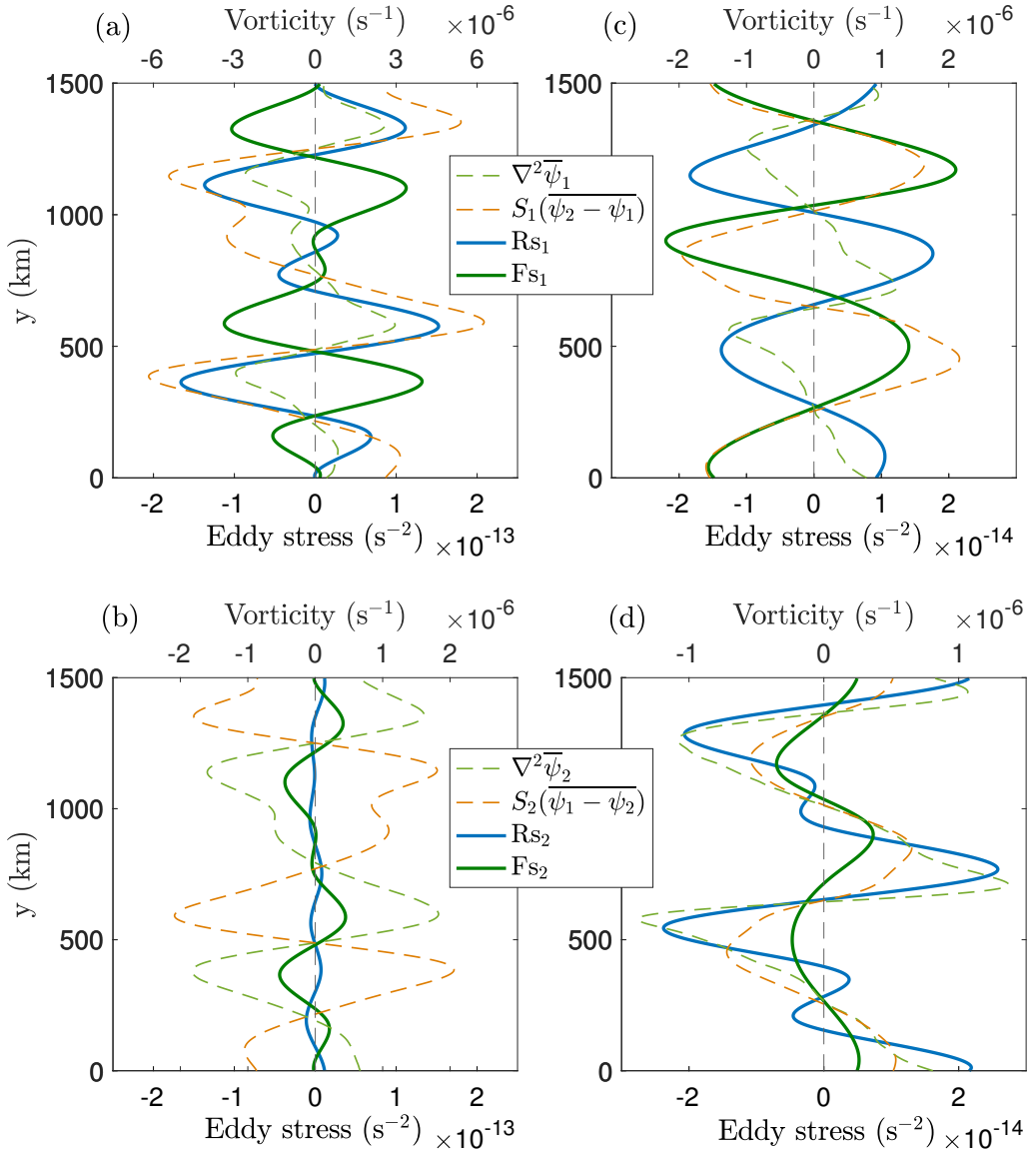


Figure 6.2: Adopted from Khatri and Berloff (2018b). Meridional profiles of the Reynolds stress term (solid blue) and form stress term (solid green) in the top (a,c) and bottom (b,d) layers. Left (a,b) and right (c,d) panels are for the ES and WS cases, respectively. The dashed curves represent the meridional profiles of the mean relative vorticity (dashed light green) and mean buoyancy (dashed orange). The profiles were averaged in the zonal direction as well as in time for the last 10 years. Additionally, the profiles of the stress terms were smoothed by applying moving averages in the meridional direction.

WS case, the maxima in the heat diffusivity profile coincide with the westward jet cores. This difference is due to the opposite directions of the imposed vertical shears in the two cases as the rest of the parameters are the same in both cases. However, we do not focus on this aspect in this thesis. Overall, the ES and WS cases are similar as eddies tend to flatten the isopycnals via down-gradient eddy buoyancy fluxes, although the locations of the heat diffusivity maxima are different.

We could also investigate how the form stress term affects the mean relative vorticity profile or the Reynolds stress term affects the mean buoyancy profile. However, these effects are not independent of what has been described above. For example, eddies transfer momentum from the top layer to the bottom layer via the form stress term; thus, the form

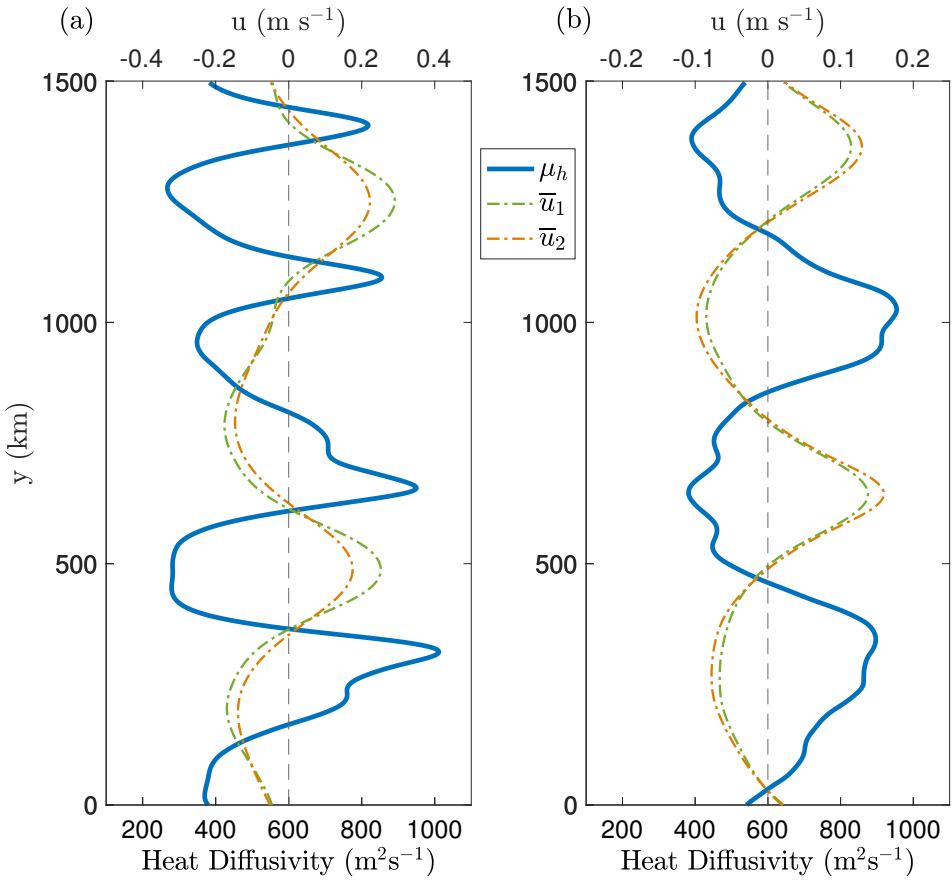


Figure 6.3: Adopted from Khatri and Berloff (2018b). Meridional profiles of heat diffusivity; (a) ES and (b) WS. The dash-dotted curves represent the meridional profiles of the mean zonal flow (averaged for the last 10 years) in the layers. A positive value of heat diffusivity indicates that eddy buoyancy fluxes are down-gradient.

stress term tends to reduce the strength of the mean flow in the upper layer and tends to enhance the mean flow strength in the lower layer. These effects are clearly captured in figure 6.2 as the form stress term is negatively (positively) correlated with the mean relative vorticity profile in the top (bottom) layer. In a similar manner, the Reynolds stress term has a positive (negative) correlation with the mean buoyancy in the more (less) energetic layer, which is consistent with the arguments given above. Eddies are responsible for maintaining the jets; thus, in the overall balance, the eddy stress terms drive the jets. In both the ES and WS cases, the Reynolds stress term forces the mean zonal flow in both layers whereas the form stress term transfers momentum from the top to the bottom layer. In a statistical equilibrium state, this additional momentum in the bottom layer is balanced by bottom friction. In essence, our layer-wise analyses show that the overall dynamics is largely the same in both the ES and WS cases.

6.3 ZONAL ENERGY BALANCE

We further analyse the energy exchanges between the zonal jets and eddies in individual layers. For this purpose, we derive the time-mean zonal energy balance by multiplying $-\bar{\psi}_i$ (overbar indicates the time-mean) to equation (2.1) and then averaging over the

whole domain (denoted by $\langle \cdot \rangle$) as well as in time (we followed the same steps as shown in Appendix A.3 to derive the energy equations),

$$\begin{aligned} \left\langle \frac{1}{2} \frac{\partial}{\partial t} \bar{u}_i^2 + \frac{S_i}{2} \frac{\partial}{\partial t} \bar{\psi}_i^2 \right\rangle &+ \left\langle -\delta_{i1} S_1 \bar{\psi}_1 \frac{\partial \bar{\psi}_2}{\partial t} - \delta_{i2} S_2 \bar{\psi}_2 \frac{\partial \bar{\psi}_1}{\partial t} \right\rangle \\ &= \left\langle \frac{\partial \bar{u}_i}{\partial y} \bar{u}'_i \bar{v}'_i - \epsilon_i S_i \bar{u}_i \bar{\psi}'_1 \frac{\partial \bar{\psi}'_2}{\partial x} - \nu \left(\frac{\partial \bar{u}_i}{\partial y} \right)^2 - \delta_{i2} \gamma \bar{u}_2^2 \right\rangle, \quad (6.3) \end{aligned}$$

where ϵ_i and δ_{ij} are the same as defined in equation (6.1). The first two terms on the RHS in equation (6.3) represent the energy exchange between the jets and eddies in individual layers. The first term captures the energy transfer from eddies to the mean zonal flow via up-gradient momentum fluxes in each layer. We refer to this term as ‘Reynolds stress correlations (RSC) term’, which basically represents the transfer of kinetic energy from eddies to the mean zonal flow. There is also a transfer of energy in the vertical direction as the upper and lower layers continuously interact. The second term on the RHS in equation (6.3) captures the energy exchange between individual layers via eddy buoyancy effects. We refer to this term as ‘form stress correlations (FSC) term’ from here onwards. The rest of the terms on the RHS in equation (6.1) represent the loss of the mean zonal energy through eddy viscosity and bottom friction. A single energy balance equation can be derived for the zonal mean flow. In order to do that, we multiply the above layer-wise energy equation by H_i and then added the equations. The final energy equation is given as

$$\begin{aligned} \frac{\partial}{\partial t} \left\langle \sum_{i=1}^2 \frac{H_i}{2} \bar{u}_i^2 + \frac{H_1 S_1}{2} (\bar{\psi}_1 - \bar{\psi}_2)^2 \right\rangle &= \left\langle \sum_{i=1}^2 H_i \frac{\partial \bar{u}_i}{\partial y} \bar{u}'_i \bar{v}'_i + H_1 S_1 (\bar{u}_2 - \bar{u}_1) \bar{\psi}'_1 \frac{\partial \bar{\psi}'_2}{\partial x} \right\rangle \\ &\quad \left\langle -\nu \sum_{i=1}^2 H_i \left(\frac{\partial \bar{u}_i}{\partial y} \right)^2 - \gamma H_2 \bar{u}_2^2 \right\rangle. \quad (6.4) \end{aligned}$$

In the statistical equilibrium, the sum of the domain integrated kinetic energy and potential energy in the system is conserved and the terms on the RHS in equation (6.4) exactly balance each other (see table 6.2). In both the ES and WS cases, the mean zonal flow gains energy through the RSC terms in both layers and bottom friction removes most of the energy from the system. In both cases, the FSC terms transfer energy from the upper to the lower layer. This is in agreement with our hypothesis that eddies always transfer momentum from the top to the bottom layer and, in an energy equilibrium state, this additional momentum is dissipated through bottom friction. One important aspect to consider is that the magnitudes of the RSC terms greatly differ in individual layers and a similar disparity was also observed in the strength of the Reynolds stress terms (see figure 6.1). We discuss this aspect in detail later in this chapter.

The meridional profiles of the RSC, FSC and dissipation terms in equation (6.3) are shown in figure 6.4. The magnitudes of the terms significantly vary in the meridional

	ES			
Layer	$\langle H_i \bar{u}_{iy} \bar{u}'_i v'_i \rangle$	$\langle -\epsilon_i H_i S_i \bar{u}_i \bar{\psi}'_1 \bar{\psi}'_{2x} \rangle$	$\langle -H_i \nu \bar{u}_{iy}^2 \rangle$	$\langle -\delta_{i2} H_i \gamma \bar{u}_i^2 \rangle$
Top ($i = 1$)	11.42	-9.98	-0.56	-
Bottom ($i = 2$)	0.84	7.77	-0.84	-8.32
	WS			
Layer	$\langle H_i \bar{u}_{iy} \bar{u}'_i v'_i \rangle$	$\langle -\epsilon_i H_i S_i \bar{u}_i \bar{\psi}'_1 \bar{\psi}'_{2x} \rangle$	$\langle -H_i \nu \bar{u}_{iy}^2 \rangle$	$\langle -\delta_{i2} H_i \gamma \bar{u}_i^2 \rangle$
Top ($i = 1$)	0.77	-0.86	-0.11	-
Bottom ($i = 2$)	3.18	0.97	-0.40	-3.56

Table 6.2: Energy exchange between the mean zonal flow and eddies through the RSC and FSC terms, and energy loss through viscous dissipation and bottom friction terms (averaged over the whole domain and time for the last 10 years) in the top and bottom layers. The units are in $10^{-7} \text{ m}^3 \text{s}^{-3}$. δ_{ij} is the Kronecker delta and $\epsilon_1 = -\epsilon_2 = 1$.

direction and this is strongly correlated with the meridional profile of the mean zonal flow. For example, the RSC terms are strongest in the regions of the eastward jets as eddies deposit momentum into the eastward jet cores. On the other hand, the FSC terms act against the eastward jets in the more energetic layer and force the mean zonal flow in the less energetic layer in both the ES and WS cases. Although the effects of the layer-wise FSC terms on the zonal jets look opposite in the ES and WS cases, the overall energy transfer via the FSC terms is still from the top to bottom layer (see table 6.2). The majority of this energy gain in the lower layer is dissipated through bottom friction. Hence, the overall impact of eddy buoyancy fluxes is the same in both the ES and WS cases. Eddies transfer energy from the top to the bottom layer where it is dissipated through bottom friction.

6.4 EFFECT OF BOTTOM FRICTION

Friction plays an important role in governing the ocean dynamics and greatly affects the strength of large-scale ocean currents (Dewar, 1998). Berloff et al. (2011) studied the impacts of bottom friction on zonal jets and ambient eddies in a baroclinic QG model and found that bottom friction affects the vertical structure of the multiple jets. Here we investigate how bottom friction affects the baroclinic structure of the flow (see equation (6.1) for the bottom layer). It can be inferred from figure 6.2 that bottom friction has opposite effects on the baroclinic structure in the ES and WS cases, as the meridional profiles of the bottom friction term, $-\gamma \nabla^2 \bar{\psi}_2$, and baroclinic streamfunction, $\bar{\psi}_1 - \bar{\psi}_2$, are positively (negatively) correlated in the ES (WS) case. This shows that bottom friction tends to make the flow more baroclinic (barotropic) in the ES (WS) case.

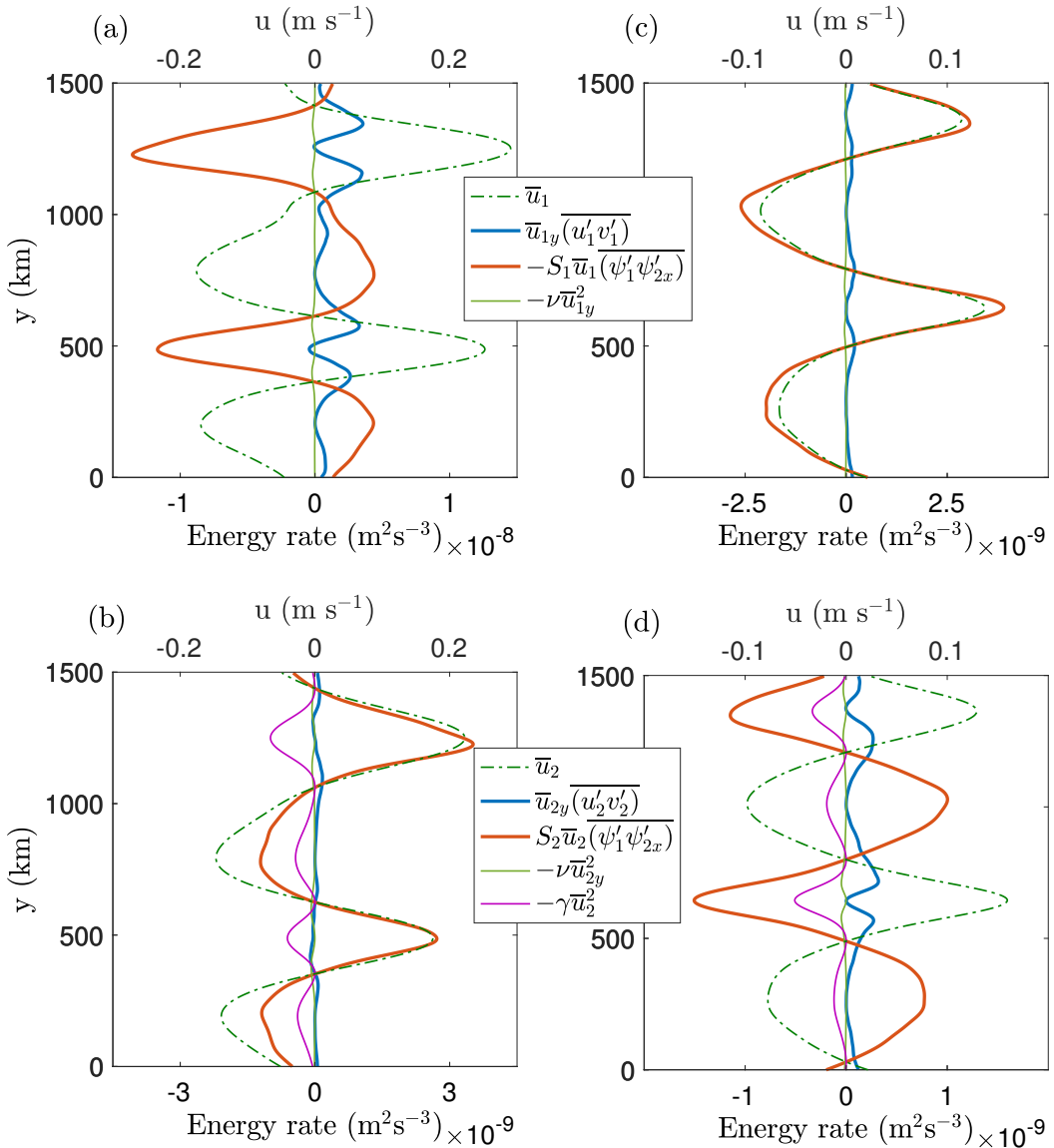


Figure 6.4: Adopted from Khatri and Berloff (2018b). Meridional profiles of the RSC, FSC and dissipation terms; (a,b) ES (c,d) WS. \bar{u}_{iy} and ψ_{2x} represent the meridional and zonal gradient of the mean zonal velocity and bottom-layer streamfunction, respectively. Top and bottom panels correspond to the upper and lower layers, respectively. The layer-wise mean zonal velocity is represented by dash-dotted curves. The profiles were averaged in the zonal direction as well as in time for the last 10 years.

The difference can simply be understood by looking at the mean zonal velocity profiles (figure 6.1). The jets are stronger in the top and bottom layers in the ES and WS cases, respectively. This is because the top and bottom layers receive more energy through the RSC terms in the two cases (see figure 6.4). In both cases, most of the energy is dissipated through bottom friction (table 6.2), which primarily affects the flow in the lower layer. Hence, bottom friction tends to enhance (reduce) the difference between the mean zonal velocity magnitudes between the upper and lower layers in the ES (WS) case. As a consequence, the vertical flow structure tends to be more baroclinic (barotropic) in the ES (WS) case. Although the overall behaviour of eddies and dynamics are the same in the ES and WS cases, the impact of bottom friction on the baroclinic structure is the opposite.

6.5 COMPARISON WITH PREVIOUS STUDIES

Our layer-wise analysis of the roles of eddy fluxes shows that the overall eddy dynamics remains the same in systems forced with eastward and westward vertical imposed shears. In contrast, some previous works have found that the direction of the imposed vertical shear significantly affects the behaviour of eddy fluxes. For example, Berloff et al. (2009a,b) used BT-BC decomposition in the time-mean PV balances and analysed the impacts of nonlinear eddy stress terms on the barotropic and baroclinic structures of zonal jets. They observe that the impacts of the Reynolds stress and form stress terms are opposite in eastward and westward sheared systems. In the former, eddies tend to maintain the baroclinic jets through the Reynolds stress term while the form stress term acts against the baroclinic jets. In the latter case, on the other hand, the Reynolds (form) stress term tends to destroy (maintain) the baroclinic structure of the zonal jets. Although the role of eddy fluxes in the BT-BC analyses look significantly different in the two scenarios, we argue that the overall eddy dynamics remains the same and the observed differences can be understood by analysing the baroclinic flow structures in the ES and WS cases (see figure 6.1).

The mean zonal velocities of the barotropic ($\frac{H_1\bar{u}_1+H_2\bar{u}_2}{H_1+H_2}$) and baroclinic ($\bar{u}_1 - \bar{u}_2$) flow components are in phase in the ES case, i.e., the maxima and minima in the mean barotropic and baroclinic velocities occur at the same latitudes. In the WS case, the jets are stronger in the lower layer as the jets receive more energy through the RSC term in the lower layer. As a result, the barotropic and baroclinic components of the mean flow are in the opposite phases. This reversal in the phase of the baroclinic flow component is the key reason why the impacts of the Reynolds stress and form stress terms on the baroclinic flow structure of the jets look opposite in systems forced with eastward and westward vertical shears. In fact, even in this study, we make a similar observation. The meridional profiles of the mean buoyancy and form stress term are negatively (positively) correlated in the ES (WS) case (figure 6.2), even though eddies transfer momentum from the top to the bottom layer in both cases. The same effect leads to a reversal in the impact of bottom friction on the baroclinic flow structure, which is discussed in the previous section. In order to avoid the reversal in the baroclinic flow component, one could define the baroclinic mode on the basis of the energy of the mean zonal flow in the layers; e.g., $\psi_1 - \psi_2$ and $\psi_2 - \psi_1$ in the ES and WS cases, respectively. This approach would ensure that the barotropic and baroclinic flow components are always in phase and the roles of the eddy stress terms would be the same.

It is important to remember that, although the overall eddy dynamics is the same in both the ES and WS cases, local eddy shapes and their meridional structure can still be different in eastward and westward sheared systems (e.g. see the discussion in Berloff and Kamenkovich, 2013a,b). In this work too, we observe that the maxima in the meridional

profiles of eddy heat diffusivity in the ES and WS cases occur at different latitudes in relation to the zonal velocity maxima of the jets. These differences may have important implications in the oceans; however, studying the impacts of the vertical shear direction on characteristics of eddy shapes is beyond the scope of this work.

6.6 DISPARITY IN THE UPPER AND LOWER LAYER REYNOLDS STRESS CORRELATIONS

We observe that the rates of the energy transfer to the zonal jets from eddies via the RSC terms are significantly different between the upper and lower layers. In the ES case, the upper-layer RSC term is larger in magnitude while, in the WS case, the lower-layer RSC term dominates (table 6.2, meridional profiles of the RSC terms are also shown in figure 6.5). As a consequence, the layer receiving more energy through the RSC term tends to be more energetic (see figure 6.1). This is in agreement with Thompson and Young (2007) who found that the mean zonal flow receives almost all of the energy via the upper-layer Reynolds stresses in a baroclinic QG model forced with an eastward velocity shear.

This strong disparity in the strength of the RSC terms is surprising because the vertical flow structure is predominantly barotropic and the layers are not significantly different in terms of kinetic energy levels (see figure 6.1). Thus, eddies are also expected to be of similar magnitudes in the upper and lower layers. Given this, it is not obvious why eddies are significantly more efficient in transferring momentum to the jets in one of the layers. This indicates that the baroclinic flow structure is important for understanding the jet dynamics as eddies transfer a significant amount of energy between the layers, and this effect cannot be captured in a barotropic model. Also, despite imposing a westward background flow in the upper layer, the lower layer tends to be more energetic in the WS case. This shows that only the direction of the vertical shear is important. For example, another way to create a westward vertical shear is to impose an eastward background flow in the lower layer. In this scenario too, the lower layer would be more energetic.

Similar enhancement in the strength of Reynolds stresses is seen in Earth's atmosphere. It is well known that eddy momentum flux (EMF) convergence peaks in the upper troposphere and its magnitude sharply decreases in the lower troposphere (see figure 1 in Ait-Chaalal and Schneider, 2015). It is believed that strong friction tends to reduce eddy magnitudes near the surface resulting in a reduction in the EMF strength (Held, 2007; Vallis, 2017). The Earth's atmosphere experiences an eastward vertical shear due to more heating at the equator than at the poles and this is equivalent to the ES case in this study. Ait-Chaalal and Schneider (2015) performed an idealised experiment in which they heated the poles more than the equator resulting in a westward shear, which is equivalent our WS case. They find that the EMF maxima shift to the lower troposphere, which is similar to the observations made in the WS case in our study, and the results are not very sensitive to the strength of surface friction. Thus, it is unlikely that

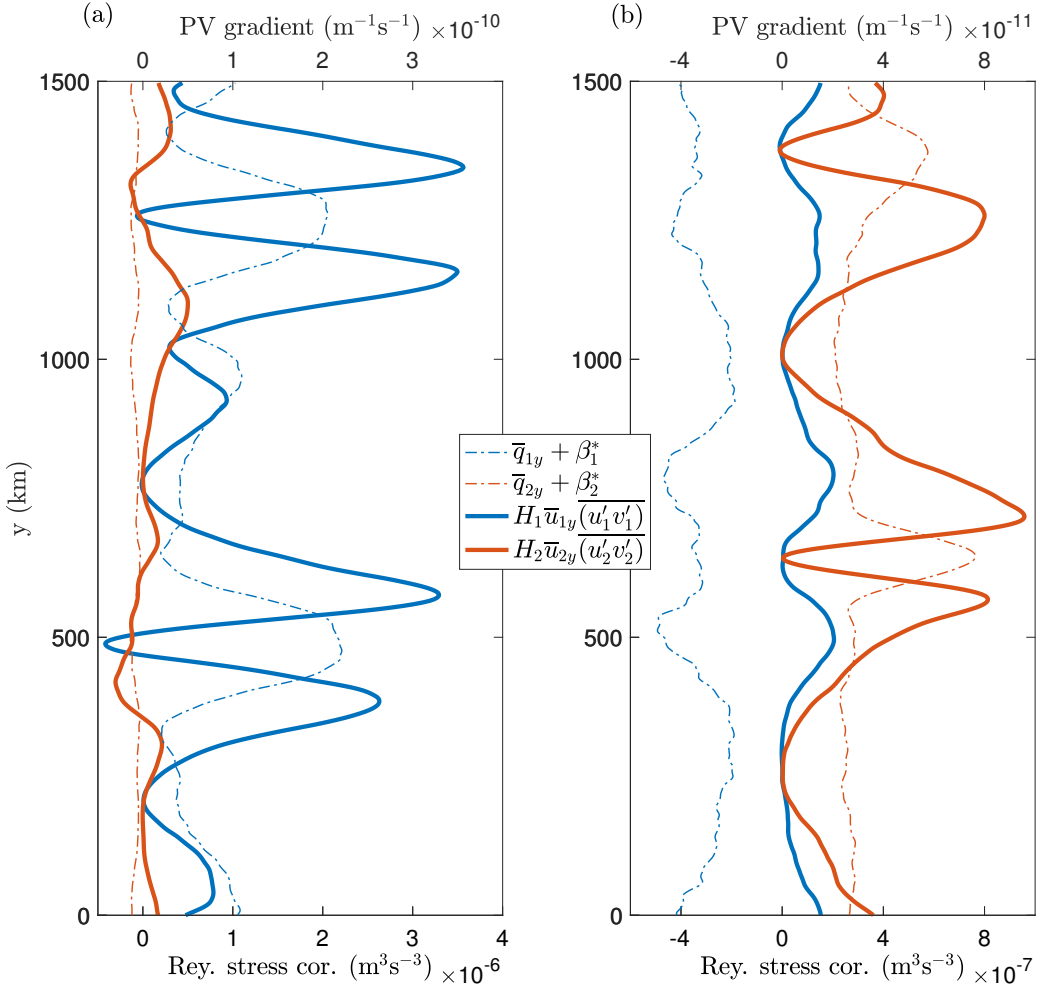


Figure 6.5: Adopted from Khatri and Berloff (2018b). Meridional profiles of layer-wise energy transfer from eddies to the zonal jets through RSC terms (solid) and the meridional gradient in the layer-wise full PV (dash-dotted); (a) ES (b) WS. \bar{u}_{iy} and \bar{q}_{iy} are the meridional gradient of the mean zonal velocity and mean PV, respectively, and $\beta_i^* = \beta + \epsilon_i S_i U_b$ ($\epsilon_1 = -\epsilon_2 = 1$) is the background PV gradient in i^{th} layer. The profiles were averaged in the zonal direction as well as in time for the last 10 years. The jets receive more energy through RSC term in the upper (lower) layer in the ES (WS) case.

surface friction controls the EMF strength in the atmosphere. Ait-Chaalal and Schneider (2015) further propose that the magnitude of EMF is associated with the absorption of wave activity due to eddy-eddy interactions in the atmosphere. However, it still remains unclear why the wave activity absorption tends to be much stronger in one part of the atmosphere. It has been suggested that, in Earth's atmosphere, the EMF maxima are associated with greater magnitudes of meridional PV gradients in the upper troposphere than in the lower troposphere (Held, 2007). However, the reasoning is not completely satisfactory, as the magnitudes of meridional PV gradients change gradually with height whereas EMF possess a sharp peak in the upper troposphere.

In order to better evaluate the role of eddies in the large-scale circulations of the oceans and atmosphere, it is crucial to understand how eddies redistribute momentum and what controls the strength of this momentum redistribution as a function of depth. In our study, we observe that, in both cases, the layer having a positive background PV

gradient in the meridional direction receives more energy through the RSC terms (figure 6.5). Further, in order to find out if the magnitudes of meridional PV gradients play any role in controlling the strength of the RSC terms, we ran additional simulations in which we imposed background flows of -3 and -5 cm s^{-1} in the upper layer, respectively. As a result, we created a larger magnitude of the background meridional PV gradient in the lower (upper) layer in $U_b = -3 \text{ cm s}^{-1}$ ($U_b = -5 \text{ cm s}^{-1}$) case. In all three simulations ($U_b = -3, -4, -5 \text{ cm s}^{-1}$), we find that the RSC term in the lower layer tends to be stronger resulting in more energetic lower layer. This is in contrast to the belief that larger meridional PV gradients in the upper troposphere may be associated with the enhanced EMF convergence (Held, 2007).

In order to understand this disparity in the upper and lower-layer RSC terms, we analyse the layer-wise eddy momentum fluxes more carefully. The classical argument says that stirring due to baroclinic eddies produces an eastward flow (see figure 17.2 in Vallis, 2017). The eddy stirring generates Rossby waves that propagate away from the region of stirring and carry energy with them. These Rossby waves eventually fade away or break, and dissipate. Consequently, there is a strong convergence of eddy momentum into the stirring region resulting in an eastward flow in the stirring region and a westward flow in the wave breaking region (Dickinson, 1969; Thompson, 1971, 1980). The same argument can be applied to the problem of multiple jets. We can infer from figure 6.5 that, in both the ES and WS cases, there is a convergence of eddy momentum into the eastward jets in both layers as the RSC terms peak on the flanks of the eastward jets. This indicates that the eastward jet cores (EJC) correspond to the eddy stirring maxima and, on average, Rossby waves carry energy from the regions of the eastward jets to the westward jet regions. Thus, the group velocity of Rossby waves is directed away from the EJC as the direction of the energy propagation is along with the Rossby wave group velocity. We analyse the layer-wise group velocity vectors and corresponding eddy momentum transport in the linearised two-layer QG model. For simplicity, we treat the layers independent of each other by neglecting the buoyancy term perturbations in PV and also neglect the presence of the mean zonal flow. With these assumptions, we derived approximate expressions for the layer-wise dispersion relation and group velocity by substituting $\psi_i = \tilde{\psi}_i e^{j(k_x x + k_y y - \omega t)}$ in equation (2.1), which are given as (for a brief review, refer section 15.1.2 in Vallis, 2017)

$$\omega_i \approx \delta_{i1} U_b k_x - \frac{\beta_i^* k_x}{k_x^2 + k_y^2}, \quad (6.5)$$

$$C_{gi}^y = \frac{\partial \omega_i}{\partial k_y} \approx \frac{2\beta_i^* k_x k_y}{(k_x^2 + k_y^2)^2}, \quad (6.6)$$

where ω_i and C_{gi}^y are the frequency and meridional group velocity of Rossby waves, respectively, in i^{th} layer and $\beta_i^* = \beta + \epsilon_i S_i U_b$ is the background PV gradient in the meridional

direction. k_x and k_y are the zonal and meridional wavenumbers, respectively. δ_{i1} is the Kronecker delta and $\epsilon_1 = -\epsilon_2 = 1$. Indeed, the dynamics of Rossby waves is more complex than simple plane waves due to the coupling between the layers and due to the presence of multiple jets. The aim here is only to qualitatively understand the eddy impacts in terms of group velocity vectors and investigate why the magnitudes of the RSC terms are different in the upper and lower layers. Neglecting the mean zonal flow and buoyancy perturbation term are major assumptions in our approach. Since Reynolds stresses only depend on the eddy field, the presence of jets makes little difference. Also, Reynolds stresses are not affected by the vertical flow structure. Hence, the usage of the simplified expressions for the dispersion relation is reasonable for our purposes.

Further, we assume that the Rossby wave group velocity is directed away from the EJC in both layers as Rossby waves carry energy away from the region of stirring (Thompson, 1971). Our assumption of more stirring by eddies in the eastward jet regions is only based on figure 6.5 and we do not have any physical reasoning for this. In response to the energy carried by Rossby waves away from the EJC, there is a convergence or divergence of momentum in the EJC. For a disturbance of the form $\psi'_i = A_i e^{i(k_{xx}x + k_{yy}y - \omega_i t)}$ in i^{th} layer (A_i is some magnitude), associated zonally averaged momentum flux in the meridional direction is given as (Vallis, 2017)

$$\overline{u'_i v'_i} = -\frac{k_x k_y A_i^2}{2}. \quad (6.7)$$

The direction of momentum flux transfer by eddies depends on the sign of $k_x k_y$, which can be determined from equation (6.6). By construction, β_i^* is of the opposite signs in the upper and lower layers. This is required for the system to be baroclinically unstable (Charney and Stern, 1962); and thus, generate eddies. β_i^* is positive (negative) in the upper (lower) layer in the ES case, whereas it is positive (negative) in the lower (upper) layer in the WS case. In order to have the group velocity directed away from the EJC, for positive β_i^* , we have $k_x k_y > 0$ ($k_x k_y < 0$) to the northward (southward) of the EJC. Consequently, we have $\overline{u'_i v'_i} < 0$ to the northward of the EJC and $\overline{u'_i v'_i} > 0$ to the southward of the EJC and this results in a convergence of eddy momentum into the eastward jets. Hence, eddies tend to make the jets stronger. On the other hand, for negative β_i^* , we have $k_x k_y < 0$ ($k_x k_y > 0$) to the northward (southward) of EJC, which predicts a divergence of eddy momentum from the EJC and eddies tend to act against the jets. The analysis predicts that eastward jets are forced by eddies only for a positive background PV gradient in the meridional direction and Reynolds stresses are more efficient in the top (bottom) layer in the ES (WS) case, which is clearly seen in figure 6.5. In general, eddies need not transfer momentum in opposite directions in the upper and lower layers. The Reynolds stresses may still force the jets in both layers as the dynamics in the two-layer QG model is more complex, which is not captured in our simplified approach. However, it is quite likely that the opposite signs of the layer-wise

background meridional PV gradients would still affect the strength of Reynolds stresses.

Indeed, equations (6.5-6.6) are a huge simplification and neglecting the jets and buoyancy terms in the PV cannot be justified easily. The Rossby wave group velocity is affected by the presence of the mean flow and vertical flow structure. However, the aim of this work is only to qualitatively understand the differences between the upper and lower-layer eddy momentum fluxes on the basis of the Rossby wave group velocity direction vectors, which we inferred from the fully nonlinear simulations (figure 6.5). Our analysis provides us with a reasonable explanation of why there should be a disparity in the strength of the upper and lower-layer eddy momentum fluxes. Although we only considered the layer-wise background PV gradients, the argument is also valid for the layer-wise full PV gradients because the signs of PV gradients in the fully developed flow field are the same as the signs of the background PV gradients (see figure 6.5). Although our simplified approach explains the differences in the strength of the layer-wise RSC terms, the main limitation of our approach is that it cannot predict the relative strengths of the RSC terms in individual layers. Also, our method does not provide any information about the wavenumbers that contribute the most to eddy momentum flux convergence/divergence. Further work that accounts for the presence of jets and buoyancy terms is required to address these aspects.

6.7 SUMMARY

In this chapter, we analysed the roles of the Reynolds stress and form stress terms in the maintenance of zonal jets over a flat bottom. We find that the Reynolds stress term forces the jets via up-gradient momentum fluxes in the entire fluid column and the form stress term is responsible for transferring momentum from the upper to the lower layer where it is balanced by bottom friction. Here, we compared the results in systems forced with either an eastward background shear or a westward shear. We show that, despite some local differences in eddy structure and heat diffusivity, the overall eddy dynamics is the same in the two cases. This looks somewhat in contrast to the works of Berloff et al. (2009a,b), who concluded that the Reynolds and form stress terms have opposite effects on baroclinic jets in systems forced with an eastward vs a westward vertical shear. However, the differences between our results and previous works are caused by the phase reversal of the baroclinic flow in the WS case, in which the barotropic and baroclinic flows are in opposite phases as the bottom layer is more energetic (figure 6.2). Because of this reversal, the eddy effects look opposite, even though the overall dynamics is the same. Thus, the results presented in this study are consistent with Berloff et al. (2009a,b).

We also observe that the strength of the energy transfer to the jets from eddies through Reynolds stresses tends to be significantly different in the upper and lower layers (table 6.2), even though the vertical flow structure is predominantly barotropic (also

see Thompson and Young, 2007). The RSC term tends to be stronger in the layer that experiences a positive meridional PV gradient. In order to understand this, we used simplified layer-wise Rossby wave group velocity expressions and analysed the phase vectors associated with the momentum transfer by eddies in the meridional direction. In general, an eastward flow can be generated by stirring due to baroclinic eddies, in which Rossby waves carry energy away from the stirring regions resulting in the convergence of eddy momentum into eastward jets (Dickinson, 1969; Thompson, 1971, 1980). We find that convergence of eddy momentum into eastward jets occurs only for positive meridional PV gradients and this explains the differences in the strength of the layer-wise RSC terms. Note that our approach is qualitative as we treated the layers as independent of each other and neglected the presence of the jets. One should proceed with caution if a similar method is used in other scenarios.

7

CONCLUSIONS

The oceans are populated with alternating jet patterns, which play an important role in ocean transport and mixing (Thompson, 2008). These jets are seen to possess spatial and temporal variability, as jets can drift and mix/merge with other multiple jets (Sokolov and Rintoul, 2007; Thompson and Richards, 2011). This jet variability is believed to be primarily due to the presence of ocean bathymetry, which also affects the cross-jet transport (Thompson and Richards, 2011; Thompson and Sallée, 2012). In general, ocean bathymetry greatly affects the large-scale ocean circulation (Hogg and Munday, 2014), as nonuniform bathymetry creates spatially nonuniform potential vorticity (PV) gradients (Radko and Kamenkovich, 2017). As a consequence, eddy activity and transport properties change significantly around topographic features (Thompson and Sallée, 2012; Tamsitt et al., 2017).

In this thesis, we studied the dynamics of multiple jets over a zonally sloped topography in the two-layer quasi-geostrophic (QG) model forced with a uniform background vertical velocity shear. Idealised QG models have been quite effective in understanding the impacts of topography on the jet dynamics. For example, Thompson (2010) studied the jet formation over a two-dimensional sinusoidal topography and found that eddy transport in the meridional direction increases with increasing the topographic steepness. Boland et al. (2012) studied the jet dynamics over a zonal topographic slope and showed that jets tilt from the zonal direction, as the jets tend to align with the tilted barotropic PV isolines, and drift meridionally (also see Chen et al., 2015). However, it is not completely clear why jets tend to drift over topography. In this work, we analysed the dynamics of jets formed over a zonally sloped topography and mainly focused on the drifting behaviour of jets. Additionally, we investigated how topography affects the jet-eddy interactions and how it impacts the large-scale circulation. The conclusions of

this thesis are in the following sections.

7.1 JET DRIFT AND THE LINEAR DYNAMICS

In chapter 3, we studied how topography induces jet drift. In numerical simulations run with different slope magnitudes, we observe that the jets tilt from the zonal direction and drift meridionally with a constant speed. Both the tilt angle and drift speed increase with the slope magnitude, which is in agreement with Boland et al. (2012). In order to understand why the jets drift, we analysed the time-mean PV balances in the state of statistical equilibrium. In order to separate the jets and eddies, we rewrote the governing dynamical equations in a frame of reference moving with the jets such that the jets appear completely stationary and zonal in the new frame of reference. We decomposed the flow field into the time-mean flow and eddy field in the moving frame of reference and derived the time-mean PV balances. In addition to nonlinear stress terms (eddy forcing), linear stress terms appear in the time-mean PV balances due to the presence of topography. We then computed correlation coefficients between the cross-jet time-mean profiles of the stress terms and mean PV profiles.

We find that the linear stress terms are much stronger than the non-linear eddy forcing terms and the linear dynamics largely controls the jet drift. The jet drift velocities agree well with the phase velocities of linear Rossby waves computed using the linear dispersion relation. Moreover, in the overall balance, the jets are directly forced by the linear stress terms, which are directly proportional to the mean flow itself, and eddies act against the jets. Since the forcing term is directly proportional to the mean flow, by construction, the maxima in the cross-jet profiles of the forcing terms and mean PV are not aligned and have a large offset. As a result of this off-core forcing term, the jets are pushed in the meridional direction. From the perspective of PV conservation, the jets drift meridionally to compensate for the PV advection by the mean flow across the mean PV isolines. This is also in agreement with the hypothesis of Boland et al. (2012). Note that the results are limited to mild topographic slopes and non-linear eddy effects may be significant in the presence of steep topography.

7.2 JET-TOPOGRAPHY INTERACTIONS

We observe that the jets are directly forced by the linear stress terms (see chapter 3), which are proportional to the mean flow itself. Further analysis revealed that the tilted jets are coupled to the imposed background shear and the jets are able to extract energy directly from the background shear. In fact, for sufficiently large slopes, the energy gain by the jets from the imposed shear can even be more than the energy gain by mesoscale eddies through the baroclinic instability process (see chapter 4). Also, the total energy

gain by the jets and eddies from the imposed shear increases with the slope magnitude and the system tends to be more energetic, which is in agreement with earlier studies (Arbic and Flierl, 2004b; Smith, 2007; Boland et al., 2012).

On the other hand, eddies tend to act against the jets and gain energy from the jets. This is in contrast to the conventional view that jets are forced by mesoscale eddies (Rhines, 1975; Panetta, 1993; Berloff et al., 2009a). We further decomposed the eddy forcing term into the Reynolds stress term and form stress term to look at their impacts on the jets. The behaviour of the Reynolds stress and form stress terms is the same as in the case of stationary zonal jets. The form stress term opposes the jets as eddies grow by converting the mean available potential energy into kinetic energy, whereas the Reynolds stress term forces the jets (Thompson and Young, 2007; Berloff et al., 2009a). In the overall balance, the form stress term dominates over the Reynolds stress term in the presence of the sloped topography and the net impact of the eddy forcing is to weaken the jets. We reached the same conclusion when we looked at eddy fluxes of eddy relative vorticity and buoyancy.

Another important observation we made is that eddy kinetic energy increases with the slope magnitude as eddies gain energy from both the tilted jets and imposed background shear. Moreover, stronger eddy activity can enhance net cross-jet transport. We computed eddy heat and PV diffusivities as a function of the slope magnitude and find that the diffusivity coefficients increase with the topographic steepness, which is in agreement with the works of Thompson (2010); Boland et al. (2012). Note that these previous studies computed effective diffusivities in a stationary frame of reference; hence, their formulation included the effects of both the jets and eddies. On the other hand, in this work, the diffusivity computations were performed in the moving frame of reference and only the eddy fluxes were considered in the computations.

7.3 JET DYNAMICS IN WEAK DISSIPATION REGIMES

The results discussed above are limited to continuously forced-dissipative systems, in which the energy gain from the imposed background shear is balanced by viscous dissipation and bottom friction. In chapter 5, we studied the dynamics of tilted jets in weak dissipation regimes. We observe that, in addition to the tilted jets, many large-scale alternating patterns, which were extracted using the Principal Component Analysis, can coexist in the system. These structures are comparable to the tilted jets in size and are of much larger scale than the size of mesoscale eddies. Similar to the tilted jets, these large-scale structures can have different tilt angles and propagate with different speeds. In this thesis, we focused on the leading four EOFs, which capture a majority of the variance in the flow field. These four EOFs describe the tilted jets and a purely zonal mode. Similar to the tilted jets, the zonal mode propagates with a constant Rossby wave

phase speed and the propagation speed increases linearly with the slope magnitude and decreases roughly as the square of the meridional wavenumber. We further observe that the relative contributions of the tilted jets and zonal mode are affected by the magnitudes of the slope magnitude and dissipation parameters. The variance explained by the jets (zonal mode) in the full flow field decreases (increases) for steeper slopes and smaller values of eddy viscosity and bottom friction parameters.

In order to understand why the tilted jets and purely zonal modes coexist, we analysed two-dimensional kinetic energy spectra, which showed a presence of nonlinear interactions involving the tilted jets, zonal mode and mesoscale eddies. In fact, the jets lost almost all the energy to the zonal mode when we removed forcing and dissipative terms in the middle of a simulation. This indicates that the zonal mode grows via nonlinear interactions and gains energy from the tilted jets and eddies. In order to confirm the hypothesis, linear stability analysis was performed in the drifting frame of reference around a base state of the time-mean tilted jets. It is found that the eigenmodes present at small wavenumbers are generally stable or weakly unstable; thus, the zonal mode must have received energy through nonlinear interactions in the numerical simulations. These nonlinear interactions are greatly affected by eddy viscosity and bottom friction. For smaller magnitudes of the dissipative parameters, many unstable modes appear, which are otherwise stable. This suggests that strong dissipation tends to suppress small-scales resulting in weaker nonlinear interactions. This somewhat explains the absence of the zonal mode in the numerical solutions that had relatively strong viscous dissipation. However, it is not understood why the system is dominated by purely zonal modes in weak dissipation regimes. Since the zonal modes are aligned with the imposed shear, they cannot gain energy directly from the background shear (see table 4) and must receive energy through nonlinear interactions. It is not yet clear if this is just a coincidence or requirement by the system dynamics.

In the numerical simulations, the zonal mode is present at a lower wavenumber than the wavenumber corresponding to the tilted jets. This shows that eddies are able to transfer energy to meridional scales longer than the Rhines scale, which is set by a balance between Rossby waves and eddy energy (Rhines, 1975). Note that Rossby waves cannot stop the upscale energy transfer (Sukoriansky et al., 2007). Over a flat bottom, the upscale energy transfer stops near the Rhines scale because the triad interactions, which are required to transfer energy to longer wavelengths than the Rhines scale, would involve two almost parallel Fourier modes and such triad interactions are quite inefficient (Vallis and Maltrud, 1993). It is possible that, in the presence of various large-scale structures formed over topography, triad interactions are sufficiently strong to transfer energy to meridional scales longer than the Rhines scale.

7.4 EDDY FLUXES AND JET MAINTENANCE

In general, multiple jets are seen in eastward as well as westward large-scale flows in the oceans, e.g. midlatitude gyre circulations, the Southern Ocean. In chapter 6, we analysed the roles of eddy fluxes in the maintenance of zonal stationary jets in systems forced with either an eastward or a westward uniform vertical shear. Our primary aim is to understand how the Reynolds stress term and form stress term affect the jets in the eastward-sheared (ES) and westward-sheared (WS) cases. Previous studies have shown that non-linear stress terms have opposite effects on baroclinic jets in the two cases (Berloff et al., 2009a,b) and there can be significant differences in the meridional structure and eddy shapes (Berloff and Kamenkovich, 2013a,b). We show that, despite these differences in the local structure, the impacts of eddies on the jets can be understood with the same arguments. The Reynolds stress term forces the jets in both layers and the form stress term transfers momentum from the upper to the lower layer where it is balanced by bottom friction. The roles of the eddy stress terms may look opposite in the ES and WS cases if the jet dynamics is analysed in terms of barotropic and baroclinic modes. This is because the upper (lower) layer is more energetic in the ES (WS) case. As a consequence, the baroclinic flow components are in opposite phases in the two cases and the eddy effects look different.

It is also observed that the energy transfer rates to the jets from eddies via Reynolds stress correlation (RSC) terms are significantly different in the upper and lower layers (also see Thompson and Young, 2007; Ait-Chaalal and Schneider, 2015). This is surprising because, in the numerical simulations, the flow field was predominantly barotropic in both cases and eddy magnitudes were of similar magnitudes in the upper and lower layers. We show that the RSC terms tend to be stronger in the layer having a positive meridional PV gradient and this layer also tends to be the more energetic layer. It is known that stirring by eddies generates Rossby waves that carry energy away from the stirring region and, consequently, eddy momentum converges into the stirring region resulting in the generation of an eastward flow (Dickinson, 1969; Thompson, 1971, 1980). We applied the same argument to the upper and lower layers in the two cases and analysed the direction of eddy momentum transfer. We find that eddy momentum converges into eastward jet regions only for positive meridional PV gradients and this explains the differences in the strength of the layer-wise RSC terms. Note that our approach is qualitative as the layers were treated independent of each other and the presence of the jets was neglected.

7.5 BROADER IMPLICATIONS AND FUTURE DIRECTION

The oceans are primarily driven by surface wind and buoyancy forcing. As a result, the isopycnals in the oceans tilt in the vertical-meridional plane and, consequently, a vertically

sheared velocity field is created governed by thermal wind balance (Vallis, 2017). This vertical shear is generally baroclinically unstable and is the main source of energy for mesoscale eddies. These eddies then transfer energy upscale to form large-scale oceanic flows, e.g. jets.

In this work, we show that tilted jets and zonal background vertical shear can be coupled in the presence of topography and the jets can gain energy directly from the vertical shear. On the other hand, eddy buoyancy fluxes tend to be much stronger in comparison to eddy relative vorticity fluxes over topography and eddies remove more energy from the jets via down-gradient buoyancy transfer than the energy transfer to the jets via Reynolds stresses. In the overall balance, eddies act against the jets. This is opposite to the classical jet formation arguments that eddies force the jets; hence, comes the term “eddy-driven jets”. The results presented in this thesis indicate that, at least in the oceans, mesoscale eddies can either force or oppose the jets depending on the scenario (e.g. see Kamenkovich et al., 2009). Also, alternating jets can be formed via interactions between eddies and different large-scale modes, and this makes the jet dynamics more complex in the oceans. Overall, eddies behave in such a way that jets reach an energy equilibrium state. Thus, with regards to oceanic jets, a term like “eddy-sustained jets” would be more appropriate. We studied the jet dynamics over gentle topographic slopes and this work may not be applicable everywhere in the oceans. This study would be more helpful in understanding the formation of jets in regions where topographic gradients are small.

This general eddy effect may also be important in understanding the dynamics of other large-scale flows in the oceans. For example, topography plays an important role in the Southern Ocean dynamics where eddies have strong control over the strength of the Antarctic Circumpolar Current (ACC) (Hallberg and Gnanadesikan, 2006; Munday et al., 2013). It is seen that eddy activity is significantly enhanced over rough topography and most of the upwelling and particle transport occur over major topographic features (Thompson and Sallée, 2012; Tamsitt et al., 2017). This local increase in eddy activity is seen to be associated with strong topography-mean flow interactions and eddy mixing is also enhanced at ocean mid-depths over topography (Lu and Speer, 2010; Abernathey and Cessi, 2014; Youngs et al., 2017). Although the results of this thesis do not apply directly to such scenarios as we only studied the impacts of mild topographic slopes, strong jet-topography interactions and enhancement in eddy activity were also observed in our idealised baroclinic QG model simulations. Thus, idealised QG experiments could be helpful in studying the effects of topography in the oceans, where the dynamics are complex because of continuous interactions among a wide range of spatiotemporal scales.

Eddies play a major role in the large-scale circulation in the oceans as well as in the atmosphere. Thus, it is crucial to understand how eddies redistribute momentum and buoyancy, which then affect the large-scale flows. In this thesis, we observe that

the strength of eddy buoyancy fluxes is enhanced over topography and the strength of eddy momentum fluxes is closely linked to horizontal PV gradients. Topography also modifies PV gradients; hence, topography can have an indirect effect on eddy momentum fluxes. In this work, we only studied the jet dynamics over mild topographic slopes in the two-layer QG model, which assumes a fixed vertical stratification. Idealised primitive equation model experiments are needed to quantify the topographic effects on eddy fluxes and the large-scale circulation in the oceans. The results can then be compared against outputs from global ocean models and observational datasets. Such studies would shed some light on the impacts of geostrophic eddies on ocean mixing and material transport in the presence of topography. These idealised studies might even be helpful in incorporating topographic impacts in eddy parameterisation schemes, as conventional eddy parameterisation schemes do not account for the topographic effects, which can result in unphysical solutions (Adcock and Marshall, 2000). Finally, the analyses presented in this thesis are based on the Reynolds decomposition of the flow field into the time-mean and eddy components in a non-stationary frame of reference, and in the future it would be useful to consider other decompositions (e.g. Berloff, 2005a), which are more relevant for parameterising the involved eddy effects in non-eddy-resolving or eddy-permitting models.

A

COORDINATE TRANSFORMATION

A.1 GOVERNING EQUATIONS IN A ROTATED NON-STATIONARY FRAME OF REFERENCE

Here, we derive the governing equations for the two-layer QG system in a frame of reference that is moving with a constant velocity and rotated from the zonal direction. For this purpose, we use the governing equations in the original xy coordinate system, which are given as

$$\frac{\partial \Pi_i}{\partial t} = -\frac{\partial \psi_i}{\partial x} \frac{\partial \Pi_i}{\partial y} + \left(\frac{\partial \psi_i}{\partial y} - \delta_{i1} U_b \right) \frac{\partial \Pi_i}{\partial x} + \nu \nabla^4 \psi_i - \delta_{i2} \gamma \nabla^2 \psi_i, \quad (\text{A.1})$$

where

$$\Pi_i = \nabla^2 \psi_i + \epsilon_i S_i (\psi_2 - \psi_1) + (\beta + \epsilon_i S_i U_b) y + \delta_{i2} T_x x. \quad (\text{A.2})$$

Here, $i = 1$ ($i = 2$) indicates the top (bottom) layer, δ_{ij} is the Kronecker delta and $\epsilon_1 = -\epsilon_2 = 1$. The rest of the parameters are the same as in equations (2.1-2.2). The new coordinate system pq is rotated by angle θ and propagating with a constant speed c in q direction (see figure 3.3). It can be shown that

$$\begin{aligned} y &= q \cos \theta + p \sin \theta + ct \cos \theta, \\ x &= -q \sin \theta + p \cos \theta - ct \sin \theta. \end{aligned} \quad (\text{A.3})$$

Using the relations above, the governing equations in pq coordinate system can be written as (note that, in the moving frame of reference $\partial/\partial t \rightarrow \partial/\partial t - c\partial/\partial q$)

$$\begin{aligned} \left[\frac{\partial}{\partial t} - c \frac{\partial}{\partial q} \right] \Pi_i &= - \left(\frac{\partial \psi_i}{\partial p} - \delta_{i1} U_b \sin \theta \right) \frac{\partial \Pi_i}{\partial q} + \left(\frac{\partial \psi_i}{\partial q} - \delta_{i1} U_b \cos \theta \right) \frac{\partial \Pi_i}{\partial p} \\ &\quad + \nu \nabla^4 \psi_i - \delta_{i2} \gamma \nabla^2 \psi_i, \end{aligned} \quad (\text{A.4})$$

where

$$\left. \begin{aligned} \Pi_1 &= \overbrace{\nabla^2 \psi_1 + S_1(\psi_2 - \psi_1)}^{Q_1} + (\beta + S_1 U_b)(q \cos \theta + p \sin \theta + ct \cos \theta), \\ \Pi_2 &= \overbrace{\nabla^2 \psi_2 + S_2(\psi_1 - \psi_2)}^{Q_2} + (\beta - S_2 U_b)(q \cos \theta + p \sin \theta + ct \cos \theta) \\ &\quad + T_x(-q \sin \theta + p \cos \theta - ct \sin \theta). \end{aligned} \right\} \quad (\text{A.5})$$

The variables are a function of (p, q, t) . Equation (A.4) can be further expanded as

$$\begin{aligned} \frac{\partial Q_i}{\partial t} &= -\frac{\partial \psi_i}{\partial p} \frac{\partial Q_i}{\partial q} + \frac{\partial \psi_i}{\partial q} \frac{\partial Q_i}{\partial p} + (\delta_{i1} U_b \sin \theta + c) \frac{\partial Q_i}{\partial q} - \delta_{i1} U_b \cos \theta \frac{\partial Q_i}{\partial p} \\ &\quad - [(\beta + \epsilon_i S_i U_b) \cos \theta - \delta_{i2} T_x \sin \theta] \frac{\partial \psi_i}{\partial p} + [(\beta + \epsilon_i S_i U_b) \sin \theta + \delta_{i2} T_x \cos \theta] \frac{\partial \psi_i}{\partial q} \\ &\quad + \nu \nabla^4 \psi_i - \delta_{i2} \gamma \nabla^2 \psi_i. \end{aligned} \quad (\text{A.6})$$

A.2 PV BUDGET IN THE STATISTICAL EQUILIBRIUM

In order to analyse the role of eddies in potential vorticity (PV) balances, we isolate the contributions of the mean flow and eddies by decomposing the variables into the time-mean $(\bar{Q}_i, \bar{\psi}_i)$ and eddy components (Q'_i, ψ'_i) in equation (A.6),

$$\begin{aligned} \left[\frac{\partial}{\partial t} - c \frac{\partial}{\partial q} \right] (\bar{Q}_1 + Q'_1) &= - \left(\frac{\partial(\bar{\psi}_1 + \psi'_1)}{\partial p} - U_b \sin \theta \right) \left(\frac{\partial(\bar{Q}_1 + Q'_1)}{\partial q} + (\beta + S_1 U_b) \cos \theta \right) \\ &\quad + \left(\frac{\partial(\bar{\psi}_1 + \psi'_1)}{\partial q} - U_b \cos \theta \right) \left(\frac{\partial(\bar{Q}_1 + Q'_1)}{\partial p} + (\beta + S_1 U_b) \sin \theta \right) + \nu \nabla^4 (\bar{\psi}_1 + \psi'_1), \end{aligned} \quad (\text{A.7})$$

$$\begin{aligned} \left[\frac{\partial}{\partial t} - c \frac{\partial}{\partial q} \right] (\bar{Q}_2 + Q'_2) &= - \frac{\partial(\bar{\psi}_2 + \psi'_2)}{\partial p} \left(\frac{\partial(\bar{Q}_2 + Q'_2)}{\partial q} + (\beta - S_2 U_b) \cos \theta - T_x \sin \theta \right) \\ &\quad + \frac{\partial(\bar{\psi}_2 + \psi'_2)}{\partial q} \left(\frac{\partial(\bar{Q}_2 + Q'_2)}{\partial p} + (\beta - S_2 U_b) \sin \theta + T_x \cos \theta \right) \\ &\quad + \nu \nabla^4 (\bar{\psi}_2 + \psi'_2) - \gamma \nabla^2 (\bar{\psi}_2 + \psi'_2). \end{aligned} \quad (\text{A.8})$$

We then average the above equations over time to derive the time-mean equations. Note that $\bar{Q}'_i = \bar{\psi}'_i = 0$ and $\frac{\partial \bar{Q}_i}{\partial p} = \frac{\partial \bar{\psi}_i}{\partial p} = 0$ (the time-mean profile of the jets is a function of q only),

$$\frac{\partial \bar{Q}_1}{\partial t} - c \frac{\partial \bar{Q}_1}{\partial q} = - \frac{\partial \bar{\psi}'_1}{\partial p} \frac{\partial \bar{Q}'_1}{\partial q} + U_b \sin \theta \frac{\partial \bar{Q}_1}{\partial q} + \frac{\partial \bar{\psi}'_1}{\partial q} \frac{\partial \bar{Q}'_1}{\partial p} + (\beta + S_1 U_b) \sin \theta \frac{\partial \bar{\psi}_1}{\partial q} + \nu \nabla^4 \bar{\psi}_1, \quad (\text{A.9})$$

$$\frac{\partial \bar{Q}_2}{\partial t} - c \frac{\partial \bar{Q}_2}{\partial q} = - \overline{\frac{\partial \psi'_2}{\partial p} \frac{\partial Q'_2}{\partial q}} + \overline{\frac{\partial \psi'_2}{\partial q} \frac{\partial Q'_2}{\partial p}} + (\beta - S_2 U_b) \sin \theta + T_x \cos \theta \frac{\partial \bar{\psi}_2}{\partial q} + \nu \nabla^4 \bar{\psi}_2 - \gamma \nabla^2 \bar{\psi}_2. \quad (\text{A.10})$$

The time-derivative terms vanish in the equilibrium and we have only retained them here for clarity. We further introduce velocity ($\mathbf{u}_i = (u_i, v_i) = (-\partial \psi_i / \partial q, \partial \psi_i / \partial p)$) and relative vorticity ($\zeta_i = \nabla^2 \psi_i$, where $\nabla = (\partial / \partial p, \partial / \partial q)$) to represent the nonlinear terms in the flux form ($\nabla \cdot \mathbf{u}'_i = 0$ from the continuity equation). The final time-mean equations are

$$\frac{\partial \bar{Q}_1}{\partial t} = -\nabla \cdot \overline{(\mathbf{u}'_1 Q'_1)} + (c + U_b \sin \theta) \frac{\partial \bar{Q}_1}{\partial q} - (\beta + S_1 U_b) \sin \theta \cdot \bar{u}_1 + \nu \nabla^2 \bar{\zeta}_1, \quad (\text{A.11})$$

$$\frac{\partial \bar{Q}_2}{\partial t} = -\nabla \cdot \overline{(\mathbf{u}'_2 Q'_2)} + c \frac{\partial \bar{Q}_2}{\partial q} - [(\beta - S_2 U_b) \sin \theta + T_x \cos \theta] \cdot \bar{u}_2 + \nu \nabla^2 \bar{\zeta}_2 - \gamma \bar{\zeta}_2. \quad (\text{A.12})$$

A.3 ENERGETICS DERIVATION

In order to derive energy equations, we multiply equation (A.6) by $-H_i \psi_i$ and add the layer-wise equations. We first look at the time-derivative term (note that $H_1 S_1 = H_2 S_2$),

$$\begin{aligned} &\Rightarrow \sum_{i=1}^2 -H_i \psi_i \frac{\partial}{\partial t} [\nabla^2 \psi_i + \epsilon_i S_i (\psi_2 - \psi_1)] \\ &\Rightarrow \sum_{i=1}^2 H_i \left[-\frac{\partial}{\partial t} (\nabla \cdot (\psi_i \nabla \psi_i)) + \frac{\partial}{\partial t} |\nabla \psi_i|^2 + \nabla^2 \psi_i \frac{\partial \psi_i}{\partial t} + \frac{S_i}{2} \frac{\partial \psi_i^2}{\partial t} \right] \\ &\quad - H_1 S_1 \psi_1 \frac{\partial \psi_2}{\partial t} - H_2 S_2 \psi_2 \frac{\partial \psi_1}{\partial t} \\ &\Rightarrow \sum_{i=1}^2 H_i \left[-\frac{\partial}{\partial t} (\nabla \cdot (\psi_i \nabla \psi_i)) + \frac{1}{2} \frac{\partial}{\partial t} |\nabla \psi_i|^2 + \nabla \cdot (\nabla \psi_i \frac{\partial \psi_i}{\partial t}) + \frac{S_i}{2} \frac{\partial \psi_i^2}{\partial t} \right] \\ &\quad - H_1 S_1 \psi_1 \frac{\partial \psi_2}{\partial t} - H_2 S_2 \psi_2 \frac{\partial \psi_1}{\partial t} \\ &\Rightarrow \frac{\partial}{\partial t} \left[\underbrace{\sum_{i=1}^2 \frac{H_i}{2} |\nabla \psi_i|^2}_{KE} + \underbrace{\frac{H_1 S_1}{2} (\psi_1 - \psi_2)^2}_{PE} \right] + \sum_{i=1}^2 H_i \nabla \cdot \left[-\frac{\partial}{\partial t} (\psi_i \nabla \psi_i) + \nabla \psi_i \frac{\partial \psi_i}{\partial t} \right]. \end{aligned} \quad (\text{A.13})$$

In a similar manner, we manipulate the nonlinear terms. These are first written in the flux form by using the condition $\nabla \cdot \mathbf{u}_i = 0$,

$$\begin{aligned}
&\Rightarrow \sum_{i=1}^2 -H_i \psi_i \left[-\frac{\partial \psi_i}{\partial p} \frac{\partial Q_i}{\partial q} + \frac{\partial \psi_i}{\partial q} \frac{\partial Q_i}{\partial p} \right] = \sum_{i=1}^2 H_i \psi_i \nabla \cdot (\mathbf{u}_i Q_i) \\
&\Rightarrow \sum_{i=1}^2 H_i \left[\nabla \cdot (\psi_i \mathbf{u}_i Q_i) - \cancel{(\nabla \psi_i \cdot \mathbf{u}_i) Q_i}^0 \right] = \sum_{i=1}^2 H_i \nabla \cdot (\psi_i \mathbf{u}_i Q_i). \quad (\text{A.14})
\end{aligned}$$

We now work with the linear terms. We manipulate the terms having ψ_i and Q_i separately and then add them at the end,

$$\begin{aligned}
&\Rightarrow -H_1 \psi_1 \left[(\beta + S_1 U_b) \left(-\cos \theta \frac{\partial \psi_1}{\partial p} + \sin \theta \frac{\partial \psi_1}{\partial q} \right) \right] \\
&\quad -H_2 \psi_2 \left[-[(\beta - S_2 U_b) \cos \theta - T_x \sin \theta] \frac{\partial \psi_2}{\partial p} + [(\beta - S_2 U_b) \sin \theta + T_x \cos \theta] \frac{\partial \psi_2}{\partial q} \right] \\
&\Rightarrow \frac{H_1(\beta + S_1 U_b)}{2} \left(\cos \theta \frac{\partial \psi_1^2}{\partial p} - \sin \theta \frac{\partial \psi_1^2}{\partial q} \right) \\
&\quad + \frac{H_2}{2} \left[[(\beta - S_2 U_b) \cos \theta - T_x \sin \theta] \frac{\partial \psi_2^2}{\partial p} - [(\beta - S_2 U_b) \sin \theta + T_x \cos \theta] \frac{\partial \psi_2^2}{\partial q} \right]. \quad (\text{A.15})
\end{aligned}$$

We also have,

$$\begin{aligned}
&\Rightarrow -H_1 \psi_1 \left[(U_b \sin \theta + c) \frac{\partial Q_1}{\partial q} - U_b \cos \theta \frac{\partial Q_1}{\partial p} \right] - H_2 \psi_2 c \frac{\partial Q_2}{\partial q} \\
&\Rightarrow -H_1 \psi_1 \left[(U_b \sin \theta + c) \frac{\partial}{\partial q} (\nabla^2 \psi_1 + S_1(\psi_2 - \psi_1)) - U_b \cos \theta \frac{\partial}{\partial p} (\nabla^2 \psi_1 + S_1(\psi_2 - \psi_1)) \right] \\
&\quad - H_2 \psi_2 c \frac{\partial}{\partial q} (\nabla^2 \psi_2 + S_2(\psi_1 - \psi_2)) \\
&\Rightarrow -H_1 (U_b \sin \theta + c) \left[\frac{\partial}{\partial q} (\nabla \cdot (\psi_1 \nabla \psi_1)) - \nabla \cdot \left(\frac{\partial \psi_1}{\partial q} \nabla \psi_1 \right) - \frac{1}{2} \frac{\partial}{\partial q} |\nabla \psi_1|^2 \right] \\
&\quad + H_1 U_b \cos \theta \left[\frac{\partial}{\partial p} (\nabla \cdot (\psi_1 \nabla \psi_1)) - \nabla \cdot \left(\frac{\partial \psi_1}{\partial p} \nabla \psi_1 \right) - \frac{1}{2} \frac{\partial}{\partial p} |\nabla \psi_1|^2 \right] \\
&\quad - H_2 c \left[\frac{\partial}{\partial q} (\nabla \cdot (\psi_2 \nabla \psi_2)) - \nabla \cdot \left(\frac{\partial \psi_2}{\partial q} \nabla \psi_2 \right) - \frac{1}{2} \frac{\partial}{\partial q} |\nabla \psi_2|^2 \right] \\
&\quad - H_1 S_1 (U_b \sin \theta + c) \left(\psi_1 \frac{\partial \psi_2}{\partial q} - \frac{1}{2} \frac{\partial \psi_1^2}{\partial q} \right) + H_1 S_1 U_b \cos \theta \left(\psi_1 \frac{\partial \psi_2}{\partial p} - \frac{1}{2} \frac{\partial \psi_1^2}{\partial p} \right) \\
&\quad - H_2 S_2 c \left(\psi_2 \frac{\partial \psi_1}{\partial q} - \frac{1}{2} \frac{\partial \psi_2^2}{\partial q} \right). \quad (\text{A.16})
\end{aligned}$$

We can now add equations (A.15-A.16) and some of the terms cancel out.

$$\begin{aligned}
\Rightarrow & \sum_{i=1}^2 H_i \left[\left(k_{i1} \frac{\partial}{\partial p} + k_{i2} \frac{\partial}{\partial q} \right) \psi_i^2 \right] + \frac{c}{2} \frac{\partial}{\partial q} (H_1 |\nabla \psi_1|^2 + H_2 |\nabla \psi_2|^2 + H_1 S_1 (\psi_1 - \psi_2)^2) \\
& \sum_{i=1}^2 l_i \left[\frac{\partial}{\partial q} (\nabla \cdot (\psi_i \nabla \psi_i)) - \nabla \cdot \left(\frac{\partial \psi_i}{\partial q} \nabla \psi_i \right) \right] \\
& + H_1 U_b \cos \theta \left[\frac{\partial}{\partial p} (\nabla \cdot (\psi_1 \nabla \psi_1)) - \nabla \cdot \left(\frac{\partial \psi_1}{\partial p} \nabla \psi_1 \right) \right] \\
& + H_1 U_b \left(-\cos \theta \frac{\partial}{\partial p} + \sin \theta \frac{\partial}{\partial q} \right) |\nabla \psi_1|^2 + H_1 S_1 U_b \left(\cos \theta \psi_1 \frac{\partial \psi_2}{\partial p} - \sin \theta \psi_1 \frac{\partial \psi_2}{\partial q} \right),
\end{aligned} \tag{A.17}$$

where

$$\left. \begin{aligned}
k_{11} &= \frac{H_1}{2} \beta \cos \theta, k_{12} = -\frac{H_1}{2} \beta \sin \theta \\
k_{21} &= \frac{H_2}{2} [(\beta - S_2 U_b) \cos \theta - T_x \sin \theta], k_{22} = -\frac{H_1}{2} [(\beta - S_2 U_b) \sin \theta + T_x \cos \theta] \\
l_1 &= -H_1 (U_b \sin \theta + c), l_2 = -H_2 c
\end{aligned} \right\} \tag{A.18}$$

In equation (A.17), except for the last term, all terms can be represented in the flux form, i.e. $(\nabla \cdot \mathcal{B})$. This means that the integrals of these terms over the whole domain vanish in our system due to the imposed periodic boundary conditions as there is no flux input/output from the boundaries.

Finally, the dissipation terms are worked out below,

$$\begin{aligned}
\Rightarrow & -\nu \sum_{i=1}^2 H_i \psi_i \nabla^4 \psi_i + \gamma H_2 \psi_2 \nabla^2 \psi_2 \\
\Rightarrow & -\nu \sum_{i=1}^2 H_i [\nabla \cdot (\psi_i \nabla \zeta_i) - \nabla \psi_i \cdot \nabla \zeta_i] + \gamma H_2 [\nabla \cdot (\psi_2 \nabla \psi_2) - |\nabla \psi_2|^2] \\
\Rightarrow & \nu \sum_{i=1}^2 H_i [-\nabla \cdot (\psi_i \nabla \zeta_i) + \nabla \cdot (\zeta_i \nabla \psi_i) - \zeta_i^2] + \gamma H_2 [\nabla \cdot (\psi_2 \nabla \psi_2) - |\nabla \psi_2|^2],
\end{aligned} \tag{A.19}$$

where $\zeta_i = \nabla^2 \psi_i$ is the relative vorticity. The relation above shows that the system loses energy through viscous dissipation and bottom friction.

A.3.1 ENERGY BUDGETS OF THE MEAN FLOW AND EDDIES

We now add expressions (A.13-A.19) to analyse the energy budget of the two-layer QG system. We further integrate the energy equation over the whole domain and average in

time,

$$\begin{aligned} \int_A \frac{\partial}{\partial t} (\overline{KE} + \overline{PE}) &= - \int_A \overline{\nabla \cdot \mathcal{B}}^0 + \int_A H_1 S_1 U_b \left(\cos \theta \overline{\psi_1 \frac{\partial \psi_2}{\partial p}} - \sin \theta \overline{\psi_1 \frac{\partial \psi_2}{\partial q}} \right) \\ &\quad - \int_A \nu \sum_{i=1}^2 H_i \overline{|\zeta_i|^2} - \int_A \gamma H_2 \overline{|\nabla \psi_2|^2}, \end{aligned} \quad (\text{A.20})$$

where

$$KE = \sum_{i=1}^2 \frac{H_i}{2} |\nabla \psi_i|^2, PE = \frac{H_1 S_1}{2} (\psi_1 - \psi_2)^2 \quad (\text{A.21})$$

All terms that can be represented in the flux form are contained in $\nabla \cdot \mathcal{B}$ and these terms vanish in the domain integrated energy equation. Thus, in the absence of forcing and dissipation and terms, i.e. $U_b = \nu = \gamma = 0$, the total energy of the system is conserved.

In addition to the total energy budget, we also derive energy budgets of the mean flow and eddies. This is helpful in analysing the energy exchanges between the large-scale flow and transient eddy field components. Also, the energy gain by the mean flow and eddies directly from the imposed background vertical shear can be computed. We first decompose the full field into the time-mean ($\overline{\psi}_i, \overline{Q}_i$) and transient eddy field (ψ'_i, Q'_i). Note that $\psi_i = \overline{\psi}_i + \psi'_i$, $Q = \overline{Q}_i + Q'_i$ and $\overline{\psi}'_i = \overline{Q}'_i = 0$.

In order to derive the energy equation for the mean flow, we multiply the equation (A.6) by $-H_i \overline{\psi}_i$ and follow the same steps shown above. The final equation integrated over the whole domain and averaged in time is (domain integrals of the divergence terms, i.e. $\int_A \nabla \cdot \mathcal{B}$ vanish and are not shown),

$$\begin{aligned} \int_A \frac{\partial}{\partial t} (\overline{KE}_m + \overline{PE}_m) &= - \int_A \sum_{i=1}^2 H_i \overline{Q}_i \mathbf{u}_i \cdot \nabla \overline{\psi}_i + \int_A H_1 S_1 U_b \left(\underbrace{\cos \theta \overline{\psi_1 \frac{\partial \overline{\psi}_2}{\partial p}}}_{=0} - \sin \theta \overline{\psi_1 \frac{\partial \overline{\psi}_2}{\partial q}} \right) \\ &\quad - \int_A \nu \sum_{i=1}^2 H_i \overline{|\zeta_i|^2} - \int_A \gamma H_2 \overline{|\nabla \overline{\psi}_2|^2}, \end{aligned} \quad (\text{A.22})$$

where

$$KE_m = \sum_{i=1}^2 \frac{H_i}{2} |\nabla \overline{\psi}_i|^2, PE_m = \frac{H_1 S_1}{2} (\overline{\psi}_1 - \overline{\psi}_2)^2. \quad (\text{A.23})$$

The second term on the right-hand side (RHS) in the above equation indicates that tilted jets can gain energy directly from the background flow as $\sin \theta$ is nonzero. The first term on the RHS (contribution from the Jacobian term in the original PV equation) does not vanish here and it represents the energy exchange between the jets and eddies.

The rest of the terms on the RHS represent the energy loss from the mean flow through viscous dissipation and bottom friction.

Similarly, an equation for eddy energy can be derived by multiplying the equation (A.6) by $-H_i\psi'_i$ and integrating over the whole domain as well as averaging in time,

$$\begin{aligned} \int_A \frac{\partial}{\partial t} (\overline{KE}_e + \overline{PE}_e) &= - \int_A \sum_{i=1}^2 H_i \overline{Q_i \mathbf{u}_i \cdot \nabla \psi'_i} + \int_A H_1 S_1 U_b \left(\cos \theta \overline{\psi'_1 \frac{\partial \psi'_2}{\partial p}} - \sin \theta \overline{\psi'_1 \frac{\partial \psi'_2}{\partial q}} \right) \\ &\quad - \int_A \nu \sum_{i=1}^2 H_i \overline{|\zeta'_i|^2} - \int_A \gamma H_2 \overline{|\nabla \psi'_2|^2}, \end{aligned} \quad (\text{A.24})$$

where

$$KE_e = \sum_{i=1}^2 \frac{H_i}{2} \overline{|\nabla \psi'_i|^2}, PE_e = \frac{H_1 S_1}{2} (\overline{\psi'_1} - \overline{\psi'_2})^2. \quad (\text{A.25})$$

The first and second terms on the RHS represent the eddy-jet energy exchange and eddy energy gain from the background available potential energy, respectively. The energy gain by eddies from jets through jet-eddy interactions is energy loss for the mean jets. Thus, the first terms on the RHS in equations (A.22,A.24) are equal in magnitude but are opposite in the sign. This can easily be shown as,

$$\begin{aligned} \int_A \overline{Q_i \mathbf{u}_i \cdot \nabla \psi'_i} &= \int_A \overline{Q_i \mathbf{u}_i \cdot \nabla (\psi_i - \overline{\psi}_i)} \\ &= \int_A \overline{Q_i \mathbf{u}_i \cdot \nabla \psi_i} - \int_A \overline{Q_i \mathbf{u}_i \cdot \nabla \overline{\psi}_i} \\ &= \int_A \overline{Q_i [\nabla \cdot (\mathbf{u}_i \psi_i) - \psi_i \nabla \cdot \mathbf{u}_i]} \xrightarrow{0} - \int_A \overline{Q_i \mathbf{u}_i \cdot \nabla \overline{\psi}_i} \end{aligned} \quad (\text{A.26})$$

The first terms on the RHS in equations (A.22,A.24) can be further simplified to

$$\begin{aligned} \overline{Q_i \mathbf{u}_i \cdot \nabla \psi'_i} &= \overline{Q'_i \mathbf{u}'_i \cdot \nabla \psi'_i} \\ \overline{Q_i \mathbf{u}_i \cdot \nabla \overline{\psi}_i} &= \overline{Q'_i \mathbf{u}'_i \cdot \nabla \overline{\psi}_i} \end{aligned} \quad (\text{A.27})$$

A.4 LINEARISATION OF THE GOVERNING EQUATIONS

We linearise the governing equation (A.6) around the time-mean state of the tilted, drifting jets. In this scenario, the time-mean flow is a function of q only, i.e., $\overline{\psi}_i = f(q)$ and $\partial \overline{\psi}_i / \partial p = 0$ and satisfies the governing equation; hence, we have

$$\begin{aligned} -(c + \delta_{i1} U_b \sin \theta) \frac{\partial}{\partial q} [\nabla^2 \overline{\psi}_i + \epsilon_i S_i (\overline{\psi}_2 - \overline{\psi}_1)] &- [(\beta + \epsilon_i S_i U_b) \sin \theta + \delta_{i2} T_x \cos \theta] \frac{\partial \overline{\psi}_i}{\partial q} \\ &= \nu \nabla^4 \overline{\psi}_i - \delta_{i2} \gamma \nabla^2 \overline{\psi}_i. \end{aligned} \quad (\text{A.28})$$

In order to derive the linearised equations, we then substitute $\psi_i = \bar{\psi}_i(q) + \psi'_i$ in equation (A.6) and ignore the non-linear terms. We further use the relation (A.28) and the final linearised equation is

$$\begin{aligned} & \left[\frac{\partial}{\partial t} - c \frac{\partial}{\partial q} \right] [\nabla^2 \psi'_i + \epsilon_i S_i (\psi'_2 - \psi'_1)] + \frac{\partial \psi'_i}{\partial p} \frac{\partial}{\partial q} [\nabla^2 \bar{\psi}_i + \epsilon_i S_i (\bar{\psi}_2 - \bar{\psi}_1)] \\ & + [(\beta + \epsilon_i S_i U_b) \cos \theta - \delta_{i2} T_x \sin \theta] \frac{\partial \psi'_i}{\partial p} - \frac{\partial \bar{\psi}_i}{\partial q} \frac{\partial}{\partial p} [\nabla^2 \psi'_i + \epsilon_i S_i (\psi'_2 - \psi'_1)] \\ & \quad - [(\beta + \epsilon_i S_i U_b) \sin \theta + \delta_{i2} T_x \cos \theta] \sin \theta \frac{\partial \psi'_i}{\partial q} \\ & + \delta_{i1} U_b \left(-\sin \theta \frac{\partial}{\partial q} + \cos \theta \frac{\partial}{\partial p} \right) [\nabla^2 \psi'_i + \epsilon_i S_i (\psi'_2 - \psi'_1)] \\ & = \nu \nabla^4 \psi'_i - \delta_{i2} \gamma \nabla^2 \bar{\psi}_i. \end{aligned} \quad (\text{A.29})$$

Let $\partial \bar{\psi}_i / \partial q = -\bar{u}_i$, which is the along-jet mean velocity. The linearised equation can be written as

$$\begin{aligned} \frac{\partial}{\partial t} [\nabla^2 \psi'_i + \epsilon_i S_i (\psi'_2 - \psi'_1)] & + \left[A_i \frac{\partial}{\partial p} + B_i \frac{\partial}{\partial q} \right] [\nabla^2 \psi'_i + \epsilon_i S_i (\psi'_2 - \psi'_1)] \\ & + C_i \frac{\partial \psi'_i}{\partial p} + D_i \frac{\partial \psi'_i}{\partial q} = \nu \nabla^4 \psi'_i - \delta_{i2} \gamma \nabla^2 \psi'_i, \end{aligned} \quad (\text{A.30})$$

where

$$\left. \begin{aligned} A_1 &= U_b \cos \theta + \bar{u}_1, \\ A_2 &= \bar{u}_2, \\ B_1 &= -c - U_b \sin \theta, \\ B_2 &= -c, \\ C_1 &= (\beta + S_1 U_b) \cos \theta - \bar{u}_1'' + S_1 (\bar{u}_1 - \bar{u}_2), \\ C_2 &= (\beta - S_2 U_b) \cos \theta - T_x \sin \theta - \bar{u}_2'' + S_2 (\bar{u}_2 - \bar{u}_1), \\ D_1 &= -(\beta + S_1 U_b) \sin \theta, \\ D_2 &= -(\beta - S_2 U_b) \sin \theta - T_x \cos \theta. \end{aligned} \right\} \quad (\text{A.31})$$

For the linear stability analysis, we assume solutions of the kind $\psi'_i = \tilde{\psi}_i(q) e^{i(lp - \omega t)}$ for the perturbation terms, where l is the wavenumber along p direction, and ω is the frequency.

$$\begin{aligned} -i\omega \left[-l^2 \tilde{\psi}_i + \tilde{\psi}_i'' + \epsilon_i S_i (\tilde{\psi}_2 - \tilde{\psi}_1) \right] & + \left[A_i \frac{\partial}{\partial p} + B_i \frac{\partial}{\partial q} \right] \left[-l^2 \tilde{\psi}_i + \tilde{\psi}_i'' + \epsilon_i S_i (\tilde{\psi}_2 - \tilde{\psi}_1) \right] \\ & + ilC_i \tilde{\psi}_i + D_i \tilde{\psi}_i' = \nu (l^4 \tilde{\psi}_i + \tilde{\psi}_i''') + \delta_{i2} \gamma (l^2 \tilde{\psi}_i + \tilde{\psi}_i''). \end{aligned} \quad (\text{A.32})$$

We then use finite-difference discretisation in direction q to solve the above equations. This results in a system of equations, which can be represented in a matrix form as

$$\omega \mathbf{G} \tilde{\psi} = \mathbf{H} \tilde{\psi}, \quad (\text{A.33})$$

$$|\mathbf{G}^{-1} \mathbf{H} - \omega \mathbf{I}| = \mathbf{0}. \quad (\text{A.34})$$

Here, \mathbf{G} and \mathbf{H} represent the coefficient matrices, and $\tilde{\psi}$ is the set of all eigenvectors. We then impose periodic boundary conditions at both ends and solve the eigenvalue problem for all possible values of the wavenumber l .

B

JETS IN CHANNEL SIMULATIONS

B.1 JET TILT AND DRIFT IN A CHANNEL SIMULATION

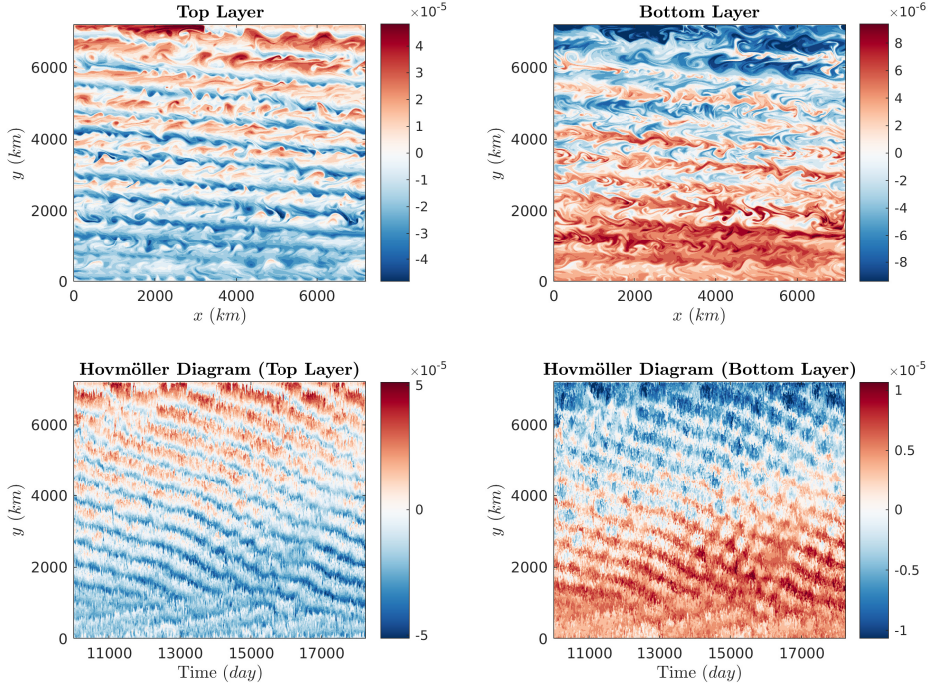


Figure B.1: Adopted from Khatri and Berloff (2018a). Tilted, drifting jets in a channel simulation; (a,b): Snapshots of the PV anomaly field in the top layer ($\nabla^2\psi_1 + S_1(\psi_2 - \psi_1)$) and bottom layer ($\nabla^2\psi_2 + S_2(\psi_1 - \psi_2)$) for the medium-slope configuration (colorbar units are in s^{-1}); (c,d): Hovmöller diagrams of the PV anomaly field in both layers (PV along a meridional cross-section is plotted against time). $\nu = 50 \text{ m}^2\text{s}^{-1}$ and $\gamma = 10^{-8} \text{ s}^{-1}$ were used in the simulation. The rest of the parameter values were the same as in table 2.1.

In order to verify that jets tilt and drift over a sloped topography irrespective of the boundary conditions, we ran channel simulations. We imposed partial-slip boundary

conditions on the meridional boundaries,

$$\frac{\partial^2 \psi_i}{\partial \mathbf{n}^2} - \frac{1}{\alpha} \frac{\partial \psi_i}{\partial \mathbf{n}} = 0, \quad (\text{B.1})$$

where ψ_i is the layer-wise velocity streamfunction and $\alpha = 120$ km. \mathbf{n} is the unit vector, which is normal-to-wall and faces inward. This condition is imposed to parameterise dynamically unresolved near-boundary processes (Berloff and McWilliams, 1999). Along with this boundary condition, we also ensured no normal flow on the meridional boundaries. In this simulation, we used a larger 7200 km square domain with 2048×2049 grid points to verify that the tendency of the jets to tilt and drift does not depend on the domain size and grid resolution; however, the tilt angle and drift speed might differ due to boundary effects. In the simulation, we used $\nu = 50 \text{ m}^2 \text{s}^{-1}$ and $\gamma = 10^{-8} \text{ s}^{-1}$, and the rest of the parameters were the same as given in table 2.1. As seen in figure B.1, the jets tilt from the zonal direction (tilt angle $\sim 5^\circ$) and drift meridionally with a speed of about 0.2 cm s^{-1} . The jet dynamics are more complex than in the doubly-periodic simulations. The drifting jets transport PV in the north-south direction and this results in the accumulation of positive or negative PV anomalies near the boundaries. Further, a secondary circulation develops that transports PV along the boundaries (not shown) and, as a result, the domain integrated PV remains conserved. These secondary circulations may be important around continental boundaries; however, impacts of these circulations are not studied in this thesis.

B.2 J AND Z MODES IN A CHANNEL SIMULATION

Similar to the doubly-periodic simulations, EOF analysis was performed on the streamfunction field in a channel simulation to confirm the presence of the J and Z modes (figure B.2). The spatial flow structure is quite complicated due to the presence of the meridional boundaries; nevertheless, the tilted J and purely zonal Z modes are visible, especially in the northern and southern halves of the domain. Here, the J and Z modes propagate southwards and northwards, respectively (see Hovmöller plots in figure B.2), and the power spectra of the PCs corresponding to these modes show distinct peaks in the frequency space indicating the propagation with roughly constant speeds.

B.3 EOFs IN DOUBLY-PERIODIC SIMULATIONS

In chapter 5, we only discussed the first four EOFs, which capture the J and Z modes. Here, we show the first twenty EOFs (figure B.3) obtained from the EOF analysis corresponding to the simulation in figure 5.1. In addition to the J and Z modes, higher EOFs also have a large-scale structure and are present at lower wavenumbers than mesoscale eddies. Most of these EOFs appear in pairs and this indicates that they propagate.

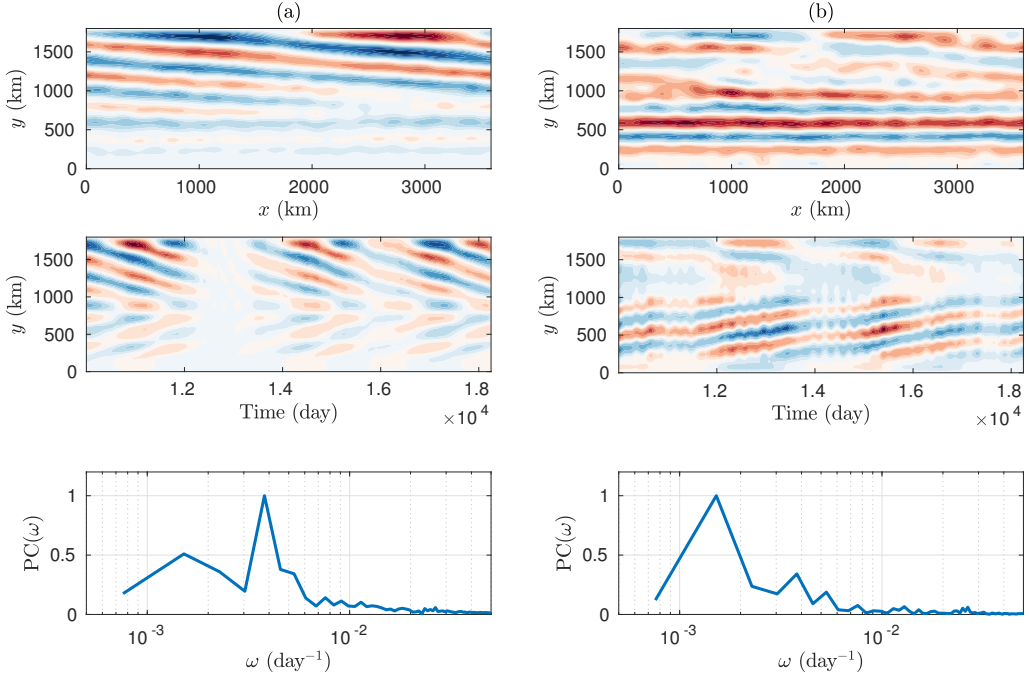


Figure B.2: The leading EOFs of the streamfunction field in a channel simulation; (a) EOF1 (b) EOF3. The upper-layer spatial structure of the EOFs is shown in the top panels and the Hovmöller diagrams of the J and Z modes reconstructed using the EOFs and their PCs are shown in the middle panels. The J and Z modes together capture about 60% of the variance. The colorbar range is [-1,1], blue to red. The power spectra of PCs (normalised to unity) corresponding to the EOFs are shown in the bottom panels.

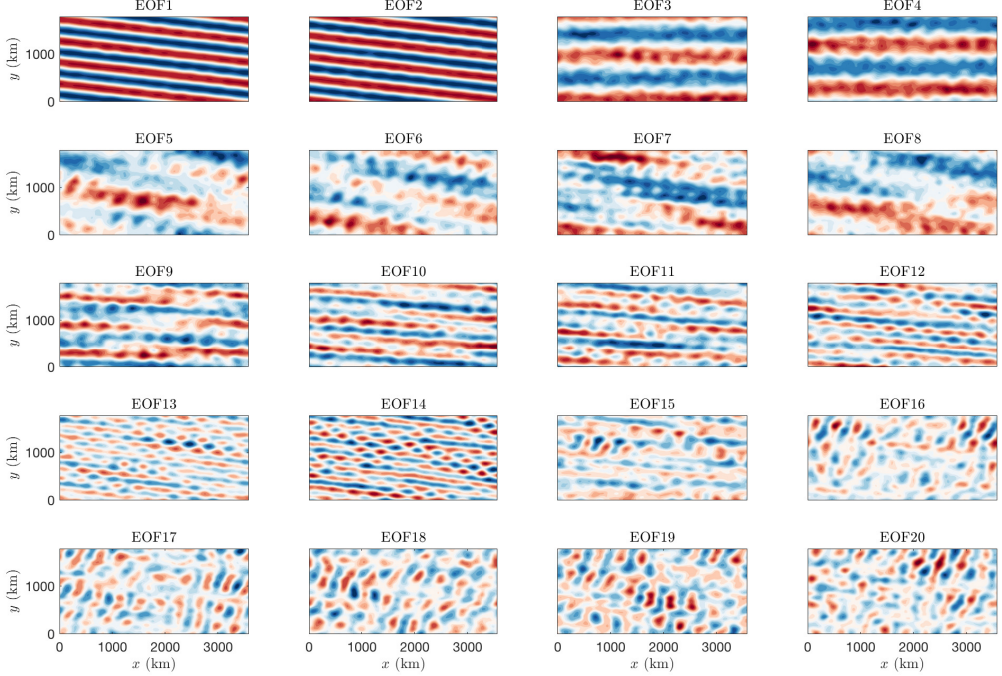


Figure B.3: The first twenty EOFs of the streamfunction field in the doubly-periodic simulation corresponding to figure 5.1. The panels show the spatial structure of the EOFs in the top layer. The colorbar range is [-1,1], blue to red. The first twenty EOFs capture more than 90% of the variance.

C

COPYRIGHT PERMISSIONS

CAMBRIDGE UNIVERSITY PRESS LICENSE TERMS AND CONDITIONS

Feb 18, 2019

This Agreement between Mr. Hemant Khatri ("You") and Cambridge University Press ("Cambridge University Press") consists of your license details and the terms and conditions provided by Cambridge University Press and Copyright Clearance Center.

License Number	4532001468682
License date	Feb 18, 2019
Licensed Content Publisher	Cambridge University Press
Licensed Content Publication	The Journal of Fluid Mechanics
Licensed Content Title	A mechanism for jet drift over topography
Licensed Content Author	Hemant Khatri, Pavel Berloff
Licensed Content Date	Apr 26, 2018
Licensed Content Volume	845
Licensed Content Issue	undefined
Start page	392
End page	416
Type of Use	Dissertation/Thesis
Requestor type	Author
Portion	Full article
Author of this Cambridge University Press article	Yes
Author / editor of the new work	Yes
Order reference number	
Territory for reuse	World
Title of your thesis / dissertation	Dynamics of ocean jets over topography
Expected completion date	Aug 2019
Estimated size(pages)	100
Requestor Location	Mr. Hemant Khatri 613, Huxley, Imperial College London South Kensington London, London SW7 2AZ United Kingdom Attn: Mr. Hemant Khatri
Publisher Tax ID	GB823847609
Billing Type	Invoice
Billing Address	Mr. Hemant Khatri 613, Huxley, Imperial College London

South Kensington
London, United Kingdom SW7 2AZ
Attn: Mr. Hemant Khatri

Total **0.00 GBP**

[Terms and Conditions](#)

TERMS & CONDITIONS

Cambridge University Press grants the Licensee permission on a non-exclusive non-transferable basis to reproduce, make available or otherwise use the Licensed content 'Content' in the named territory 'Territory' for the purpose listed 'the Use' on Page 1 of this Agreement subject to the following terms and conditions.

1. The License is limited to the permission granted and the Content detailed herein and does not extend to any other permission or content.
2. Cambridge gives no warranty or indemnity in respect of any third-party copyright material included in the Content, for which the Licensee should seek separate permission clearance.
3. The integrity of the Content must be ensured.
4. The License does extend to any edition published specifically for the use of handicapped or reading-impaired individuals.
5. The Licensee shall provide a prominent acknowledgement in the following format:
author/s, title of article, name of journal, volume number, issue number, page references, , reproduced with permission.

Other terms and conditions:

v1.0

Questions? customercare@copyright.com or +1-855-239-3415 (toll free in the US) or +1-978-646-2777.

REFERENCES

- Abernathay, R. and Cessi, P. (2014). Topographic enhancement of eddy efficiency in baroclinic equilibration. *J. Phys. Oceanogr.*, 44(8):2107–2126.
- Adcock, S. T. and Marshall, D. P. (2000). Interactions between geostrophic eddies and the mean circulation over large-scale bottom topography. *J. Phys. Oceanogr.*, 30(12):3223–3238.
- Ait-Chaalaal, F. and Schneider, T. (2015). Why eddy momentum fluxes are concentrated in the upper troposphere. *J. Atmos. Sci.*, 72(4):1585–1604.
- Arbic, B. K. and Flierl, G. R. (2004a). Baroclinically unstable geostrophic turbulence in the limits of strong and weak bottom ekman friction: Application to midocean eddies. *J. Phys. Oceanogr.*, 34(10):2257–2273.
- Arbic, B. K. and Flierl, G. R. (2004b). Effects of mean flow direction on energy, isotropy, and coherence of baroclinically unstable beta-plane geostrophic turbulence. *J. Phys. Oceanogr.*, 34(1):77–93.
- Arbic, B. K., Polzin, K. L., Scott, R. B., Richman, J. G., and Shriver, J. F. (2013). On eddy viscosity, energy cascades, and the horizontal resolution of gridded satellite altimeter products. *J. Phys. Oceanogr.*, 43(2):283–300.
- Baldwin, M. P., Rhines, P. B., Huang, H. P., and McIntyre, M. E. (2007). The jet-stream conundrum. *Science*, 315(5811):467–468.
- Barthel, A., Hogg, A., Waterman, S., and Keating, S. (2017). Jet-topography interactions affect energy pathways to the deep southern ocean. *J. Phys. Oceanogr.*, 47(7):1799–1816.
- Beebe, R. F., Ingersoll, A. P., Hunt, G. E., Mitchell, J. L., and Müller, J. P. (1980). Measurements of wind vectors, eddy momentum transports, and energy conversions in jupiter’s atmosphere from voyager 1 images. *Geophys. Res. Lett.*, 7(1):1–4.
- Benilov, E. S. (2001). Baroclinic instability of two-layer flows over one-dimensional bottom topography. *J. Phys. Oceanogr.*, 31(8):2019–2025.
- Berloff, P. (2005a). On dynamically consistent eddy fluxes. *Dynam. Atmos. Oceans*, 38(3):123–146.
- Berloff, P. (2005b). On rectification of randomly forced flows. *J. Mar. Res.*, 63(3):497–527.

- Berloff, P. and Kamenkovich, I. (2013a). On spectral analysis of mesoscale eddies. part i: Linear analysis. *J. Phys. Oceanogr.*, 43(12):2505–2527.
- Berloff, P. and Kamenkovich, I. (2013b). On spectral analysis of mesoscale eddies. part ii: Nonlinear analysis. *J. Phys. Oceanogr.*, 43(12):2528–2544.
- Berloff, P., Kamenkovich, I., and Pedlosky, J. (2009a). A mechanism of formation of multiple zonal jets in the oceans. *J. Fluid Mech.*, 628:395–425.
- Berloff, P., Kamenkovich, I., and Pedlosky, J. (2009b). A model of multiple zonal jets in the oceans: Dynamical and kinematical analysis. *J. Phys. Oceanogr.*, 39(11):2711–2734.
- Berloff, P., Karabasov, S., Farrar, J. T., and Kamenkovich, I. (2011). On latency of multiple zonal jets in the oceans. *J. Fluid Mech.*, 686:534–567.
- Berloff, P. S. and McWilliams, J. C. (1999). Quasigeostrophic dynamics of the western boundary current. *J. Phys. Oceanogr.*, 29(10):2607–2634.
- Boland, E., Thompson, A. F., Shuckburgh, E., and Haynes, P. (2012). The formation of nonzonal jets over sloped topography. *J. Phys. Oceanogr.*, 42(10):1635–1651.
- Buckingham, C. E. and Cornillon, P. C. (2013). The contribution of eddies to striations in absolute dynamic topography. *J. Geophys. Res. Oceans*, 118(1):448–461.
- Chan, C. J., Plumb, R. A., and Cerovecki, I. (2007). Annular modes in a multiple migrating zonal jet regime. *J. Atmos. Sci.*, 64(11):4053–4068.
- Charney, J. C. (1971). Geostrophic turbulence. *J. Atmos. Sci.*, 28:1087–1095.
- Charney, J. G. (1948). On the scale of atmospheric motions. *Geofys. Publ. Oslo*, 17(2):1–17.
- Charney, J. G. and Stern, M. (1962). On the stability of internal baroclinic jets in a rotating atmosphere. *J. Atmos. Sci.*, 19(2):159–172.
- Chelton, D. B., Deszoeke, R. A., Schlax, M. G., El Naggar, K., and Siwertz, N. (1998). Geographical variability of the first baroclinic rossby radius of deformation. *J. Phys. Oceanogr.*, 28(3):433–460.
- Chemke, R. and Kaspi, Y. (2015a). The latitudinal dependence of atmospheric jet scales and macroturbulent energy cascades. *J. Atmos. Sci.*, 72(10):3891–3907.
- Chemke, R. and Kaspi, Y. (2015b). Poleward migration of eddy-driven jets. *J. Adv. Model. Earth Sy.*, 7(3):1457–1471.
- Chen, C. and Kamenkovich, I. (2013). Effects of topography on baroclinic instability. *J. Phys. Oceanogr.*, 43(4):790–804.

- Chen, C., Kamenkovich, I., and Berloff, P. (2015). On the dynamics of flows induced by topographic ridges. *J. Phys. Oceanogr.*, 45(3):927–940.
- Chen, C., Kamenkovich, I., and Berloff, P. (2016). Eddy trains and striations in quasi-geostrophic simulations and the ocean. *J. Phys. Oceanogr.*, 46(9):2807–2825.
- Cho, J. Y. K. and Polvani, L. M. (1996). The emergence of jets and vortices in freely evolving, shallow-water turbulence on a sphere. *Phys. Fluids*, 8(6):1531–1552.
- Connaughton, C. P., Nadiga, B. T., Nazarenko, S. V., and Quinn, B. E. (2010). Modulational instability of rossby and drift waves and generation of zonal jets. *J. Fluid Mech.*, 654:207–231.
- Constantinou, N. C., Farrell, B. F., and Ioannou, P. J. (2014). Emergence and equilibration of jets in beta-plane turbulence: applications of stochastic structural stability theory. *J. Atmos. Sci.*, 71(5):1818–1842.
- Cravatte, S., Kessler, W. S., and Marin, F. (2012). Intermediate zonal jets in the tropical pacific ocean observed by argo floats*. *J. Phys. Oceanogr.*, 42(9):1475–1485.
- Cravatte, S., Kestenare, E., Marin, F., Dutrieux, P., and Firing, E. (2017). Subthermocline and intermediate zonal currents in the tropical pacific ocean: paths and vertical structure. *J. Phys. Oceanogr.*, 47(9):2305–2324.
- Danilov, S. and Gry檀ik, V. M. (2004). Barotropic beta-plane turbulence in a regime with strong zonal jets revisited. *J. Atmos. Sci.*, 61(18):2283–2295.
- Danilov, S. and Gurarie, D. (2004). Scaling, spectra and zonal jets in beta-plane turbulence. *Phys. Fluids*, 16(7):2592–2603.
- Dar, G., Verma, M. K., and Eswaran, V. (2001). Energy transfer in two-dimensional magnetohydrodynamic turbulence: formalism and numerical results. *Physica D*, 157(3):207–225.
- Dewar, W. K. (1998). Topography and barotropic transport control by bottom friction. *J. Mar. Res.*, 56(2):295–328.
- Dickinson, R. E. (1969). Theory of planetary wave-zonal flow interaction. *J. Atmos. Sci.*, 26(1):73–81.
- Dritschel, D. G. and McIntyre, M. E. (2008). Multiple jets as pv staircases: the phillips effect and the resilience of eddy-transport barriers. *J. Atmos. Sci.*, 65(3):855–874.
- Dunkerton, T. J. and Scott, R. K. (2008). A barotropic model of the angular momentum-conserving potential vorticity staircase in spherical geometry. *J. Atmos. Sci.*, 65(4):1105–1136.

- Edmon Jr, H., Hoskins, B., and McIntyre, M. (1980). Eliassen-palm cross sections for the troposphere. *J. Atmos. Sci.*, 37(12):2600–2616.
- Farrell, B. F. and Ioannou, P. J. (2007). Structure and spacing of jets in barotropic turbulence. *J. Atmos. Sci.*, 64(10):3652–3665.
- Gierasch, P. J., Conrath, B. J., and Magalha, J. A. (1986). Zonal mean properties of jupiter's upper troposphere from voyager infrared observations. *Icarus*, 67(3):456–483.
- Haidvogel, D. B. and Held, I. M. (1980). Homogeneous quasi-geostrophic turbulence driven by a uniform temperature gradient. *J. Atmos. Sci.*, 37(12):2644–2660.
- Hallberg, R. and Gnanadesikan, A. (2006). The role of eddies in determining the structure and response of the wind-driven southern hemisphere overturning: Results from the modeling eddies in the southern ocean (meso) project. *J. Phys. Oceanogr.*, 36(12):2232–2252.
- Hannachi, A., Jolliffe, I. T., and Stephenson, D. B. (2007). Empirical orthogonal functions and related techniques in atmospheric science: A review. *Int. J. Climatol.*, 27(9):1119–1152.
- Hart, J. E. (1975a). Baroclinic instability over a slope. part i: Linear theory. *J. Phys. Oceanogr.*, 5(4):625–633.
- Hart, J. E. (1975b). Baroclinic instability over a slope. part ii: Finite-amplitude theory. *J. Phys. Oceanogr.*, 5(4):634–641.
- Held, I. M. (2007). Progress and problems in large-scale atmospheric dynamics.
- Hogg, A. M. and Munday, D. R. (2014). Does the sensitivity of southern ocean circulation depend upon bathymetric details? *Philos. T. Roy. Soc. A*, 372(2019):20130050.
- Holland, W. R. (1978). The role of mesoscale eddies in the general circulation of the oceannumerical experiments using a wind-driven quasi-geostrophic model. *J. Phys. Oceanogr.*, 8(3):363–392.
- Holloway, G. (2010). Eddy stress and shear in 2-d flow. *J. Turbulence*, (11):N14.
- Hristova, H. G., Pedlosky, J., and Spall, M. A. (2008). Radiating instability of a meridional boundary current. *J. Phys. Oceanogr.*, 38(10):2294–2307.
- Huang, H. P. and Robinson, W. A. (1998). Two-dimensional turbulence and persistent zonal jets in a global barotropic model. *J. Atmos. Sci.*, 55(4):611–632.
- Ingersoll, A. P., Beebe, R. F., Mitchell, J. L., Garneau, G. W., Yagi, G. M., and Müller, J. P. (1981). Interaction of eddies and mean zonal flow on jupiter as inferred from voyager 1 and 2 images. *J. Geophys. Res. Space Physics*, 86(A10):8733–8743.

- Ingersoll, A. P., Gierasch, P. J., Banfield, D., Vasavada, A. R., and Team, G. I. (2000). Moist convection as an energy source for the large-scale motions in jupiter's atmosphere. *Nature*, 403(6770):630–632.
- Jochum, M., Danabasoglu, G., Holland, M., Kwon, Y.-O., and Large, W. (2008). Ocean viscosity and climate. *J. Geophys. Res. Oceans*, 113(C6).
- Kamenkovich, I., Berloff, P., and Pedlosky, J. (2009). Role of eddy forcing in the dynamics of multiple zonal jets in a model of the north atlantic. *J. Phys. Oceanogr.*, 39(6):1361–1379.
- Karabasov, S. A., Berloff, P., and Goloviznin, V. M. (2009). Cabaret in the ocean gyres. *Ocean Model.*, 30(2):155–168.
- Karabasov, S. A. and Goloviznin, V. M. (2009). Compact accurately boundary-adjusting high-resolution technique for fluid dynamics. *J. Comput. Phys.*, 228(19):7426–7451.
- Khatri, H. and Berloff, P. (2018a). A mechanism for jet drift over topography. *J. Fluid Mech.*, 845:392–416.
- Khatri, H. and Berloff, P. (2018b). Role of eddies in the maintenance of multiple jets embedded in eastward and westward baroclinic shears. *Fluids*, 3(4):91.
- Khatri, H., Sukhatme, J., Kumar, A., and Verma, M. K. (2018). Surface ocean enstrophy, kinetic energy fluxes, and spectra from satellite altimetry. *J. Geophys. Res. Oceans*, 123(5):3875–3892.
- Kong, H. and Jansen, M. F. (2017). The eddy diffusivity in barotropic β -plane turbulence. *Fluids*, 2(4):54.
- Kraichnan, R. H. (1967). Inertial ranges in two-dimensional turbulence. *Phys. Fluids*, 10(7):1417–1423.
- Kramer, W., van Buren, M. G., Clercx, H. J. H., and van Heijst, G. J. F. (2006). β -plane turbulence in a basin with no-slip boundaries. *Phys. Fluids*, 18(2):026603.
- Lee, S. (1997). Maintenance of multiple jets in a baroclinic flow. *J. Atmos. Sci.*, 54(13):1726–1738.
- Lu, J. and Speer, K. (2010). Topography, jets, and eddy mixing in the southern ocean. *J. Mar. Res.*, 68(3-1):479–502.
- Maltrud, M. E. and Vallis, G. K. (1991). Energy spectra and coherent structures in forced two-dimensional and beta-plane turbulence. *J. Fluid Mech.*, 228:321–342.
- Manfroi, A. and Young, W. R. (1999). Slow evolution of zonal jets on the beta plane. *J. Atmos. Sci.*, 56(5):784–800.

- Marston, J. B., Conover, E., and Schneider, T. (2008). Statistics of an unstable barotropic jet from a cumulant expansion. *J. Atmos. Sci.*, 65(6):1955–1966.
- Maximenko, N. A., Bang, B., and Sasaki, H. (2005). Observational evidence of alternating zonal jets in the world ocean. *Geophys. Res. Lett.*, 32:L12607.
- Melnichenko, O. V., Maximenko, N. A., Schneider, N., and Sasaki, H. (2010). Quasi-stationary striations in basin-scale oceanic circulation: vorticity balance from observations and eddy-resolving model. *Ocean Dynam.*, 60(3):653–666.
- Munday, D. R., Johnson, H. L., and Marshall, D. P. (2013). Eddy saturation of equilibrated circumpolar currents. *J. Phys. Oceanogr.*, 43(3):507–532.
- Nadiga, B. T. (2006). On zonal jets in oceans. *Geophys. Res. Lett.*, 33:L10601.
- Nakano, H. and Hasumi, H. (2005). A series of zonal jets embedded in the broad zonal flows in the pacific obtained in eddy-permitting ocean general circulation models. *J. Phys. Oceanogr.*, 35(4):474–488.
- Panetta, R. L. (1993). Zonal jets in wide baroclinically unstable regions: Persistence and scale selection. *J. Atmos. Sci.*, 50(14):2073–2106.
- Poulin, F. and Flierl, G. (2005). The influence of topography on the stability of jets. *J. Phys. Oceanogr.*, 35(5):811–825.
- Qiu, B., Chen, S., and Sasaki, H. (2013). Generation of the north equatorial undercurrent jets by triad baroclinic rossby wave interactions. *J. Phys. Oceanogr.*, 43(12):2682–2698.
- Radko, T. and Kamenkovich, I. (2017). On the topographic modulation of large-scale eddying flows. *J. Phys. Oceanogr.*, 47(9):2157–2172.
- Read, P., Yamazaki, Y., Lewis, S., Williams, P. D., Miki-Yamazaki, K., Sommeria, J., Didelle, H., and Fincham, A. (2004). Jupiter’s and saturn’s convectively driven banded jets in the laboratory. *Geophys. Res. Lett.*, 31(22).
- Read, P. L., Conrath, B. J., Fletcher, L. N., Gierasch, P. J., Simon-Miller, A. A., and Zuchowski, L. C. (2009). Mapping potential vorticity dynamics on saturn: Zonal mean circulation from cassini and voyager data. *Planet. Space Sci.*, 57(14):1682–1698.
- Read, P. L., Yamazaki, Y. H., Lewis, S. R., Williams, P. D., Wordsworth, R., Miki-Yamazaki, K., Sommeria, J., and Didelle, H. (2007). Dynamics of convectively driven banded jets in the laboratory. *J. Atmos. Sci.*, 64(11):4031–4052.
- Rhines, P. B. (1975). Waves and turbulence on a beta-plane. *J. Fluid Mech.*, 69(03):417–443.
- Rhines, P. B. (1979). Geostrophic turbulence. *Annu Rev Fluid Mech.*, 11(1):401–441.

- Richards, K. J., Maximenko, N. A., Bryan, F. O., and Sasaki, H. (2006). Zonal jets in the pacific ocean. *Geophys. Res. Lett.*, 33:L03605.
- Rudko, M. V., Kamenkovich, I. V., Iskadarani, M., and Mariano, A. J. (2018). Zonally elongated transient flows: Phenomenology and sensitivity analysis. *J. Geophys. Res. Oceans*, 123(6):3982–4002.
- Scott, R. K. and Polvani, L. M. (2007). Forced-dissipative shallow-water turbulence on the sphere and the atmospheric circulation of the giant planets. *J. Atmos. Sci.*, 64(9):3158–3176.
- Sinha, B. and Richards, K. J. (1999). Jet structure and scaling in southern ocean models. *J. Phys. Oceanogr.*, 29(6):1143–1155.
- Smith, S. (2007). Eddy amplitudes in baroclinic turbulence driven by nonzonal mean flow: Shear dispersion of potential vorticity. *J. Phys. Oceanogr.*, 37(4):1037–1050.
- Sokolov, S. and Rintoul, S. R. (2007). Multiple jets of the antarctic circumpolar current south of australia. *J. Phys. Oceanogr.*, 37(5):1394–1412.
- Srinivasan, K. (2013). *Stochastically forced zonal flows*. University of California, San Diego.
- Srinivasan, K. and Young, W. R. (2012). Zonostrophic instability. *J. Atmos. Sci.*, 69(5):1633–1656.
- Srinivasan, K. and Young, W. R. (2014). Reynolds stress and eddy diffusivity of β -plane shear flows. *J. Atmos. Sci.*, 71(6):2169–2185.
- Stern, A., Nadeau, L. P., and Holland, D. (2015). Instability and mixing of zonal jets along an idealized continental shelf break. *J. Phys. Oceanogr.*, 45(9):2315–2338.
- Suhas, D. and Sukhatme, J. (2015). Low frequency modulation of jets in quasigeostrophic turbulence. *Phys. Fluids*, 27(1):016601.
- Sukoriansky, S., Dikovskaya, N., and Galperin, B. (2007). On the arrest of inverse energy cascade and the rhines scale. *J. Atmos. Sci.*, 64(9):3312–3327.
- Tamsitt, V., Drake, H. F., Morrison, A. K., Talley, L. D., Dufour, C. O., Gray, A. R., Griffies, S. M., Mazloff, M. R., Sarmiento, J. L., Wang, J., et al. (2017). Spiraling pathways of global deep waters to the surface of the southern ocean. *Nature Comm.*, 8(1):172.
- Tansley, C. E. and Marshall, D. P. (2001). Flow past a cylinder on a β plane, with application to gulf stream separation and the antarctic circumpolar current. *J. Phys. Oceanogr.*, 31(11):3274–3283.

- Thompson, A. F. (2008). The atmospheric ocean: eddies and jets in the antarctic circumpolar current. *Philos. T. Roy. Soc. A*, 366(1885):4529–4541.
- Thompson, A. F. (2010). Jet formation and evolution in baroclinic turbulence with simple topography. *J. Phys. Oceanogr.*, 40(2):257–278.
- Thompson, A. F. and Richards, K. J. (2011). Low frequency variability of southern ocean jets. *J. Geophys. Res. Oceans*, 116:C09022.
- Thompson, A. F. and Sallée, J. (2012). Jets and topography: Jet transitions and the impact on transport in the antarctic circumpolar current. *J. Phys. Oceanogr.*, 42(6):956–972.
- Thompson, A. F. and Young, W. R. (2007). Two-layer baroclinic eddy heat fluxes: Zonal flows and energy balance. *J. Atmos. Sci.*, 64(9):3214–3231.
- Thompson, R. O. (1971). Why there is an intense eastward current in the north atlantic but not in the south atlantic. *J. Phys. Oceanogr.*, 1(3):235–237.
- Thompson, R. O. (1980). A prograde jet driven by rossby waves. *J. Atmos. Sci.*, 37(6):1216–1226.
- Tréguyer, A. M. and Panetta, R. L. (1994). Multiple zonal jets in a quasigeostrophic model of the antarctic circumpolar current. *J. Phys. Oceanogr.*, 24(11):2263–2277.
- Vallis, G. K. (2017). *Atmospheric and oceanic fluid dynamics*. Cambridge University Press.
- Vallis, G. K. and Maltrud, M. E. (1993). Generation of mean flows and jets on a beta plane and over topography. *J. Phys. Oceanogr.*, 23(7):1346–1362.
- Van Sebille, E., Kamenkovich, I., and Willis, J. K. (2011). Quasi-zonal jets in 3-d argo data of the northeast atlantic. *Geophys. Res. Lett.*, 38:L02606.
- Wang, J., Spall, M. A., Flierl, G. R., and Malanotte-Rizzoli, P. (2012). A new mechanism for the generation of quasi-zonal jets in the ocean. *Geophys. Res. Lett.*, 39:L10601.
- Williams, G. P. (1979). Planetary circulations: 2. the jovian quasi-geostrophic regime. *J. Atmos. Sci.*, 36(5):932–969.
- Williams, G. P. (2003). Jovian dynamics. part iii: Multiple, migrating, and equatorial jets. *J. Atmos. Sci.*, 60(10):1270–1296.
- Wordsworth, R., Read, P., and Yamazaki, Y. (2008). Turbulence, waves, and jets in a differentially heated rotating annulus experiment. *Phys. Fluids*, 20(12):126602.
- Young, R. M. B. and Read, P. L. (2017). Forward and inverse kinetic energy cascades in jupiters turbulent weather layer. *Nature Phys.*, 13(11):1135.

Youngs, M. K., Thompson, A. F., Lazar, A., and Richards, K. (2017). ACC meanders, energy transfer, and mixed barotropic–baroclinic instability. *J. Phys. Oceanogr.*, 47(6):1291–1305.